Numerical modeling of low-pressure plasmas: applications to electric double layers

A thesis submitted for the degree of
Doctor of Philosophy of the Australian National University
and
Docteur de l'Université Paul Sabatier
by
Albert Meige

Research Supervisors
R. W. Boswell
J.-P. Boeuf

Research Advisors
C. Charles
G. J. M. Hagelaar

External Examiners
P. Chabert
J. Verboncoeur

Space Plasma Power and Propulsion (SP_3),
Research School of Physical Sciences and Engineering,
the Australian National University,
Canberra, ACT, 0200, Australia

Centre de Physique des Plasmas et de leurs Applications de Toulouse (CPAT),
Université Paul Sabatier,
118 route de Narbonne, Toulouse Cedex 31062, France

This thesis contains no material which has been accepted for the award of any other degree or diploma in any university. To the best of the author's knowledge and belief, it contains no material previously published or written by another person, except where due reference is made in the text.

Albert Meige
July 13, 2006

Acknowledgements

First of all, I would like to thank Rod, who was not only my supervisor, but I believe also a very good friend. Rod first gave me the opportunity to start a PhD in plasma physics, while I was "just" an engineer in telecommunications. Thank you for believing in me and thank you for all that you taught me. Thank you for your professional and personal support. I hope in 10 years, after a couple of kidneys and a Stinco D'Agnello at Marinetti's, you we tell your new students, "actually, we did that with Albert 10 years ago, but never published it".

Still at the Australian National University, I would like to thank Christine for always taking the time to talk about plasma physics, even when she was crawling under piles of work.

I would also like to thank my supervisors at the Université Paul Sabatier. Although I spent far less time there, each of my stays at the CPAT was very fruitful. Thank you Jean-Pierre for giving me the opportunity to do a PhD in your group and thank you for supporting me although the research I was carrying out did not really belong to the research themes of the CPAT. Also a special thank to Gerjan who spent a huge number of hours sharing with me his knowledge in numerical techniques and simulations.

I also acknowledge the work and valuable comments of all the members of my Jury: Rod Boswell, Jean-Pierre Boeuf, Gerjan Hagelaar, Pascal Chabert, John Verboncoeur and Richard Fournier.

A number of people have also helped me all the way through my PhD. Thank you to Miles Turner who welcomed me at the Plasma Research Laboratory in Dublin and who gave me some of the original ideas of this thesis. Thank you to Mike Lieberman who tried to prevent me from writing my thesis by constantly giving me new ideas. Thank you to Pascal Chabert for providing the famous "tickets rouges" and for giving me the opportunity to progress in the electronegative double-layer simulations. Thank you to Bob Dewar and Matthew Hole for helping me in my triple integrals over velocity space. Thank you to Pascal Brault for my first seminar. Thank you to Peter Alexander that I have not solicited too much, unlike my colleagues experimentalist, but who has prepared to most awesome BBQs and Xmas Ev's. Thank you to the people at the School Computer Unit (Julie, James, Shiu) for their help during the last three years. A special thank especially for the time, just before I started writing this thesis, when I realized that all my data from 2005 had gone.

Thank you to my friends at SP_3 and in the other plasma labs: Orson, for coming to my birthday party. Nico for a number of interesting conversations on electronegative plasmas, life, universe and everything. Niko, for every thing

before the orange juice. Malou, for your immuable sourire. Cormac, for trying to destroy my liver when I was writing my thesis. Devin, for inviting me at your "woody". Dave P. and Peter L., for reminding me that my thesis could have been a lot more difficult to write. Pascal V., for the G5.

I would also like to thank my friends in France, Hong Kong and Mayotte for giving me a roof, a lift and some good time, when I was in transit and for visiting me in Australia: Pilou, Fab, Seb, Filou, Jasmin, Troll, Rage, Mel, Lise, Dino.

Also a special thank to Michel Puech, father of the young girl I was giving magic courses to, who first put me in touch with Rod.

I also wish to thank my family, Toupette, Le Chef, Marie and my grand parents for their invaluable support and encouragements: Toupette pour les colis, Le Chef pour les invitations au restaurant, Marie pour plaidoyer pour le bonheur.

Finally, Ane deserves the most special thanks of all. Tussen takk min Sukker Klump for helping me to finish and for preventing me from falling further down into madness.

Abstract

Inductive plasmas are simulated by using a one-dimensional particle-in-cell simulation including Monte Carlo collision techniques (pic/mcc). To model inductive heating, a non-uniform radio-frequency (rf) electric field, perpendicular to the electron motion is included into the classical particle-in-cell scheme. The inductive plasma pic simulation is used to confirm recent experimental results that electric double layers can form in current-free plasmas. These results differ from previous experimental or simulation systems where the double layers are driven by a current or by imposed potential differences. The formation of a super-sonic ion beam, resulting from the ions accelerated through the potential drop of the double layer and predicted by the pic simulation is confirmed with nonperturbative laser-induced fluorescence measurements of ion flow. It is shown that at low pressure, where the electron mean free path is of the order of, or greater than the system length, the electron energy distribution function (eedf) is close to Maxwellian, except for its tail which is depleted at energies higher than the plasma potential. Evidence supporting that this depletion is mostly due to the high-energy electrons escaping to the walls is given.

A new hybrid simulation scheme (particle ions and Boltzmann/particle electrons), accounting for non-Maxwellian eedf and self-consistently simulating low-pressure high-density plasmas at low computational cost is proposed. Results obtained with the "improved" hybrid model are in much better agreement with the full pic simulation than the classical non self-consistent hybrid model. This model is used to simulate electronegative plasmas and to provide evidence supporting the fact that propagating double layers may spontaneously form in electronegative plasmas. It is shown that critical parameters of the simulation were very much aligned with critical parameters of the experiment.

Résumé

Un modèle *particle-in-cell / Monte Carlo collisions* (pic/mcc) unidimensionnel est utilsé pour simuler un plasma inductif. Un champ électrique radiofréquence (rf) est utilisé pour modéliser le chauffage inductif. L'amplitude du champ est non-uniforme et sa direction perpendiculaire à celle du déplacement des électrons. Ce modèle de plasma inductif permet de confirmer de récents résultats expérimentaux démontrant la possibilité de former des doubles couches électriques au sein de plasmas sans courant. Les doubles couches étudiées par le passé, aussi bien numériquement qu'expérimentalement, ont toujours été imposées par différence de potentiel ou en forçant un courant électrique dans le plasma. C'est en ce sens que les résultats présentés ici diffèrent de ceux précédemment reportés. La simulation prédit la formation d'un faisceau d'ions supersoniques résultant des ions accélérés par le saut de potentiel de la double couche. L'existence de ce faisceau d'ions supersoniques est confirmée par fluorescence induite par laser (nonperturbative laser-induced fluorescence). La simulation montre aussi qu'à basse pression, lorsque le libre parcours moyen des électrons est du même ordre de grandeur ou plus grand que le système, la fonction de distribution en énergie des électrons (eedf) est quasi-Maxwellienne, à l'exception de sa queue, dépeuplée pour des énergies supérieures au potentiel plasma. Ce dépeuplement est principalement dû à la perte aux parois des électrons les plus rapides.

Un nouveau schéma de simulation hybride (ions particulaires et électrons particulaires et Boltzmann), permettant de simuler des plasmas hautes pressions et hautes densités, en des temps de calculs relativement faibles, est proposé. Les résultats obtenus avec ce modèle hybride "amélioré" sont bien plus proches de ceux d'une simulation pic, que le sont ceux d'une simulation hybride classique. Ce modèle est appliqué à la simulation de décharges électronégatives et confirme des résultats expérimentaux démontrant la possibilité de formation de doubles couches propagatives. En particulier, les paramètres critiques contrôllant cette formation dans la simulation corroborent ceux de l'expérience.

Contents

Chapter 1

Introduction

1.1 Electric double layers in plasmas

The acceleration of charged particles (electrons or ions) is a fundamental aspect of plasma physics, as the creation of electron or ion beams have many applications such as propulsion, where the creation of an ion beam provides the thrust to the spaceship, plasma processing, where electron or ion beams are used to functionalize surfaces etc.

Charged particles are accelerated by electric fields, that can be either electrostatic or induced by time-varying magnetic fields. Hence, understanding the mechanisms that can create and maintain electric fields in plasma is of particular interest. One of these mechanisms is the electric double layer, which is, in essence, an electrostatic phenomenon where a significant electric field is sandwiched between two opposite space charge layers. Although electric double layers have been studied for many decades, the understanding that we have of them is still far from complete. In this section, a brief overview on various kinds of double layers and their investigation through theory, computer simulation, experiment, and observation in space, is given.

1.1.1 Definition and classification

Definition

An electric double layer[1] (DL) is a narrow localized region within a plasma, not directly attached to a wall, which can sustain a large potential difference (see Raadu 1989, and references therein). Although the global charge of a double layer vanishes and the surrounding plasma has no significant electric field, the quasi-neutrality within the double layer breaks down: the double layer is actually called "double layer" because it is composed of a layer of positive charge, "bending" the plasma potential like a normal sheath, and a layer of negative charge, "bending" the plasma potential back in the other direction, in order to join to the null-electric-field plasma. On each side of the double layer, the plasma may be perturbed by extended pre-sheaths, matching the conditions

[1] "Double layers" are also referred to as "double sheaths", "internal sheaths" or even simply as "sheaths" or "plasma potential discontinuities".

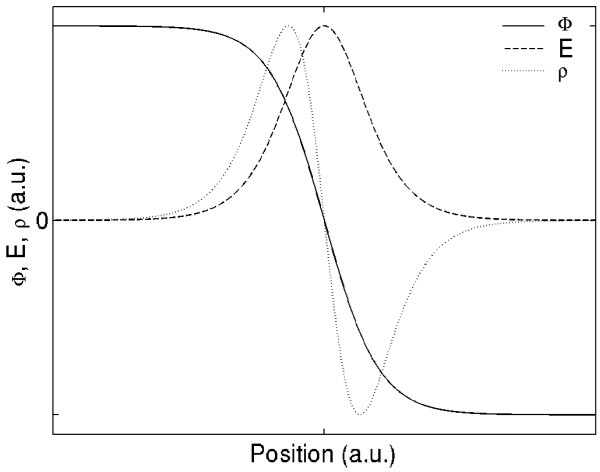

Figure 1.1: Typical plasma potential across an electric double layer (solid line), corresponding electric field (dashed line) and charge density (dotted line).

at the edges of the double layer to those of the undisturbed plasma, in the same fashion as a normal sheath. A typical double-layer potential profile and the associated electric field and charge density profiles are shown schematically in figure 1.1. It is generally accepted that double layers must fulfill the three conditions below

1. The double-layer potential drop Φ_{DL} must obey $|\Phi_{\mathrm{DL}}| > k_B T_e/e$, where k_B is the Boltzmann constant, T_e is the downstream[2] electron temperature and e is the elementary charge.

2. The electric field must be much stronger inside the double layer than outside and the global charge of the double layer must vanish.

3. Quasi-neutrality is locally violated at the position of the double layer.

Another typical, although not strictly necessary, condition is that the collisional mean free path is much longer than the double-layer thickness.

Double layers have been found in a variety of laboratory plasmas such as in constricted plasmas (Langmuir 1929), Mercury discharges (Stangeby and Allen 1973), Q-machines (Sato et al. 1976), triple plasma devices (Coakley et al. 1978), expanding plasmas (Charles and Boswell 2003) etc. Their role in astrophysics is also considerable as they are thought to be present in the magnetosphere and responsible for the acceleration of electrons onto the upper atmosphere, creating the fantastic aurora (Alfvén 1958, Albert and Lindstrom 1970, Temerin et al. 1982). Various theories on the formation of solar flares also involve double layers (Alfvén and Carlqvist 1967). Finally it was also recently proposed that double layers may play a significant role in supplying and accelerating plasma in magnetic coronal funnels (Boswell et al. 2006).

[2]The low-potential side of the double layer is generally referred to as "downstream", while the high-potential side of the double layer is generally referred to as "upstream".

The strength of experimental double layers ranges from very strong, with $e\Phi_{\rm DL}/k_BT_e$ as large as 2000 (Sato et al. 1981) or relatively weak, with $e\Phi_{\rm DL}/k_BT_e$ on the order of 1 (Chan et al. 1984). Properties of double layers can be very different one from another; for example, the potential drop associated with the double layer can be one-dimensional (Hershkowitz et al. 1981), two-dimensional (U-shaped) (Baker et al. 1981) or three-dimensional etc. Finally, they can be stable, propagating or transient and magnetized or not.

Classification

The large number of different types of double layers discovered in space, experiments, simulation and theories and the various names which may have been given to the same species of double layer over the last 50 years make their classification rather cumbersome. The classification presented here is probably not comprehensive but gives an overview of the various double layers that may be encountered. The classification is given in terms of double-layer *strength* $e\Phi_{\rm DL}/k_BT_e$, electron *drift* velocity v_D compared to the electron thermal velocity $v_{\rm th}$ and *monotonic behavior* of the double-layer potential distribution Φ. Two main classes of double layers can be defined according to their strength: *weak* and *strong* double layers, each of these classes being composed of several distinct families. The formation of strong double layers requires the existence of four distinct groups of particles (trapped and accelerated electrons and ions), while weak double layers may be constructed with only three out of these four groups.

i) $e\Phi_{\rm DL}/k_BT_e > 1$, $v_D > v_{\rm th}$, monotonic Φ. These double layers are generally referred to as strong and have been investigated theoretically (Langmuir 1929, Andrews and Allen 1971), experimentally (Quon and Wong 1976) and by computer simulations (Coakley et al. 1978, Hubbard and Joyce 1979).

ii) $e\Phi_{\rm DL}/k_BT_e > 1$, $v_D < v_{\rm th}$, monotonic Φ. This category of double layers is also referred to as strong. However, it seems that these low-electron-drift-velocity strong double layers are much less common than the previous category. Hollenstein et al. (1980) have observed such double layers experimentally. Nevertheless, it seems that strong double layers are generally observed when the electron drift is sufficiently large.

iii) $e\Phi_{\rm DL}/k_BT_e < 1$, $v_D < v_{\rm th}$, *non*-monotonic Φ. What is meant by non-monotonic is that a potential dip exists on the low-potential side of the double layer. These double layers form a particular family of the class of weak double layers and are referred to as ion-acoustic double layers (IADLs). IADLs are basically explained by a small electron drift generating ion-acoustic waves, propagating in the direction of the electron drift, whose amplitude increases while slowing down and whose potential distribution evolves to a double-layer-like structure. IADLs were first observed by Sato and Okuda (1980) in particle-in-cell simulations for sufficiently long systems and where the conditions $v_D < v_{\rm th}$ was verified. Chanteur et al. (1983) found that IADLs could be well explained modified Korteweg-de Vries (mKdV) equations. Temerin et al. (1982) presented satellite data suggesting that the auroral electron acceleration was associated with a series of small IADLs rather than a large single large structure. Chan

et al. (1984) reported the first laboratory evidence of such structures. The existence of IADLs was then confirmed by many subsequent experiments (Sekar and Saxena 1985)[3], analytical studies (Roychoudhury and Bhattacharyya 1989). The existence of IALDs in plasmas containing negative ions were also predicted analytically (Mishra et al. 2002, Gill et al. 2004).

iv) $e\Phi_{\rm DL}/k_BT_e < 1$, $v_D < v_{\rm th}$, monotonic Φ. This family of double layers is also part of the class of weak double layers and are very similar to IADL, but their particularity is that their potential distribution is monotonic, i.e. there is no potential dip on the low-potential side of the double layer. These double layers are referred to as slow-ion-acoustic double layers (SIADL) and their existence was first predicted by Perkins and Sun (1981) and then confirmed experimentally by Chan et al. (1986). Finally, we should mention the existence of slow-electron-acoustic double layers (SEADL) which are double-layer solutions of electron acoustic waves. Goswami et al. (1986) predicted their existence analytically in the case of plasma composed of one species of ions and two species of electrons (hot and cold).

1.1.2 Double layers: theory

Generally, various formalisms are used to describe double layers. Steady-state one-dimensional double layers may be described as solutions of the Vlasov-Poisson equations. Double layers may also be described by the Bernstein-Greene-Kruskal (BGK) method for finding non linear electrostatic waves. Also the dynamics of some very weak double layers can be described using the modified Korteweg-de Vries equation (mKdV), in which case the double layer appears to be a particular type of soliton etc. In this section, only a few of the considerable number of theoretical approaches that can be found in the literature are presented.

BGK double Layers

Bernstein et al. (1957) proved the existence of a class of solutions to the Vlasov equations (BGK solutions) containing potential structures with the three double-layer conditions given above. They showed that any arbitrary one-dimensional potential distribution could be constructed if a suitable number of trapped particles was added to the system. Although four groups of particles are generally present in BGK double layers (free and trapped electrons and ions), in principle three groups suffice to maintain double-layer structures (at least, this is the case for weak double layers). The BGK formalism only describes the steady-state double layer, but not the dynamical aspect of its formation; in other words, in principle a particular BGK double layer may be reached in many different ways (instability, creation of trapped particles etc.).

The first self-consistent BGK double-layer solution was constructed by Langmuir (1929). However, at that early stage, Langmuir did not know that his solution would be part of the wider class of BGK solutions. Nevertheless, in

[3] In the paper by Sekar and Saxena (1985) IADLs are referred to as asymmetric ion holes.

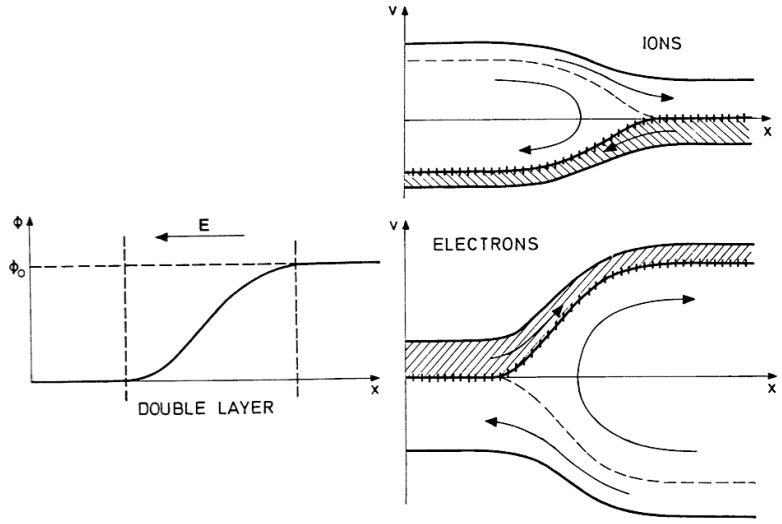

Figure 1.2: The potential distribution $\Phi(x)$, ion and electron phase space distribution across a double layer with potential Φ_0 and an internal electric field E. As indicated by the arrows and the separatrixes ('dashed' and 'barred'), there are phase space regions of transmitted and reflected particles for both species. It is physically important to distinguish between particles from different sources (at $x \to \pm\infty$) as indicated by the hatched and clear areas in phase space: at the boundaries ('barred' contours), there can be a sharp jump in phase space density, in principle a discontinuity, but in reality smoothed to some extent by fluctuations and diffusion processes. Outside the narrow transition region indicated by the vertical bars, the phase space densities on either side have no physical relation, being related to particles from widely separated sources (Raadu and Rasmussen 1988).

his theory, by the use of counter-streaming free electrons and ions, Langmuir could sustain a double layer; it is now known that this solution was unstable.

Langmuir described double layers formed between an electron-emitting cathode and an ion-emiting anode. He predicted that to ensure the neutrality in the system described above, the electron current I_e and the ion current I_i had to be related by

$$I_e = \sqrt{\frac{m_i}{m_e}} I_i, \tag{1.1}$$

where m_e and m_i are the electron and ion masses, respectively. Although this condition looks like a current condition, it is essentially a charge condition.

Andrews and Allen (1971) obtained conditions to embed the double layer within a quasi-neutral plasma using four groups of charged particles [rather than the two groups used by Langmuir (1929)]: thermal and accelerated electrons and ions.

Knorr and Goertz (1974) showed that, given three groups of particles and a potential structure, the fourth group of particles could be uniquely determined. They essentially gave an example of a BGK solution, demonstrating BGK's assertion that arbitrary potential distributions could be constructed with the right four group of particles.

Recently, Lieberman and Charles (2006) have developed a theory similar to that of Andrews and Allen (1971), introducing a fifth species of particles, ensuring the current-free nature of the double layer. The fifth species is a counter-streaming group of electrons, formed by reflection on the sheath at the insulated wall of the electrons accelerated through the double layer.

A number of similar theories can be found in the literature, where the authors construct arbitrary potential structures, by using a number of appropriate particle populations. However, one necessary condition for the existence of the BGK double layer is that trapped populations of electrons and ions can be maintained. This can be done in various ways, such as by the use of electrostatic potential troughs, magnetic mirrors, collisions causing backscattering etc.

Sagdeev potential and reductive perturbation method

Another general approach to describe the structure of steady-state plane parallel (one-dimensional) double layers consists in a direct integration of Poisson's equation and the time independent Vlasov equations for the separate particle components. This method was introduced by Sagdeev (1966) to describe shock waves in collisionless plasmas, as explained, for example, by Chen (1984, p. 297). This methods gives necessary conditions for the existence of double layers. Poisson's equation reads

$$-\varepsilon_0 \frac{d^2\Phi}{dx^2} = \rho(x). \tag{1.2}$$

If the charge density ρ can be expressed as a function of the electrostatic potential Φ, the Sagdeev potential can be defined as

$$V(\Phi) \equiv \int^{\Phi} \rho(\phi)\, \mathrm{d}\phi, \tag{1.3}$$

and Poisson's equation can be integrated once with respect to the potential Φ, yielding

$$\frac{1}{2}\varepsilon_0 \left(\frac{d\Phi}{dx}\right)^2 + V(\Phi) = \Pi, \tag{1.4}$$

where Π is a constant of integration. The behavior of this equation was made clear by Sagdeev (1966) and may be regarded as the total energy of a fictitious particle whose *position* is Φ and whose *velocity* is $d\Phi/dx$, the *time* being given by x. The *potential energy* of this fictitious particle is $V(\Phi)$. The charge density must vanish at the edges of the double layer, hence the boundary conditions are

$$\frac{dV}{d\Phi}(0) = \frac{dV}{d\Phi}(\Phi_{\mathrm{DL}}) = 0, \tag{1.5}$$

where the potential was defined to be $\Phi = 0$ and $\Phi = \Phi_{\mathrm{DL}}$ at the edges without loss of generality. In addition, the electric field also vanishes at the edges of the double layer, which yields

$$V(0) = V(\Phi_{\mathrm{DL}}) = \Pi, \tag{1.6}$$

also ensuring that the overall charge in the double layer vanishes; this condition is known as the generalized Langmuir condition. To guarantee real solutions, the Sagdeev potential also requires that $(d\Phi/dx)^2 > 0$, hence equation 1.4 yields

$$V(\Phi) < \Pi \tag{1.7}$$

for any potential in the double layer. In short, the conditions of existence of a double layer given by equations 1.5, 1.6 and 1.7 require that the Sagdeev potential has two maximum values at $\Phi = 0$ and $\Phi = \Phi_{\mathrm{DL}}$.

In cases where the net charge ρ is differentiable with respect to the potential Φ, the Sagdeev potential V then admits a second derivative at the double-layer edges and the existence condition 1.7 may be expanded to the second order yielding the generalized Bohm criteria

$$\frac{d^2V}{d\Phi^2}(0) < 0 \quad \text{and} \quad \frac{d^2V}{d\Phi^2}(\Phi_{\mathrm{DL}}) < 0, \tag{1.8}$$

In summary, the Sagdeev approach gives exact necessary conditions for the existence of double layers of arbitrary amplitude. However, the Sagdeev potential is not always definable, as it requires that the charge density can be expressed as a function of the plasma potential, which depends on the assumptions on the particle transport. Also, this method only treats the steady state and does not describe the underlying mechanisms leading to the double layer.

For completeness, although not directly related to the Sagdeev approach, the reductive perturbation method is also mentioned below. For weak double layers, the Sagdeev potential may be expanded to the fourth order in 1.4, yielding

$$\frac{1}{2}\left(\frac{d\Phi}{dx}\right)^2 + A_1\Phi^2 + A_2\Phi^3 + A_3\Phi^4 = 0, \tag{1.9}$$

where Π is set to zero and the coefficients A_1, A_2 and A_3 depend on physical parameters, such as temperature, density etc. Double-layer existence conditions 1.5 and 1.6 (with $\Pi = 0$) lead to

$$\frac{A_1}{A_3} = \Phi_{\mathrm{DL}}^2 \quad \text{and} \quad -\frac{A_2}{2A_3} = \Phi_{\mathrm{DL}}, \tag{1.10}$$

which is injected into 1.9 and factorized; this yields

$$\frac{1}{2}\left(\frac{d\Phi}{dx}\right)^2 + A_3\Phi^2(\Phi - \Phi_{\mathrm{DL}})^2 = 0 \qquad (A_3 < 0), \tag{1.11}$$

and a typical solution is

$$\Phi(x) = \frac{1}{2}\Phi_{\mathrm{DL}}\left[1 - \tanh\left(\Phi_{\mathrm{DL}}\sqrt{\frac{|A_3|}{2}}x\right)\right] \qquad (A_3 < 0). \tag{1.12}$$

This method, that offers conditions for the existence of weak double layers, has been used widely in the literature and is related to the Kortweg-de Vries equations. However, it should be kept in mind that this method is only valid for weak double layers and that neglecting the higher order terms in the expansion of the Sagdeev potential (equation 1.9) may lead to wrong qualitative results in cases other than weak double layers (Verheest 1993, for example).

1.1.3 Double layers: simulations

Because of the highly non-linear aspect of double layers, existing theories generally deal with steady-state double-layer solutions. Computer simulations have played, and still play a very important role in understanding the formation mechanisms and the non-linear dynamics of double layers. Double layers have been studied by computer simulation since the early 1970s. The first numerical simulation of plasma double layer reported is that of Goertz and Joyce (1975). In this paper, the authors make use of a one-dimensional particle-in-cell simulation in which particles that move out of the system are given back their original velocity and put back into the system on the left or right end depending on the sign of the initial velocity[4]. Electrons and ions are initially loaded with a Maxwellian velocity distribution function with the same temperature; the initial electron distribution function is shifted in velocity so that the electrons drift with a certain velocity. The electric field and potential are set to zero at the left boundary, as well as the electric field at the right boundary, while the potential at the right boundary is not imposed. Under certain conditions, a large potential difference was observed across the system and was interpreted as being a double layer.

The second double-layer simulation reported is that of DeGroot et al. (1977), unfortunately, the details of their algorithm are given in an unpublished report.

Finally, the third double-layer simulation reported is that of Joyce and Hubbard (1978), where, once again, the authors use the particle-in-cell scheme to

[4]Note that the boundary conditions used by Goertz and Joyce (1975) are not periodic, as opposed to what was commonly done at this early stage of particle-in-cell simulations.

simulate a bounded system, but this time, a constant electric field is added at each point of the grid. According to the authors, their simulation may be regarded as an experimental setup where grids with a certain potential were added at the boundaries. Under these conditions, they have observed the formation of double layers which profile was very similar to that investigated theoretically by Knorr and Goertz (1974) who had treated the double layer as a laminar, time-independent electrostatic shock.

Many subsequent double-layer simulations have followed, mostly using particle-in-cell technics (Sato and Okuda 1980, Borovsky 1981, Borovsky and Joyce 1982, Nanbu and Serikov 1997) or Vlasov simulations (Singh 1982, Singh and Schunk 1984, Newman et al. 2001).

1.1.4 Double layers: experiments

Hershkowitz (1985) has written an excellent review on electric double layers in laboratory experiments; many subsequent experiments have of course followed. In this section, a brief overview of experimental double layers is presented.

Electric double layers have been studied experimentally for many years. A well-known example is the plasma potential discontinuity that may exist at an abrupt change of diameter of the discharge tube: Andersson (1977) have measured the electron energy distribution function in front and behind the double layer, that they call "sheath", appearing at the sudden change in diameter of the discharge tube.

In this kind of multi-diameter discharge tube, the plasma in each section has different properties, a double layer may then appear at the constriction to match these different plasmas (Langmuir 1929). In this case, the double layer has two main purposes, namely i) increase the effective matching area by bulging out into the bigger chamber and ii) accelerate electrons from the cathode plasma into the smaller chamber to "boost" the ionization (Andrews and Allen 1971).

Plasma potential discontinuities have also been observed in arc plasma columns without any external disturbance from a tube constriction, where the formation of the discontinuity was only triggered by the current drawn through the plasma (Torvén and Babić 1975).

In this kind of tube discharge, double layers were visually apparent, however measuring the electron energy distribution function or the plasma potential was rather difficult because of the characteristics of the discharge tubes. Another problem was that ionization effects throughout the discharge tube tended to dominate observed phenomena. These issues were remedied by the use of both Q-machines (Sato et al. 1981) and double (Quon and Wong 1976) and especially triple (Coakley et al. 1978) plasma devices. As opposed to discharge tubes, where ionization take place throughout the device, in Q-machines and multiple plasma devices, the plasma can be produced in a different chamber from that sustaining the double layer.

Quon and Wong (1976) were the first to introduce a new type of device to investigate double layers. Their double plasma device gave strong experimental evidence supporting the fact that double layers may be regarded as BGK

structures. The experiment consisted of two plasmas separated by two grids, with plasma sources in both regions. The anode potential of each region was controlled independently from the other and the separation grids were biased. Steady state double layers were achieved by adjusting the plasma densities in each region and by adjusting the potential of the high potential source anode. However, as in discharge tube experiments, ionization was present throughout the discharge, including at the double layer position, hence dominating its characteristics. Producing BGK double layers in laboratory plasmas[5] consists of specifying the electron and ion distribution functions at the double layer boundaries, which must be chosen to be consistent with the potential and distribution function at the plasma boundaries. This requires precise control of the plasma density, temperature and most importantly electron and ion drift velocities. Since the plasma was produced by ionization throughout both chambers of the double plasma device, BGK double layers that depend only on plasma parameters at the chamber boundaries, could not be strictly created in this double plasma device.

Coakley et al. (1978) have significantly improved the formation of BGK double layers by the use of triple plasma devices, which are in essence a double plasma device with a center chamber. Generally, triple plasma devices consist of three distinct plasmas separated by two pair of grids. Hershkowitz et al. (1980) have shown that ionization could be restricted to the source chambers, hence allowing the formation of a double layer in an ionization-free region. The fundamental concept of triple plasma devices to study double layers is to achieve separate control of the ion and electron distribution functions and the plasma potential at each boundary, hence allowing strict BGK double layers.

An interesting feature of BGK solutions that is verified experimentally is that the plasma density presents a minimum at the position of the double layer, as opposed to the classical ambipolar potential which follows the plasma density, as it derives from plasma flowing out of regions without trapped particles.

Double layers formed in Q-machine experiments and double plasma devices are *generally* associated with a relatively small potential drop, with $e\Phi_{\mathrm{DL}}/k_B T_e$ on the order of 3-5 and are commonly referred to as "weak" double layers (Quon and Wong 1976). In triple plasma devices, double layers with a relatively large associated potential drop, with $e\Phi_{\mathrm{DL}}/k_B T_e$ on the order of 10 or more, are generally referred to as "strong" double layers (Coakley et al. 1978); however, note that "weak" double layers have also been reported in triple plasma device (Hershkowitz et al. 1981). "Very strong" or "ultrastrong" double layers, with $e\Phi_{\mathrm{DL}}/k_B T_e$ on the order of 2000, have also been observed (Sato et al. 1981). However, it should be kept in mind that depending on the scientific community concerned, double layers which are referred to as "weak" by certain researchers may be referred to as "strong" by others.

Experimental double layers may exist under various conditions. i) In steady state, double layers can be BGK solutions (Bernstein et al. 1957), entirely

[5] What is meant by "BGK double layers" in this context, i.e. for experimental double layers, is double layers that are formed experimentally in the same way as the BGK theoretical approach, i.e. by creating the appropriate groups of particles, compatible with a double-layer potential distribution.

controlled by both the electron and ion distribution functions and generally requiring four groups of particles, namely trapped and free electrons and ions. ii) Double layers can also be the result of turbulence (Chan and Hershkowitz 1982) or phase space vortices such as electron or ion holes (Pecseli and Trulsen 1982). iii) Finally, double layers may be the result of ionization on the high potential side of the double layer (Sekar and Saxena 1984)[6], which can be enhanced by the energy gain that electrons receive when they accelerate across the double layer. Experiments have now demonstrated that all three alternatives are possible and sometimes occur in combinations. It should be kept in mind that the existence of double layer [i), ii) or iii)] is different from the initial conditions that create it; for example, instabilities may well lead to BGK double layers.

1.1.5 Double layers: in space

In this section a few examples of the formation of double layers in space, from the Earth magnetosphere to the sun corona, are presented. The role of double layers in astrophysics goes far beyond these few examples. Raadu (1989) gives many more applications. Double layers in space are still a very active topic.

Although Alfvén (1958) had suggested that double layers may exist in the magnetosphere and could possibly be responsible for the acceleration of electrons onto the upper atmosphere that create the visible Aurora, data supporting this assumption were not available until the 1970s. Albert and Lindstrom (1970) confirmed Alfven's assumption from the pitch angle distribution of electrons in the ionosphere above the visible aurora. Mozer et al. (1977) and Temerin et al. (1982) reported the first direct measurements obtained with a satellite showing the presence of double-layer-like potential structures at altitudes of 3000-8000 km.

Solar flares are the results of a sudden irreversible release of energy in the corona and the chromosphere of the sun; they lead to particle acceleration and to a transient heating of the chromosphere. The formation of a double layer in a current carrying loop in the solar corona has been proposed as a mechanism for energy release in a solar flare (Jacobsen and Carlqvist 1964, Alfvén and Carlqvist 1967).

Finally it was recently proposed that double layers may play a significant role in supplying and accelerating plasma in magnetic coronal funnels (Boswell et al. 2006).

1.1.6 Summary

Double layers can be formed experimentally in a wide variety of shapes and sizes in both stable and moving structures. They can be one, two or three-dimensional structures and can exist in magnetized or unmagnetized plasmas. Their existence can be described in terms of BGK solutions, turbulence or

[6]The potential discontinuity that Sekar and Saxena (1984) observed was actually transient and due to a minute amount of gas leaking in the system when moving the probe and that was suddenly ionized.

ionization or combinations of all three. In each of these possibilities, the triggering may be different (for example BGK double layers may well be triggered by instabilities). They can be current driven or current free and can have a monotonic potential step, or present potential dips that are non-monotonic. They can exist in single ion plasmas or multi-species plasmas, such as plasmas containing negative ions. Depending on their strength, various analytical formalisms can be used to describe their dynamical aspect or *simply* their steady state. Most of the double layers that have been predicted analytically or by computer simulations have also been observed in space or the laboratory.

1.2 Modeling plasmas

Experiments provide many insights for the comprehension of phenomena occurring in plasmas, however, this is not always sufficient. The main reason for this is that measurements are not necessarily an easy task and in essence measurements always tend to disturb or disrupt the plasma, which is particularly the case when the size of the probes are of the same order as the phenomenon of interest. For simple physical reasons, introducing new diagnostics into an experiment can also be relatively cumbersome and a really challenging task. Under certain conditions, modeling can be a very good complement to experiment or even, sometimes, a substitute to improve the comprehension of plasma physics.

In physics, the word "model" is used to indicate a set of equations, data, and assumptions, that gives a mathematical representation of the major features of a certain physical phenomenon. By solving the model equations, the physical phenomenon is simulated.

Modeling plasmas has been approached in many different ways and the various types of model that have been developed often have quite dissimilar aims. Plasma models generally fall into one of the four categories or a combination of some of these four: equivalent circuit models, analytical models, fluid models and kinetic models.

1.2.1 Equivalent circuit models

Equivalent circuit models are relatively appealing because of their apparent simplicity. Plasmas have well-defined electrical properties that can be reproduced using equivalent circuits with the appropriate electrical components such as resistors, capacitors, inductors etc. Experimental or theoretical values can be directly used in the equations, allowing the determination of, for instance, the sheath voltage as a function of input parameters such as the source voltage, the frequency, the pressure etc. without the need of understanding the fundamental mechanisms underlying the plasma. The disadvantage of this approach is that it can not provide insight into complex phenomena. Many examples of such models can be found in the literature. Logan et al. (1977) proposed an equivalent circuit model for an rf sputtering system combined with empirical fittings of the plasma density, sheath thickness and power. Wood (1991) used an equivalent circuit model to investigate the perturbations introduced by

a probe floating in the plasma. Godyak et al. (1991) proposed a generalized circuit model.

1.2.2 Analytical models

Although a particular plasma may be fully described by the appropriate Boltzmann equation, solutions to such a general formulation are almost always obtained numerically and drastic assumptions and simplification must be made. The aim of analytical models is to derive some of the plasma properties from the knowledge of the underlying physical processes. Most of the time the whole discharge is not fully described, but rather a specific region of interest, such as the sheath, an electric double layer etc. For example, Tonks and Langmuir (1929) developed the first analytical models of dc (direct current) plasmas. By using a simplified kinetic model, where the electrons were taken to be Maxwellian and the ions described as a cold fluid, coupled to Poisson's equation, they have derived the so-called plasma-sheath equation. Another well-known analytical model describing the sheath was derived by Bohm (1949), who found the existence of the pre-sheath, joining the bulk plasma to the sheath etc.

1.2.3 Fluid models

Fluid models make assumptions on the particle distribution function, allowing the solution of moment equations rather than the full Boltzmann equation. Each moment equation is obtained by multiplying the Boltzmann equation by increasing powers of the velocity and integrating over velocity space. Generally, only the first three moments[7] are used, namely, continuity, momentum and energy conservation. Each moment equation added to the set of equations leads to the introduction of a new unknown; thus a closure assumption is always required. The moment equations are coupled to Poisson's equation to describe the behavior of a plasma.

Various approaches have been adopted in these models. Boeuf (1987) assumed that the transport coefficients (drift velocity and diffusion coefficients) and ionization depend only on the local electric field. Graves and Jensen (1986) assumed a Maxwellian distribution for the electrons etc.

The main drawback of these models is that the electron distribution function cannot be self-consistently calculated. This is a serious issue for low-pressure discharges where the electron energy distribution function can be highly non-local[8]. However, under the appropriate conditions, fluid models have proved to be very useful and computationally efficient (as opposed to particle simulations for example) and have been used extensively over the past 20 years (Meyyappan and Kreskovsky 1990, Passchier and Goedheer 1993, Boeuf and Pitchford 1995, etc.).

[7] The "first three moments of the Boltzmann equation" are also referred to as "the transport equations".

[8] What is meant by "non-local" is that the electron energy distribution function does not depend only on the local electric field.

1.2.4 Kinetic models

Simulations directly dealing with the particle kinematics are potentially the most powerful for studying low pressure plasmas for which the electron energy distribution function is likely to be non-Maxwellian. The calculation of the electron energy distribution function can be achieved in various ways. These include i) Monte Carlo simulations, where a large number of particles are followed one by one through an externally imposed electric field (Kushner 1983, for exmaple), ii) particle-in-cell simulations, where charged particles evolve in their own self-consistent electric field (Birdsall and Langdon 1985, Hockney and Eastwood 1988), iii) convective schemes (Sommerer et al. 1989) and Boltzmann solvers, that directly solve the Boltzmann equation (Hagelaar and Pitchford 2005). These techniques can be combined, for example Monte Carlo techniques are commonly used together with particle-in-cell simulation to handle charged particles-neutral collisions (Vahedi and Surendra 1995).

Full particle models, such as particle-in-cell, are very powerful as both the plasma potential and the particle transport are resolved self-consistently, but their main disadvantage is that they require more computational time compared to fluid models.

1.2.5 Hybrid models

Hybrid simulations use two or more of the techniques discussed above. For example by using particle-in-cell together with fluid techniques, one can take advantage of both computational speed, with less strong assumptions on the particle transport. Strictly speaking, all modern particle-in-cell simulations are actually hybrid simulations combining the basic particle-in-cell scheme with Monte Carlo techniques to treat collisions; however, they are generally not referred to as such.

Hybrid models generally refer to models where the electrons are treated as fluid while the ions are treated as particles or *vice et versa*. For example, Porteous and Graves (1991) have developed a two-dimensional hybrid model of an inductive plasma including magnetic confinement. In this model, electrons are considered as fluid and assumed to have a Maxwell-Boltzmann distribution, while the ions are treated as particles. Porteous et al. (1994) also used this code to model ECR (Electron Cyclotron Resonance) reactors etc. Hybrid models with fluid ions and Monte Carlo electrons are also relatively popular, as they allow the electron energy distribution function to be calculated, which is then used to calculate the collision rates and the transport coefficients used in fluid equations (Sommerer and Kushner 1992, for example).

1.3 Scope of this thesis

In essence, what this thesis has attempted to do is to present simulations of both electropositive and electronegative double layers in such a way that the basic physics underlying and accompanying these phenomena can be investigated and better understood. It is in this spirit that various models were developed.

The present thesis is composed of two distinct parts. The first part (Chapters 2, 3 and 4) focuses on current-free double layers, while the second part focuses on double layers in electronegative plasmas (Chapters 5 and 6).

As stated previously, most of the double layers observed in space, laboratory experiments and theoretical models are generally imposed by a potential difference or by drawing a current through the plasma. Charles and Boswell (2003) showed experimentally that a stationary double layer could be created in a current-free plasma, expanding along a diverging magnetic field. In this case, the double layer is not imposed and is sustained by the plasma itself. Following this recent discovery, current-free double layers have been the subject of intense research by many groups. A particle-in-cell simulation including Monte Carlo collisions techniques, together with a model for inductive heating, were developed to investigate the possibilities of forming double layers in current-free plasmas. The inductive heating model included in the one-dimensional particle-in-cell simulation consists of a non-uniform rf (radio-frequency) electric field perpendicular to the electron motion. The phenomenology, such as stochastic heating, resulting from such a transverse heating mechanism are investigated by the use of an analytical model (Chapter 2). The primary aims of the particle-in-cell simulation are i) to gain insight in the fundamental mechanisms underlying the formation of the current-free double layer observed by Charles and Boswell (2003) (Chapter 3) and ii) to investigate the particle transport, and especially the formation of an ion beam, in a current-free double-layer plasma (Chapter 4).

Plihon et al. (2005b) have reported the formation of propagating double layers in experimental electronegative plasmas. These authors have fully determined the window of parameters, such as the neutral gas pressure, the relative concentration of SF_6, the input power etc. for which these propagating double layers form. A self-consistent model, where a Monte Carlo simulation for particle electrons is coupled to a classical hybrid model was developed (Chapter 5). This model shed light on the mechanisms underlying the formation of propagating double layers and demonstrate the importance of certain parameters, such as the electronegativity, the chamber diameter, the heating mechanism etc. (Chapter 6).

These simulations and models have thrown considerable light on the mechanisms responsible for the formation of the double layers and have lead to a number of publications. Although by no means exhaustive, and naturally limited by the available computing resources, this work has represented the first attempt to understand the basic physics of the current-free double layers by simulations.

Chapter 2

Electron heating in a non-uniform transverse ac electric field[1]

2.1 Motivation

Electrons in a uniform alternating current (ac) electric field of the form $E = E_0 \cos(\omega t)$ are not heated as they are constantly accelerated and decelerated in phase with the field, unless they undergo collisions, for example with the background gas. Electron collisions with other particles destroy the phase coherence, thus leading to a net transfer of power from the field to the electrons. The fundamental mechanism that converts the electric field energy to thermal energy is the breaking of the phase-coherence between the field and the electron motion by collisions; this mechanism leads to an ohmic power transfer. The average ohmic power absorbed per electron is

$$P = -e < \boldsymbol{v} \cdot \boldsymbol{E} >_t, \tag{2.1}$$

where e is the elementary electron charge, $\boldsymbol{v}$ the systematic velocity of the electrons[2] and $\boldsymbol{E}$ the electric field. The symbol $< >_t$ denotes the time average. The systematic velocity $\boldsymbol{v}$ is generally derived from a momentum conservation equation

$$\frac{\partial \boldsymbol{v}}{\partial t} + \nu \boldsymbol{v} = -\frac{e\boldsymbol{E}}{m_e}, \tag{2.2}$$

where ν in the friction term is the momentum transfer frequency and m_e the electron mass. Equation 2.2 is solved for $\boldsymbol{v}$ and $\boldsymbol{v} \cdot \boldsymbol{E}$ is averaged in time, leading to the well-known Joule heating law of power absorbed per electron in a uniform ac electric field

$$P = \frac{1}{2} \frac{(eE_0)^2}{m_e \omega} \frac{\nu/\omega}{1 + (\nu/\omega)^2}, \tag{2.3}$$

[1] The work presented in this chapter was done in close collaboration with Dr. Gerjan Hagelaar during a research visit to the "Centre de Plasma et de leurs Applications de Toulouse".

[2] What is meant by "systematic velocity" is the average velocity of the ensemble of electrons, due to the electric field and collisions, as opposed to the thermal velocity.

where E_0 is the amplitude of the electric field and ω its frequency. Details of this classical calculation can be found in the literature (for example, see Lieberman and Lichtenberg 2005, p. 98).

Collisionless heating[3] of electrons in spatially non-uniform ac electric fields has been known for over 60 years, since Landau (1946) showed the collisionless damping of electrostatic waves in warm plasmas. Due to the spatial non-uniformity of the electric field, each individual electron sees a non-periodic field, resulting in a loss of the phase-coherence between the electron motion and the field, resulting in stochastic heating. Collisionless heating has been thoroughly investigated, as it appears in many situations where the ac electric field is non-uniform (rf sheath, skin depth layer etc.). A very interesting overview of this is given by Lieberman and Lichtenberg (2005) in Chapter 18 of the second edition of their book.

In the work presented later in this thesis (Chapter 3 and 4), a one-dimensional particle-in-cell simulation with three dimensions of velocity, including charged particle - neutral collisions[4] is used. In short, the electrons are allowed to move freely along the x axis, and are heated by a non-uniform rf electric field, acting in the y direction, perpendicular to the electron motion; energy and momentum are transfered to the other x and z directions via electron-neutral collisions. In the present chapter, the possible effects, such as stochastic heating, resulting from such a heating mechanism are investigated; this is done by developing an analytical model, the validity of which is then proven by the use of a Monte Carlo simulation.

The analytical work presented in this chapter is somewhat similar to the theory originally developed by Pippard (1949), which has been used to calculate the stochastic heating within the skin depth in low-pressure inductive discharges (Weibel 1967, Turner 1993, Godyak et al. 1993). However, in that case, the electric field was set to decay exponentially, while in the present case, the non-uniformity of the field is either a cosine function of space or a step function of space.

It should be kept in mind that the goal here is to investigate the possible effects resulting from such a transverse heating mechanism in *electrostatic* simulations. In reality, the situation would be far more complex as, for example, a magnetic field is associated with such an ac electric field. Although it was shown by Aliev et al. (1997), Cohen and Rognlien (1996ba) and Lieberman and Lichtenberg (2005, p. 700-703)[5] that the magnetic field associated with the electric field rotates the "kick" in the direction of the electron motion irrespective of the electric field direction, this effect is not considered as it would not be captured by the electrostatic simulation.

[3] Collisionless heating is also referred in the literature as stochastic or anomalous heating.

[4] The particle-in-cell (PIC) simulation scheme is thoroughly described in Chapter 3, however, its full understanding is not required to follow the present chapter.

[5] A number of typos remain in the original paper by Aliev et al. (1997); these have been corrected by Lieberman and Lichtenberg (2005, p. 700-703).

2.2 Analytical model

2.2.1 Another approach to derive the Joule heating law

In this section another approach to that of Section 2.1 to derive the power absorbed per electron in a uniform ac electric field is proposed. This other approach will be later adapted to the case of a non-uniform ac electric field, where the classical derivation of the power would be rather cumbersome if not impossible.

Let us consider an electron moving freely at a constant velocity along the x direction. There is no electric field in the direction of motion of the electron, but a uniform ac electric field in the perpendicular direction, labeled the y direction. The electron motion is bounded and from time to time the electron is reflected by a wall or a plasma sheath (the boundaries along x are assumed to be completely reflecting). The background neutral gas is uniform and the electrons undergo isotropic elastic collisions with neutrals only, at a constant collision frequency ν[6]; after a collision, the electron has completely "forgotten" its original momentum.

In this approach, the power absorbed by the electron during a free flight, i.e. between two collisions, is calculated. All the random parameters, such as the free-flight time, phase of the field etc. are then averaged over their distributions.

The ac electric field along y is given by

$$E = E_0 \cos(\omega t - \phi), \tag{2.4}$$

where E_0 and ω are the amplitude and the frequency of the ac electric field, respectively. The electron is born at phase ϕ of the field. Between two collisions, i.e during the free flight, the y-velocity of the electron is given by

$$\frac{\partial v}{\partial t} = -\frac{eE}{m_e}. \tag{2.5}$$

It is assumed that $v = v_0$ at $t = 0$. Equation 2.5 is solved for v

$$v = v_0 - \frac{eE_0}{m_e\omega}\left[\sin(\omega t - \phi) + \sin\phi\right]. \tag{2.6}$$

The electron starts its free-flight at any phase ϕ of the field; the product vE is thus averaged over the whole distribution of ϕ, uniformly distributed between 0 and 2π. Note that the distribution of the phase ϕ is uniform because the collision frequency ν was taken to be energy independent. By using equations 8.1 (Appendix 8.1, p. 133), it is found that all the terms in $< vE >_\phi$ are null except $< \cos(\omega t - \phi)\sin\phi >_\phi$, which leads to

$$< vE >_\phi = -\frac{1}{2}\frac{eE_0^2}{m_e\omega}\sin(\omega t), \tag{2.7}$$

[6]The electron-neutral collision cross section is proportional to the inverse of the electron velocity.

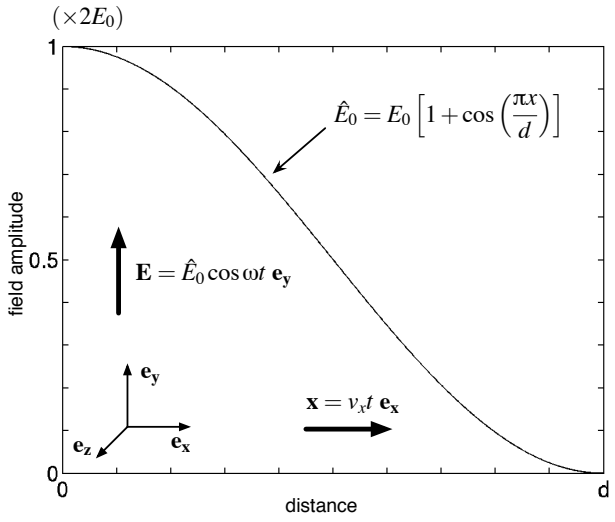

Figure 2.1: Schematic of the model: electrons move freely along the x direction at a constant velocity v_x between two reflecting boundaries separated by a distance d (the velocity v_x is constant between two collisions with neutrals). An ac electric field E heats the electrons in the y direction, perpendicular to the electron motion. The amplitude $\hat{E}_0$ of the electric field decays as a cosine function of space, is maximum in $x = 0$ and is equal to zero in $x = d$.

which is then averaged in time over the free-flight time distribution

$$< vE >_{\phi,\mathrm{t}} = \nu \int_0^\infty \exp(-\nu t) < vE >_\phi \ dt. \tag{2.8}$$

Equation 2.8 is calculated using equation 8.2 (Appendix 8.1, p. 133). Then, using equation 2.1 and rearranging yields

$$P = \frac{1}{2}\frac{(eE_0)^2}{m_e\omega}\frac{\nu/\omega}{1+(\nu/\omega)^2}, \tag{2.9}$$

which is exactly the same expression as that given by equation 2.3, proving the validity of this approach.

2.2.2 Power absorbed per electron in a non-uniform ac electric field: smooth transition

In section 2.2.1, the validity of another approach to calculate the power absorbed per electron in an electric field was demonstrated. Here, this method is applied to a non-uniform electric field. Once again the electric field is given by

$$E = \hat{E}_0 \cos(\omega t - \phi), \tag{2.10}$$

where the amplitude $\hat{E}_0$ is a cosine function of space in the direction x of the electron motion (figure 2.1). The reason why a cosine function is chosen for the present investigation is that it yields a complete analytical solution and its

derivation is not excessively cumbersome. The wave length of the amplitude variation is λ, and

$$\hat{E}_0 = E_0 \left[1 + \cos\left(\frac{2\pi x}{\lambda} - \Phi\right)\right]. \tag{2.11}$$

The assumptions are the same as in Section 2.2.1, and in addition, the distance between the two reflecting walls is $d = \lambda/2$. As the velocity v_x of the electron along the x direction is constant, the position x of the electron is given by $x = v_x t$ and $\Omega = 2\pi v_x/\lambda$ can be defined, hence the ac electric field can be written

$$E = E_0 \left[1 + \cos(\Omega t - \Phi)\right] \cos(\omega t - \phi). \tag{2.12}$$

Solving 2.6 for the field given by 2.10 gives

$$\begin{aligned} v = v_0 &- \frac{eE_0}{2m_e(\Omega+\omega)}\{\sin[(\Omega+\omega)t - (\Phi+\phi)] + \sin(\Phi+\phi)\} \\ &- \frac{eE_0}{2m_e(\Omega-\omega)}\{\sin[(\Omega-\omega)t - (\Phi-\phi)] + \sin(\Phi-\phi)\} \\ &- \frac{eE_0}{m_e\omega}[\sin(\omega t - \phi) + \sin\phi]. \end{aligned} \tag{2.13}$$

The product vE is composed of 21 terms. When this product is averaged over the uniform distribution of ϕ and Φ (equation 8.1, Appendix 8.1, p. 133), most of these terms cancel out, and there remains

$$\begin{aligned} < vE >_{\phi,\Phi} = -\frac{1}{2}\frac{eE_0^2}{m_e\omega}\sin(\omega t) &- \frac{1}{8}\frac{eE_0^2}{m_e(\Omega+\omega)}\sin[(\Omega+\omega)t] \\ &- \frac{1}{8}\frac{eE_0^2}{m_e(\Omega-\omega)}\sin[(\Omega-\omega)t], \end{aligned} \tag{2.14}$$

which is then averaged in time over the free-flight time distribution by using equation 2.8 (equation 8.2 Appendix 8.1, p. 133),

$$P = \frac{(eE_0)^2}{2m_e}\left\{\frac{\nu}{\nu^2+\omega^2} + \frac{1}{4}\left[\frac{\nu}{\nu^2+(\Omega+\omega)^2} + \frac{\nu}{\nu^2+(\Omega-\omega)^2}\right]\right\}, \tag{2.15}$$

which is the expectation value of the power absorbed by an electron moving along x at a velocity v_x, such that its angular frequency of oscillation between the two reflecting walls is $\Omega = \pi v_x/d = 2\pi v_x/\lambda$. Equation 2.15 can be decomposed into two terms $P = P_{\text{ohm}} + P_{\text{stoch}}$ where P_{ohm} and P_{stoch} are the ohmic and stochastic contributions to the total absorbed power, respectively. Note that this decomposition is rather arbitrary and may be argued. Nevertheless, the decomposition presented here is essentially to give a feeling of the significance of stochastic effects compared to the purely collisional effects. The ohmic contribution is obtained by considering that the electron is motionless at the position x; the average power absorbed by this electron is given by equation 2.9, where the amplitude E_0 is replaced by the local amplitude $\hat{E}_0$, given by equation 2.11. This "local" power is then averaged over space between 0 and λ, leading to

$$P_{\text{ohm}} = \frac{3}{4}\frac{(eE_0)^2}{m_e}\frac{\nu}{\nu^2+\omega^2}, \tag{2.16}$$

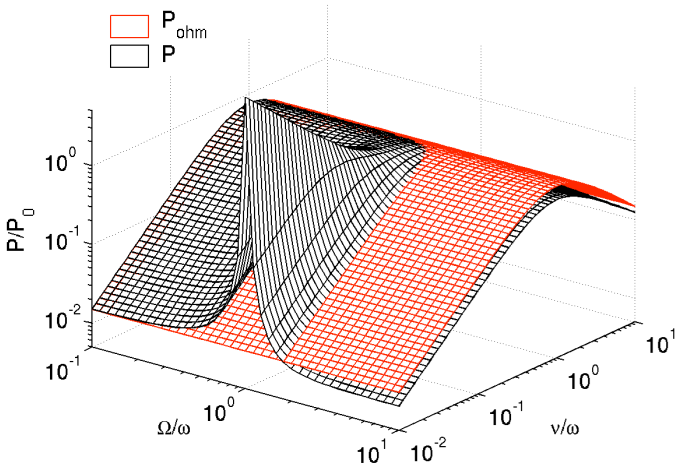

Figure 2.2: 3D mapping of the normalized power P/P_0 absorbed per electron, with $P_0 = (eE_0)^2/(2m_e\omega)$, as a function of Ω/ω and ν/ω.

and thus

$$P_{\text{stoch}} = \frac{(eE_0)^2}{2m_e}\left\{-\frac{1}{2}\frac{\nu}{\nu^2+\omega^2} + \frac{1}{4}\left[\frac{\nu}{\nu^2+(\Omega+\omega)^2} + \frac{\nu}{\nu^2+(\Omega-\omega)^2}\right]\right\}. \tag{2.17}$$

Interestingly, the first term in equation 2.17 is independent of Ω and is always negative. In other words, under certain conditions, electrons may also be "stochastically cooled".

Figure 2.2 shows the normalized power absorbed per electron, as a function of Ω and ν, for a given ac frequency ω. The red and black (or grey and black) surfaces show the ohmic contribution and the total power, respectively. A resonance in the stochastic heating is observed for $\Omega = \omega$. Stochastic cooling is observed for $\Omega/\omega > 1$. However, once again, it should be noted that splitting the total power absorption into two terms (ohmic and stochastic) maybe argued as this really depends on the definitions of these two terms.

At low pressure, when $\nu/\omega \to 0$, the power can be approximated by

$$P \overset{\nu/\omega\to 0}{\sim} \frac{(eE_0)^2}{8m_e}\pi\left[\delta(\Omega+\omega)+\delta(\Omega-\omega)\right], \tag{2.18}$$

where δ is Dirac's function defined by

$$\delta(x) = \frac{1}{\pi}\lim_{\epsilon\to 0}\frac{\epsilon}{\epsilon^2+x^2} \tag{2.19}$$

and having the property

$$\int_{-\infty}^{\infty} f(x)\delta(x-a)\,dx = f(a), \tag{2.20}$$

for any function f.

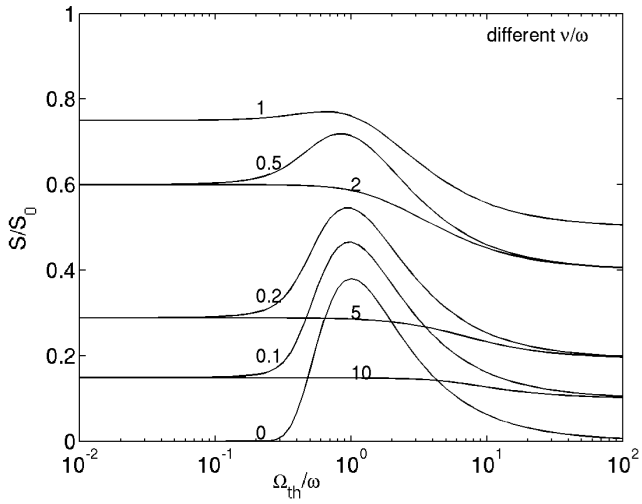

Figure 2.3: Normalized power S/S_0, with $S_0 = (eE_0)^2/(2m_e\omega)$, averaged over a Maxwellian distribution, for various ν/ω from 0 to 10.

When $\Omega/\omega \to 0$, i.e. when the electrons are still (no motion along x), the power can be approximated to first order by

$$P \underset{\sim}{}^{\Omega/\omega \to 0} \frac{3}{4} \frac{(eE_0)^2}{m_e} \frac{\nu}{\nu^2 + \omega^2}, \tag{2.21}$$

which shows that the stochastic contribution vanishes when the electrons are immobile (no motion along x).

2.2.3 Averaging over a Maxwellian distribution

The power derived above (Equation 2.18) is for a particular oscillation frequency $\Omega = 2\pi v_x/\lambda$ along x; here, the power is averaged over Ω, assuming a Maxwellian distribution of the electron velocity v_x. It should be kept in mind that averaging over a Maxwellian distribution seems rather difficult to justify *a priori*. Indeed, the x-directed electron velocity distribution function may well be affected by the heating mechanism itself and be highly anisotropic and non-Maxwellian. Nevertheless, this assumption is kept for the moment and will be verified *a posteriori* with the Monte Carlo simulation. The Maxwellian distribution $f_x(v_x)$ is given by

$$f_x(v_x) = \frac{1}{v_{\text{th}}\sqrt{\pi}} \exp\left(-\frac{v_x^2}{v_{\text{th}}^2}\right), \tag{2.22}$$

where v_{th} is the thermal velocity given by

$$v_{\text{th}} = \sqrt{\frac{2k_B T_e}{m_e}}. \tag{2.23}$$

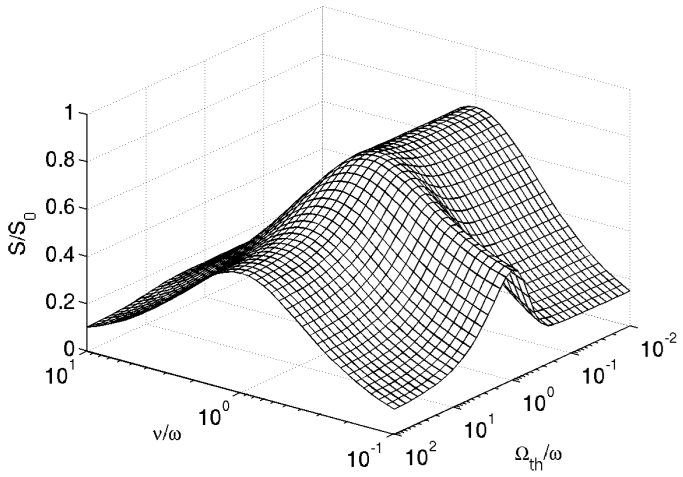

Figure 2.4: 3D mapping of the normalized power S/S_0, with $S_0 = (eE_0)^2/(2m_e\omega)$, averaged over a Maxwellian distribution, as a function of $\Omega_{\rm th}/\omega$ and ν/ω.

Let $S =< P >_{v_x}$ be the total power averaged over a Maxwellian distribution of v_x.

$$S = \int_{-\infty}^{\infty} f_x(v_x) P(v_x)\, dv_x. \tag{2.24}$$

The integration cannot be done analytically in the general case, however, it can be performed in the limit of $\nu/\omega \to 0$, and using 2.18 for $P(v_x)$. The integral $\mathcal{I}^{\pm}$ can be approximated by

$$\begin{aligned} \mathcal{I}^{\pm} &= \int_{-\infty}^{\infty} \frac{\mu}{\mu^2 + (\zeta \pm \xi)^2} \exp\left(-\zeta^2\right)\, d\zeta \\ &\overset{\mu \to 0}{\sim} \pi \int_{-\infty}^{\infty} \delta(\zeta \pm \xi) \exp\left(-\zeta^2\right)\, d\zeta \\ &= \pi \exp\left(-\xi^2\right). \end{aligned} \tag{2.25}$$

In the collisionless case, the power averaged over a Maxwellian is therefore

$$S \overset{\nu/\omega \to 0}{\sim} \frac{(eE_0)^2}{8m} \sqrt{2\pi} \frac{1}{\Omega_{\rm th}} \exp\left(-\frac{\omega^2}{2\Omega_{\rm th}^2}\right), \tag{2.26}$$

where $\Omega_{\rm th}$ is the "thermal" transit frequency through a spatial oscillation of the field amplitude, or the "thermal" frequency of oscillation of the electron along the x direction.

$$\Omega_{\rm th} = \frac{\sqrt{2}\pi v_{\rm th}}{\lambda} = \frac{2\pi}{\lambda}\sqrt{\frac{k_B T_e}{m_e}}. \tag{2.27}$$

Figure 2.3 and 2.4 show the total (ohmic and stochastic) power S absorbed per electron for a Maxwellian distribution of velocity. The collisionless case

where $\nu/\omega \to 0$, was obtained analytically using 2.26, while the other cases are the result of the numerical integration of 2.15 over a Maxwellian distribution of electrons. The power S is normalized and is represented as a function of $\Omega_{\text{th}}/\omega$ proportional to the square-root of the electron temperature. At low pressure ($\nu/\omega < 1$), a resonance of the stochastic contribution is observed for $\Omega_{\text{th}}/\omega = 1$; for example, for an electron temperature of 3 eV and $\lambda = 0.2$, the ac field resonance frequency is $\omega/2\pi \sim$2.5 MHz. At high pressure ($\nu/\omega > 1$), the absorbed power is essentially ohmic.

2.2.4 Power absorbed per electron in a non-uniform ac electric field: abrupt transition

For the work presented in Chapter 3, a non-uniform ac field similar to that described above is used, but the amplitude of the field does not vary smoothly as a cosine function of space, but is a step function

$$\begin{aligned} \hat{E}_0 &= E_0 \quad \text{if } x/d < h, \\ &= 0 \quad \text{otherwise,} \end{aligned} \tag{2.28}$$

where h is the relative "heating length". Let us call $\tau = 2d/v_x$ the oscillation period along x. The same approach as before can be used to express the absorbed power as a function as the relative heating length h and the oscillation period τ. The calculation is rather long and was derived by Hagelaar (2005b) and leads to

$$P = \frac{(eE_0)^2}{2m_e\omega}\left\{\frac{h(\nu/\omega)}{1+(\nu/\omega)^2} + \Pi\left(\Lambda + \Sigma\right)\right\}, \tag{2.29}$$

where

$$\begin{aligned} \Pi =& \frac{1}{\omega\tau\left[1+(\nu/\omega)^2\right]^2\left[\cosh(\nu\tau)-\cos(\omega\tau)\right]}, \\ \Lambda =& 2(\nu/\omega)\left\{\sin(\omega\tau) - \cosh(h\nu\tau)\sin\left[(1-h)\omega\tau\right] - \cosh\left[(1-h)\nu\tau\right]\sin(h\omega\tau)\right\}, \\ \Sigma =& \left[1-(\nu/\omega)^2\right] \\ & \left\{\sinh(\nu\tau) - \sinh(h\nu\tau)\cos\left[(1-h)\omega\tau\right] - \sinh\left[(1-h)\nu\tau\right]\cos(h\omega\tau)\right\}. \end{aligned} \tag{2.30}$$

Equation 2.29 can be numerically integrated over a Maxwellian distribution of v_x, and in the same fashion as in Section 2.2.3, significant stochastic heating is observed at low pressure ($\nu/\omega < 1$), and for a given electron temperature, the efficiency of the heating can be optimized, as there exists an optimal ac field frequency leading to a maximum in stochastic heating.

2.3 Monte Carlo model

In Monte Carlo simulations, a number of individual electrons are followed, one by one, on their way through a plasma or any other medium. The occurrence and effect of collisions, for example with the background gas are treated by random numbers. The principles of Monte Carlo simulations are detailed in Chapter 5, and are not required for the following development.

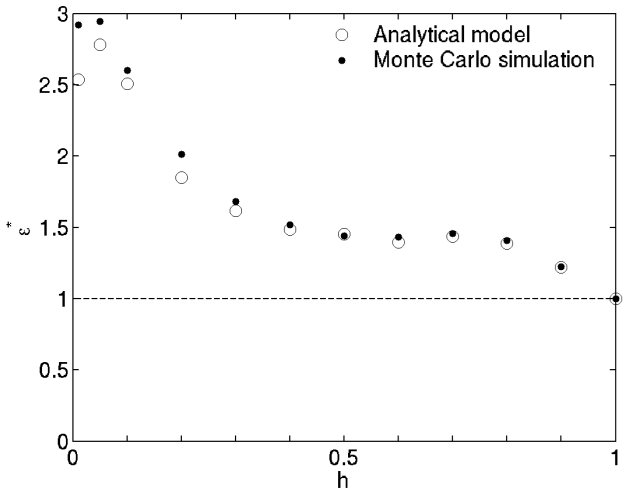

Figure 2.5: Electron mean energy, normalized to the relative heating length h as a function of h; $\mathcal{E}^* = \mathcal{E}/h$, where $\mathcal{E}$ is the electron mean energy, obtained with both the analytical model (open circles) and the Monte Carlo simulation (black dots). The dashed line shows the normalized electron mean energy that an electron would have in a system of length h and a uniform ac electric field (the electron mean energy is proportional to the volume of heating).

2.3.1 Good agreement with the analytical model

By using a Monte Carlo simulation, the situation described in Section 2.2.4 is simulated, namely, the state of an electron trapped between two reflecting walls separated by d =10 cm is measured over a relatively long time scale (300 ms). The electron undergoes elastic isotropic collisions with neutrals at a constant frequency $\nu = 10^7$ s^{-1}. Elastic energy loss only is assumed as in the case of a constant collision frequency, this yields a Maxwellian distribution (as assumed for the analytical model). A relatively large neutral to electron mass ratio is chosen (1000) to ensure that electron-neutral collisions are isotropic in the lab frame, as well as is the center-of-mass frame. The electrons are heated by a non-uniform ac electric field. The amplitude of the field is $E_0 = 20$ V/m for $x < hd$ and null otherwise, and its frequency is $\omega/2\pi = 10$ MHz.

The white circles in figure 2.5 show the electron mean energy predicted by the analytical model (equation 2.29), while the black dots show the mean energy using the Monte Carlo simulation described above. A very good agreement is observed, which is in essence not too surprising as the same quantities were calculated, using two different approaches (an analytical approach and a random-number-based numerical approach). For the analytical approach, the x-directed electron velocity distribution function was assumed to be Maxwellian and this was not justified *a priori*. The results of the Monte Carlo simulation seem to suggest *a posteriori* the validity of this assumption, as well as the validity of the whole analytical model. The dashed line shows the mean energy that an electron subject to a uniform heating over a relative length h would acquire. This shows that electrons can absorb significant power in addition to

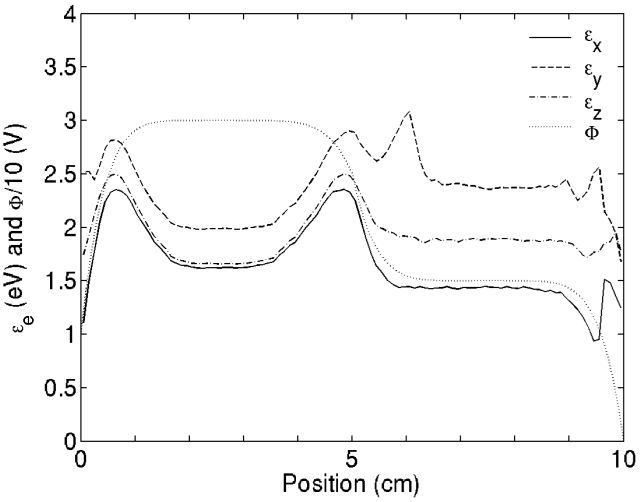

Figure 2.6: Potential profile Φ (dotted line) and directed electron mean energy profiles along the x (solid line), y (dashed line) and z (dashed-dotted line) directions.

classical ohmic power, especially for relatively small heating regions.

2.3.2 Anisotropy introduced by the stochastic heating

The use of the Monte Carlo model above allows one to investigate more complex situations that would not be easily described analytically. For example, consider now a system where the electron parallel motion along the x direction is affected by the presence of a spatially non-uniform electric field $E_x(x)$ (the corresponding potential $\Phi(x)$ is shown by the dotted line in figure 2.6), leading to a time-varying velocity v_x along x. Also, instead of using reflecting boundaries, absorbing boundaries separated by 10 cm are now used. The left-hand side boundary potential is 10 V, while the right-hand side boundary potential is 0 V. Electrons are injected with a spatial distribution following $\exp(\Phi)$ and with a 0.1 eV Maxwellian velocity distribution. Each electron is followed individually until it reaches either wall. Also, although it is not of great relevance here, various electron-neutral collisions, such as elastic, exciting and ionizing collisions are taken into account. Finally, because various energy sinks, such as inelastic collisions, are now considered, the perpendicular ac electric field amplitude is significantly increased in order to balance them and is 150 V/m from 0 to 5 cm and null from 5 to 10 cm.

Figure 2.6 shows the x, y and z-directed electron mean energies. Here, we will not focus on small artifacts of this simple model such as the peculiar behavior of the electron mean energy in the vicinity of the right wall, but rather concentrate on the y-directed (direction of the heating) electron mean energy. The y-directed electron mean energy, seems to be more important where the electrons are not heated. Both, stochastic and ohmic heating introduce anisotropy in the energy. Electrons that can reach the right-hand side of the system are those which have larger parallel energy as they need to climb a

significant potential wall. Energetic electrons are sensitive to stochastic heating as they can reach any region of the system and therefore "see" the nonuniform ac electric field. By contrast, low-energy electrons are electrostatically trapped on the left-hand side, hence are only able to see a uniform ac electric field. Under the present conditions (low-pressure), stochastic heating is more efficient than ohmic heating, hence energetic electrons become "more anisotropic" than those that are trapped on the high-potential side as they are heated more. These "more anisotropic" energetic electrons are present on both sides of the system. This is clearly visible on the low-potential side of the system, where the y-directed electron mean energy $\mathcal{E}_y$ is 1 eV larger than $\mathcal{E}_x$. However, because these "more anisotropic" energetic electrons are much less numerous than the low-energy trapped electrons on the high-potential side, they are much more visible in this region; $\mathcal{E}_y$ is only 0.5 eV larger than $\mathcal{E}_x$. This gives the illusion that, in the heating direction, electrons are somewhat cooler where they are heated than where they are not. This should be kept in mind when using such a heating mechanism in more complex situations (Chapter 3 and 4).

2.4 Discussion and conclusion

In this Chapter, the effects of a non-uniform ac electric electric field, perpendicular to the one-dimensional motion of electrons was investigated by an analytical approach. It was found that, due the non-uniformity of the field, the heating mechanism is much more complex than classical ohmic heating and is dominated by stochastic effects, especially when the neutral pressure is low (collision frequency below the field frequency). This analysis is of particular relevance as most of the simulations that were developed and used for the present thesis make use of such a transverse electric field to model inductive heating; more generally these results are valid in any one-dimensional particle plasma simulation where the electrons are heated by a non-uniform ac electric field perpendicular to the electron motion. However, it should be kept in mind that in real system, the magnetic field associated with the time-varying electric field would presumably change the above conclusions significantly. In future, the possible effects of the magnetic field should be investigated.

Chapter 3

Formation of current-free double layers in one-dimensional particle-in-cell simulations

3.1 Current-free double layers in *Chi-Kung*

An electric double layer[1] (DL) is a narrow localized region in a plasma which can sustain a large potential difference (see Raadu 1989, and references therein). The earliest work on double layers was reported by Langmuir (1929). Alfvén (1958) suggested about 50 years ago that double layers could be responsible for the acceleration of electrons onto the upper atmosphere creating the visible aurora. Evidence supporting Alfven's hypothesis was given by Albert and Lindstrom (1970) and Temerin et al. (1982). Since then, electric double layers have been studied experimentally (Hershkowitz 1985, and references therein), theoretically (Andrews and Allen 1971, Hasan and Ter Haar 1978, Torven 1981, Lieberman and Charles 2006) and by computer simulation (Knorr and Goertz 1974, Goertz and Joyce 1975, Joyce and Hubbard 1978, Newman et al. 2001). In most of these cases, the double layer is created by imposing a potential difference or by drawing a current through the system.

Until the late 1970s, it was commonly believed that a necessary condition for the formation of double layers was that the electron drift velocity had to exceed the electron thermal velocity. Evidence supporting this assumption were obtained theoretically (Knorr and Goertz 1974), by computer simulations (Goertz and Joyce 1975, DeGroot et al. 1977) and laboratory experiments (Quon and Wong 1976, Coakley et al. 1978). However, Mozer et al. (1977) observed large potential drops along the auroral field lines, where the electron drift velocity was much less than the electron thermal velocity, suggesting that the absence of a (large) current was not in contradiction with the formation of double layers. Inspired by this peculiar observation, Sato and Okuda (1980) showed, by us-

[1] "Double layers" are also referred to as "double sheaths" or "internal sheaths".

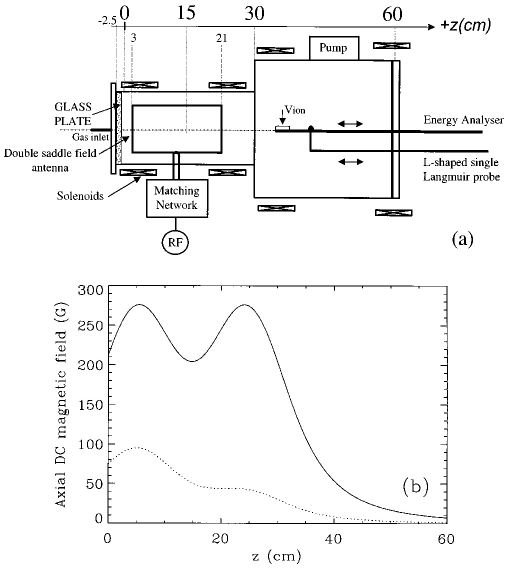

Figure 3.1: (a) Schematic of *Chi-Kung*, a horizontal helicon system, showing major components and (b) B_z component of the dc magnetic field along axis for the high (solid line) and low (dotted line) field cases (Charles and Boswell 2003).

ing a particle-in-cell simulation with periodic boundary conditions, that double layers may form even if the electron drift velocity was smaller than the electron thermal velocity.

Perkins and Sun (1981) were the first ones to suggest over 20 years ago, by an analytical model, that current-free (with no net current at all) double layers could exist. The authors found solutions of the Vlasov equation that would satisfy a set of conditions, such as the existence of an abrupt potential drop surrounded by quasi-neutral plasma with no electric field.

Hatakeyama et al. (1983) seem to be the first ones to report an experimental stable current-free double layer. However, in their experiment, although the double layer was not imposed by drawing a current through the plasma or by imposing a potential difference, the double layer was forced by creating two plasmas with two different temperatures interacting with each other.

Hairapetian and Stenzel (1990) have also reported the experimental formation of stationary current-free double layers. In their experiment, a very-low-pressure two-temperature plasma was created and allowed to expand into a longer chamber. By carefully adjusting the two distinct temperatures, the authors could form a stationary double layer. However, this double layer was "only" stationary during the duration of the pulse, i.e. for 1 ms. Sato and Miyawaki (1992) have theoretically investigated a situation similar to that of Hairapetian and Stenzel (1990), that is a plasma composed of two populations of electrons with two distinct temperatures. These authors have derived a minimal electron temperature ratio compatible with a double layer.

Charles and Boswell (2003) showed that a stationary[2] double layer could

[2] "Stationary" means that the double layer stays there once it is created, as opposed to the double layer formed by Hairapetian and Stenzel (1990), which is stationary "only" during the

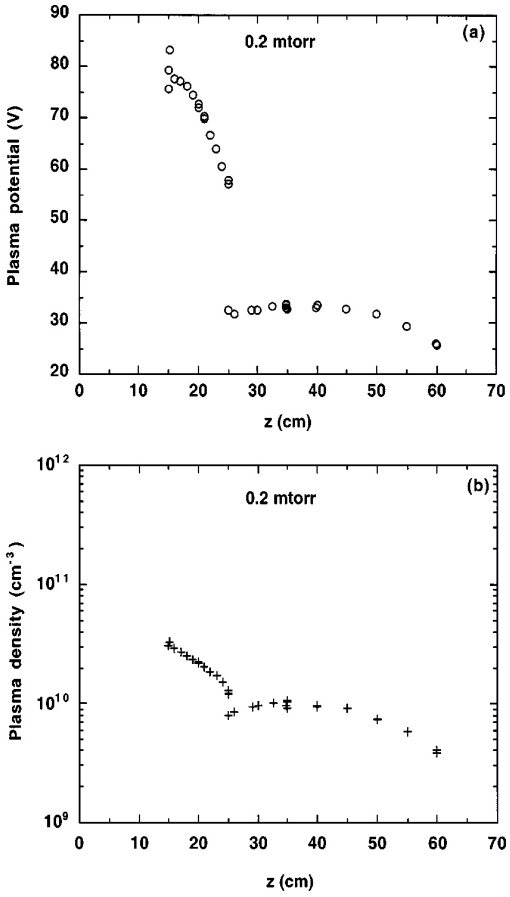

Figure 3.2: (a) Plasma potential and (b) plasma density measured with the energy analyzer along the z-axis for 0.2 mTorr pressure, 250 W rf power and high field [figure 3.1(b)] conditions, respectively (Charles and Boswell 2003).

spontaneously form in a current-free plasma, expanding along a diverging magnetic field. The first current-free double-layer experiment was performed in the horizontal helicon system, *Chi-Kung* (Charles and Boswell 2003) shown in figure 3.1. It consists of a 15-cm-diameter, 31-cm-long helicon source joined contiguously to a 32-cm-diameter, 30-cm-long grounded aluminum diffusion chamber. Two solenoids around the source are used to create a magnetic field of about 130 G[3] in the source center decreasing to a few tens of gauss in the diffusion chamber. The current-free double layer, shown in figure 3.2, can be generated for pressures less than about 1 mTorr. A supersonic ion-beam has been measured downstream of this double layer for both argon (Charles and Boswell 2004a, Charles 2005b) and hydrogen (Charles 2004) discharges. Charles and Boswell (2004b) showed that the current-free double layer was formed in the first 100 μs of the discharge; Charles (2005a) also showed that this was accompanied by some charging of the source walls. The current-free double layer has many potential applications, such as in plasma processing (Charles 2006), plasma propulsion (Gesto 2005, Gesto et al. 2006, Charles et al. 2006) and space plasma (Boswell et al. 2006).

The formation of double layers in current-free plasmas and associated ion beams were confirmed by similar experiments (Cohen et al. 2003, Sun et al. 2004, Sutherland et al. 2005). In particular, Sutherland et al. (2005) showed that the double-layer strength could be scaled by a factor of at least 2 in a bigger system and that the double layer presumably forms in the vicinity of maximal gradient of the magnetic field.

In this chapter, particle-in-cell simulation techniques are used to investigate the possibilities of forming double layers in current-free plasmas. The original aims of the simulation were i) to gain insight in the fundamental mechanisms underlying the formation of the current-free double layer observed by Charles and Boswell (2003) (this chapter) and ii) to investigate the particle transport, and especially the formation of an ion beam, in a current-free double-layer plasma (Chapter 4).

3.2 Particle-in-cell simulations

3.2.1 Introduction and background

The particle-in-cell (PIC) scheme is a purely kinetic representation of a system containing ions and electrons, allowing a self-consistent representation of virtually any plasma.

Birdsall (1991) and more recently Verboncoeur (2005) have written two comprehensive and very interesting reviews on particle-in-cell simulations. Both of them include roots of particle simulations and the basic techniques. Verboncoeur's review also treats recent advances made in the field.

duration of the pulse, i.e. 1 ms.

[3]The B field reported in the earliest papers on the current-free double layer by Charles and Boswell were wrong by a factor of two; the maximal value of the field was 130 G in the source and not 250 G as shown in figure 3.1.

The early days of particle simulations go back to calculations performed by Buneman (1959) and Dawson (1962) with only a few hundreds of particle electrons to study instabilities and thermalizing properties, respectively. In these models, the electrical forces due to the space charges were calculated using Coulomb's law. These models are referred to as particle-particle models, as the interactions between a particle and all the others are taken into account, which is, of course, very computationally expensive. This was improved by the use of particle-mesh models, where the charges are accumulated on a spatial grid on which Poisson's equation is solved; these models are referred to as cloud-in-cell or particle-in-cell.

The development of modern PIC took place in the late 1960s (Birdsall and Fuss 1969), 1970s (Langdon and Birdsall 1970) and early 1980s. The earliest work attempting to include Monte Carlo collisions (electron-neutral collisions) in a PIC simulation was done by Burger (1967) and led to many subsequent works (Vahedi et al. 1993ba, Vahedi and Surendra 1995). Most of the theoretical work on the effects of the spatial grid (Langdon and Birdsall 1970) and the analysis of the time integration (Langdon 1979) was done in the 1970s. Techniques used in modeling bounded plasmas have been well described in a number of books and publications (Hockney and Eastwood 1988, Birdsall and Langdon 1985, Vahedi et al. 1993ba). For many years plasma simulations were used to simulate the plasma bulk, neglecting the sheaths, hence, the use of periodic boundary conditions was very popular. Realistic absorbing boundary conditions were first introduced by Birdsall and Langdon (1985), and improved by the use of electron secondary emission (Hagstrum 1956, Harrower 1956, Surendra et al. 1990, Surendra et al. 1990) and by the inclusion of an external circuit (Verboncoeur et al. 1993) for a more accurate representaion of processing systems.

The time step and the cell size of full particle-in-cell simulations, where both ions and electrons are treated as particles, have to resolve both the electron plasma frequency and the Debye length, to ensure stable and accurate simulations. These extremely stiff conditions become a real issue when simulating high density plasmas, as the plasma frequency is proportional to the square root of the plasma density. In addition, when dealing with phenomena related to ion transport or whose time scale is large, for example on the order of millisecond, full particle-in-cell simulations become really cumbersome, as they can require several billions of time steps and several days of calculation. Increasing the speed of particle-in-cell simulations is a challenging issue that has been going on for years. As early as in the beginning of the 1980s, Cohen and Freis (1982) and Langdon et al. (1983) have developed a so-called implicit scheme for PIC simulations allowing use of larger time steps than with the classical explicit scheme. Accelerating PIC simulation can also be done by the use of adaptive grids and time scales, electron sub-cycling (Adam et al. 1982), consisting of moving the much heavier ions less often than the electrons. More recently, the use of variable macro-particle weight (Coppa et al. 1996, Shon et al. 2001) was developed. A very interesting review on physical and numerical technics to accelerate full PIC simulation was written by Kawamura et al. (2000). In Chapter 5, an alternative to accelerate PIC simulation is proposed.

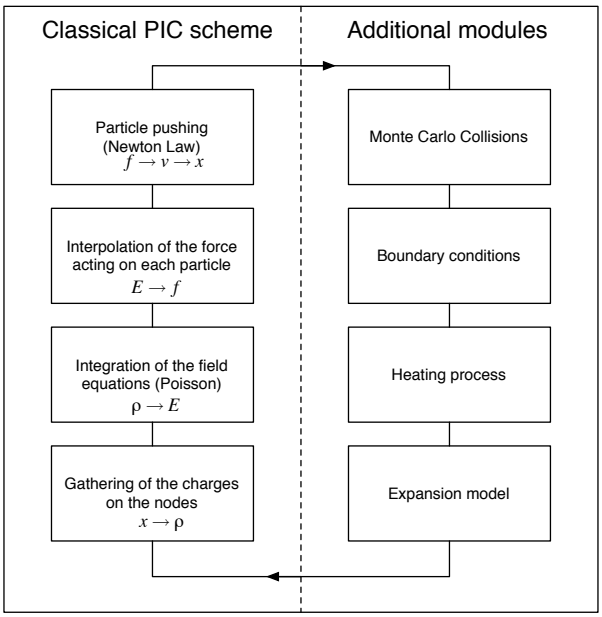

Figure 3.3: Classical particle-in-cell (PIC) scheme and extra modules.

As other kinetic methods, PIC is very attractive since it provides a self-consistent solution of the fields and particle dynamics using only first principles (Poisson's equation and Newton's law) without making any assumptions on the charged particle transport. Particle-in-cell simulations are particularly useful when modeling non-equilibrium plasmas, such as breakdown (Vender et al. 1996) or when modeling plasmas for which the electron transport is not known *a priori*. The use of PIC simulations generally falls into one of the following two categories. i) PIC can provide insight in areas where the theory is incomplete or inaccurate or when its assumptions cannot be verified experimentally. ii) PIC can be used as an extension to experiment and compared directly to experiment, giving results to clarify or explain the underlying mechanisms involved in some experimental plasmas. This second category is still limited by the complexity of the real plasma chemistry, the more or less complex geometry of the system, the real surface behavior etc., that have to be simplified to make the simulation tractable.

3.2.2 General particle-in-cell scheme

Particle-in-cell is a purely kinetic representation of a system containing ions and electrons, considered as individual particles, moving under the influence of their own self-consistent electric field (Birdsall and Fuss 1969, Langdon and Birdsall 1970, Hockney and Eastwood 1988, Birdsall and Langdon 1985). PIC simulations use the first principles (Poisson's equation and Newton's laws) only. Each particle of the simulation is actually a macro-particle allowed to represent a large number of real particles (on the order of 10^9 or 10^{10} particles per macro-particle for one-dimensional simulations; this number can be decreased even more with the improvement of computational resources) and which can move inside the

simulated domain. With a small number of these macro-particles (typically between 10^4 and 10^5 for one-dimensional simulations), a realistic steady-state plasma can be obtained in a few hours on a modern desktop computer.

Let us describe the general one-dimensional PIC scheme assuming a planar geometry. The simulated region is divided into N_c cells resulting in a grid of $N_c + 1$ nodes. Electric field only is considered (electrostatic simulation), thus each particle is pushed (accelerated and moved) using Newton's law

$$m\frac{dv}{dt} = qE, \tag{3.1}$$

where m is the mass of the particle, q its charge and v its velocity. The electric field E is given by

$$E = -\frac{\partial \Phi}{\partial x}, \tag{3.2}$$

and where the potential Φ is integrated from Poisson's equation

$$\frac{\partial^2 \Phi}{\partial x^2} = -\frac{\rho}{\varepsilon_0} = -\frac{e}{\varepsilon_0}(n_i - n_e), \tag{3.3}$$

where n_i and n_e are the ion and the electron densities, respectively; e is the elementary charge and ε_0 the vacuum permittivity. Physical quantities, such as the potential, the electric field, the position, the velocity. are normalized according to the characteristic quantities of the system, such as the cell size Δx, the time step Δt, the elementary charge e etc. Scaling the physical quantities i) decreases the number of operations, such as multiplications by physical constant ii) and minimizes round-off errors.

The steps of the conventional PIC scheme with additional modules are summarized in Figure 3.3 and are described below.

Charge assignment and field interpolation

The charge density ρ is assigned to each node of the grid by accumulation of the charges of the various species (electrons and ions). The accumulation of the charges can be done following various models such as Nearest-Grid-Point (NGP), Cloud-in-Cell (CIC) etc. These models are discussed in detail in Hockney and Eastwood (1988) and Birdsall and Langdon (1985).

It is generally accepted that the best tradeoff between computational cost and accuracy is the CIC scheme. It is a first-order weighting model involving the two nearest grid points. The charge density on each mesh point is calculated by linearly distributing the charge of each macro-particle to its two nearest grid points. Likewise, the electric field at a given position is obtained by interpolating the two nearest field values.

Charge gathering and evaluation of the electric field at the position of a macro-particle have to use the same interpolation kernel (NGP, CIC etc.), as it was shown that using different interpolation kernels leads to *self-forces*[4] (Birdsall and Langdon 1985) and higher heating rates (Mardahl and Verboncoeur 1997).

[4] *Self-force* means that a charged particle creates a force on itself.

Electric potential and electric field on the nodes

The electric potential is calculated by solving Poisson's equation discretized as follows

$$\frac{\Phi_{i-1} - 2\Phi_i + \Phi_{i+1}}{\Delta x^2} = -\frac{\rho_i}{\varepsilon_0}, \tag{3.4}$$

where Δx is the cell length and i the index of the considered node. Equation 3.4 leads to a tri-diagonal system of equations, which can be solved by any classical algorithm for tri-diagonal systems (see Press et al. 1992, for example). The electric field is then obtained by using the following finite-difference equation

$$E_i = -\frac{\Phi_{i+1} - \Phi_{i-1}}{2\Delta x}. \tag{3.5}$$

For the first (resp. last) node, the electric field is a linear extrapolation of the field of the second and third (resp. penultimate and antepenultimate) nodes; various boundary condition models are proposed and discussed by Verboncoeur et al. (1993).

Particle pushing

Particles are accelerated by integrating Newton's law (equation 3.1) discretized as follows

$$v_{t+\frac{1}{2}} = v_{t-\frac{1}{2}} + \frac{qE_t\Delta t}{m}. \tag{3.6}$$

Particles are then moved according to

$$x_{t+1} = x_t + v_{t+\frac{1}{2}}\Delta t. \tag{3.7}$$

Equations 3.6 and 3.7 lead to the classical leap-frog scheme where positions and velocities are not known simultaneously.

To allow stable and accurate simulations of cold plasmas, the time step and the size of the cell have to meet the following criteria (Birdsall and Langdon 1985, Hockney and Eastwood 1988)

$$\begin{aligned} \omega_p\Delta t &\ll 2, \\ \Delta x &< \lambda_D, \end{aligned} \tag{3.8}$$

where ω_p is the electron plasma frequency

$$\omega_p = \sqrt{\frac{n_e e^2}{m_e\varepsilon_0}}, \tag{3.9}$$

and λ_D the Debye length

$$\lambda_D = \sqrt{\frac{\varepsilon_0 k_B T_e}{e^2 n_e}}. \tag{3.10}$$

Table 3.1: Electron-neutral and ion-neutral collisions in argon.

Elastic scattering	$e + Ar \rightarrow e + Ar$
Excitation	$e + Ar \rightarrow e + Ar^*$
Ionization	$e + Ar \rightarrow e + Ar^+ + e$
Charge exchange	$Ar^+ + Ar \rightarrow Ar + Ar^+$
Elastic scattering	$Ar^+ + Ar \rightarrow Ar^+ + Ar$

Monte Carlo Collisions

Although it was recently shown by Turner (2006) that, under certain conditions, it may seriously degrade kinetic properties of the PIC, neutral-charged particle collisions in a PIC simulation are commonly handled by a Monte Carlo Collision scheme (MCC). The usual Monte Carlo[5] (MC) technique makes use of random number sequences for the modeling of stochastic events; the way collision events are treated by MC is fully described in Chapter 5. Although only one spatial dimension is considered in the simulation, collisions are in essence a three-dimensional phenomenon, hence particle are followed keeping the three dimensions of velocity; this kind of model is commonly referred to as 1D3V.

In the particular PIC developed here, the MCC model developed by Vahedi and Surendra (1995) for the various collisions in argon was implemented. Table 3.1 shows the collisions which are taken into account in this model; this includes electron-neutral collisions (elastic, exciting and ionizing) and ion-neutral collisions (elastic and charge exchange). In short, high-energy electron-neutral collision scattering angles are very small (forward scattering), while low-energy electron-neutral collisions are isotropic. At high energy (more than 1 eV) ion-neutral charge exchange collisions are predominant and are anisotropic in the center-of-mass frame. At low energy, ion-neutral elastic collisions are dominant and are isotropic in the center-of-mass frame.

Accurate electron-neutral and ion-neutral collision cross sections are used to ensure realistic simulations; data can be found in Tachibana (1986) and Pack et al. (1992) for electron-neutral collisions and in Phelps (1994) for ion-neutral collisions. The cross sections of the various collisions are shown in figure 5.8 and 5.2 (Chapter 5). Coulomb collisions are not included in the present study.

3.3 Simulation of an inductively coupled plasma

The classical PIC/MCC scheme presented above was implemented; for the present work, absorbing boundaries that can be either floating[6] or grounded were used. Two extra modules that were developed for the double-layer investigation, namely a heating mechanism and a double-layer model, are presented in this section and the following section, respectively. The implementation of

[5] The name Monte Carlo is a reference to the famous casinos.

[6] For the floating boundary, we include a capacitor in series on the left-hand side wall. Note that the boundary is not *strictly* floating as a capacitor can conduct current at high frequency.

the whole model, developed for the present thesis, is called *JanuS*[7], the code is multi-platform, object-oriented and written in C++. *JanuS* is made available as a package, including a comprehensively commented input file.

As it was chosen to model real ionization events (rather than simply "dropping" new particles into the simulation), a source of energy has to be provided: the electrons have to be heated. One-dimensional PIC simulations are commonly concerned with capacitive coupling, where an rf voltage of some hundreds of volts is applied to one of the boundaries. This mechanism has been thoroughly studied (Vender 1990, Vender and Boswell 1990, Lieberman and Lichtenberg 2005) and creates a moving sheath that heats the electrons. The drawback of this process is that it leads to strongly affected plasma potentials and electron distributions.

In this section, an adaptation to PIC simulations of the transverse heating mechanism introduced in Chapter 2 is presented. This scheme is intended to model inductive excitation, similar to that described by Turner (1993), but without solving electromagnetic field equations; this scheme has been published by Meige et al. (2005a). Some advantages of this scheme are that it avoids rf excursions of the plasma potential, characteristic of capacitive coupling and is somewhat closer to the current-free double-layer experiment.

3.3.1 Inclusion of a transverse rf field in 1D PIC simulations

An rf electric field E is applied in the direction perpendicular to the spatial dimension x of the PIC allowing the electrons to heat in the y direction, momentum and energy being transferred to the other x and z directions via electron-neutral collisions.

The amplitude E_0 of the electric field is a step function of space: it is finite in the "source" (left half of the simulation) and zero in the "diffusion chamber" (right half of the simulation). The main difference with the perpendicular heating introduced in Chapter 2 is that the electric field amplitude is not constant in time to avoid electron overheating: with a constant electric field amplitude the work done by the electric field would increase with the electron density, which is non physical and would lead to unstable simulations. Instead, the current amplitude J_0 is chosen to be the control parameter fixing the electric field amplitude. The total current density J in the source is

$$J = J_0 \sin(\omega_0 t) = J_d + J_c, \tag{3.11}$$

where ω_0 is the electric field frequency; the displacement current J_d and the conduction current J_c are given by

$$\begin{aligned} J_d &= \varepsilon_0 \frac{\partial E}{\partial t}, \\ J_c &= e\Gamma_e, \end{aligned} \tag{3.12}$$

where Γ_e is the y-directed electron flux. Equation 3.11 is integrated over the source region. The integral of the displacement current and total current

[7] *Janus* is the Roman god of gates and doors, beginnings and endings, and hence represented with a double-faced head, each looking in opposite directions.

$J_0 \sin(\omega_0 t)$ are trivial, as the electric field and J_0 are uniform in the source; the integral of the conduction current comes simply from the summation of the y-directed velocities over the particles in the source region. Finally this yields

$$\frac{\partial E}{\partial t} = \frac{1}{\varepsilon_0} \left[J_0 \sin(\omega_0 t) - e\Gamma_e \right]. \tag{3.13}$$

The perpendicular electric field E, is simply evaluated numerically at each time step of the PIC simulation by using the finite difference corresponding to 3.13 that is incorporated in the PIC scheme by using an expression similar to 3.6, but for the y-directed velocities and only for the electrons being in the source. Because of their large mass the ions[8] are not affected by the rf field; hence to save computer time, the heating algorithm simply does not apply to them.

3.3.2 The transverse heating mechanism in practice

In the following, it is shown that the introduction of the transverse heating mechanism in the PIC simulation allows a stable plasma to be sustained without introducing any noticeable pathology; this is done by conducting a set of simulations where the heating region (source) is located in the left half of the 10-cm-long system, with a current density of J_0 =100 A/m^2 and an rf frequency of $\omega_0/2\pi = 10$ MHz.

The simulations are allowed to run for several thousand rf cycles in order to reach a high degree of convergence. The number of macro-particles used is between 150 000 and 200 000, with 250 cells along the x axis and a time step of 5×10^{-11} s, allowing the simulations to meet the well-known stability and accuracy criteria of the PIC scheme (equation 3.8).

Figure 3.4 shows the plasma potential profiles along the axis of the simulation, for various positions of the heating region and a neutral pressure of 1 mTorr. For relatively large source regions (larger than a quarter of the system in the present conditions) the plasma potential is quite uniform and symmetrical about the center of the simulation (solid, dashed and dotted-dashed lines).

Figure 3.5 shows the plasma potential profiles along the axis of the simulation for various neutral pressures ranging from 0.5 to 5 mTorr and where the heating region is located in the first quarter of the system, from 0 to 2.5 cm. When the neutral pressure is increased, the plasma potential ceases being symmetrical and the potential decreases away from the source. The electron energy distribution function of such "inductively" coupled plasmas and the possibilities of stochastic heating are investigated in detail in Chapter 4.

Finally, it should be pointed out that although this inductive heating scheme works, it may well be improved and made more realistic. For example, rather than having an abrupt transition between the heating region and the field free region, it may be more realistic to have an exponentially decaying electric field amplitude. Also, and as it was already mentioned in Chapter 2, it was shown that, in reality, the magnetic field associated with the electric field rotates the

[8] For argon, the ion mass is almost five orders of magnitude greater than that of the electrons.

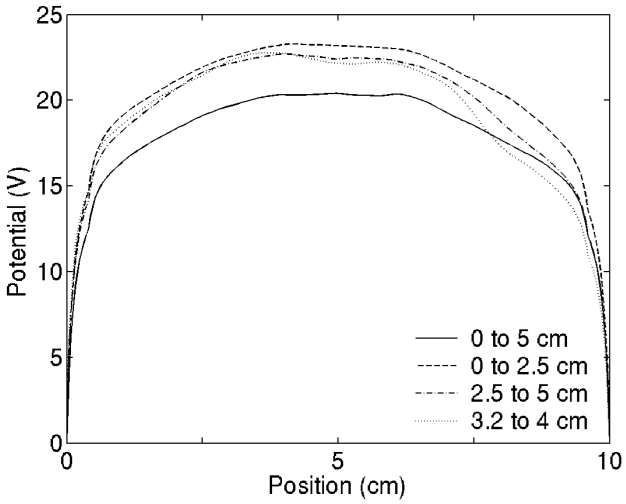

Figure 3.4: Plasma potential spatial profiles for various positions of the heating region and a neutral pressure of 1 mTorr.

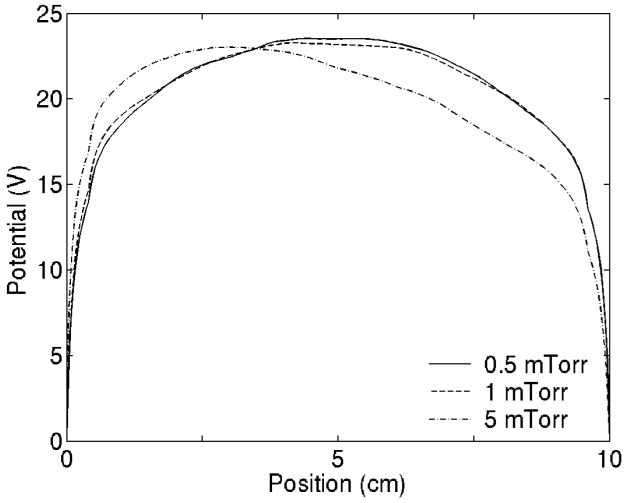

Figure 3.5: Plasma potential spatial profiles for various neutral pressures; the heating region is located in the first quarter of the system, from 0 to 2.5 cm.

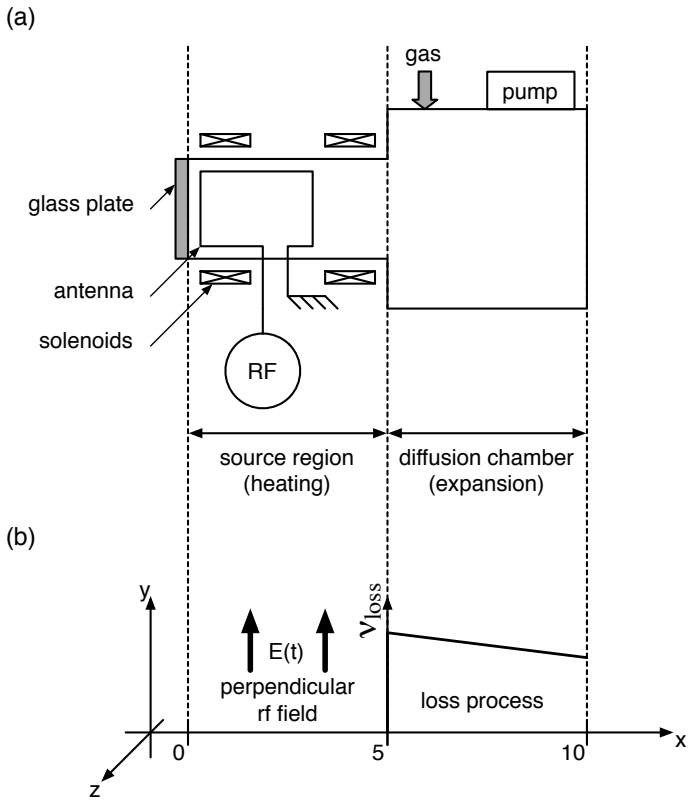

Figure 3.6: (a) Schematic of *Chi-Kung*, the helicon system where the current-free double layer was measured experimentally for the first time (Charles and Boswell 2003). (b) One-dimensional numerical model to form a current-free double layer. In the simulation, the electrons in the source are heated by a uniform rf electric field perpendicular to the spatial dimension of the simulation and the double layer is created by a particle loss process in the diffusion chamber; the loss process creates a density drop and an associated potential drop, with the properties of a double layer.

"kick" in the direction of the electron motion irrespective of the electric field direction (Aliev et al. 1997, Cohen and Rognlien 1996ba). This effect is not considered in the scheme presented above and could be included in a more sophisticated one.

3.4 Formation of the current-free double layer[9].

To form a current-free double layer, an energy-independent particle loss process was introduced into the PIC scheme. The particle loss process removes electron-ion pairs in the same vicinity, following a certain loss frequency profile ν_{loss}[10]. The loss frequency that was used is a function of space and was typically null in the source (left-hand side of the simulation), maximum at the source-diffusion chamber interface and slightly decreasing in the diffusion chamber (right-hand

[9]This section, in slightly altered form, has been published in Meige et al. (2005a)
[10]The loss frequency is a loss probability per unit of time.

Table 3.2: Standard parameters of the simulation.

Quantity	Value
neutral pressure	1 mTorr
rf frequency ($\omega_0/2\pi$)	10 MHz
current density amplitude (J_0)	100 A/m^2
system length	10 cm
cell number	250
total duration	25-100 μs
time step	5×10^{-11} s
ion mass (argon)	6.68×10^{-26} kg
room temperature	297 K
capacitance	22 nF

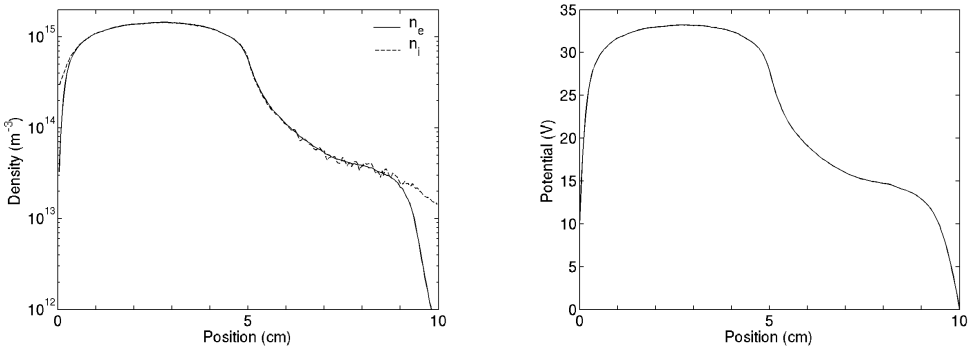

(a) **(b)**

Figure 3.7: Typical PIC simulated current-free double layer: (a) plasma density and (b) plasma potential as a function of positions.

side of the simulation); this is shown in the schematic 3.6(b). Although the loss process does not present any obvious physical justification and does not explain the current-free double layer observed by Charles and Boswell (2003), it produces an axial decrease in the plasma density and an associated potential drop with the properties of a current-free double layer.

3.4.1 Development of the steady state

Simulations are initiated by loading a certain number of macro-particles (typically 10 macro-particles of each species per cell) between the floating left wall and the earthed right wall and are allowed to run for several hundred of, even thousand of, rf cycles in order to reach high degree of convergence. The standard parameters that were used are shown in table 3.2 and the typical plasma densities that were dealt with were on the order of 10^{15} m^{-3} in the source, which is an order of magnitude smaller than in the experiment.

Figure 3.7 shows the density and potential profiles with the standard pa-

rameters (table 3.2) and a loss frequency of 10^{-6} s^{-1} at the source-diffusion chamber interface. The plasma density and potential profiles are averaged over 10 rf cycles and given with respect to the grounded wall. Similar structures are observed in both the densities and the potential: the electron density decreases by an order of magnitude from the source region (upstream plasma) to the diffusion chamber (downstream plasma). The density drop is locally accompanied by a breakdown of quasi-neutrality. The electron to ion mass ratio $m_e/m_i \sim 1.4 \times 10^{-5}$ is much smaller than the relative deviation from quasi-neutrality $\Delta n/n \sim 5 \times 10^{-2}$, where Δn is the average deviation from the exact charge neutrality and n the plasma density. Hence, the density drop and the associated potential drop have the characteristic of a double layer (Block 1978, p. 68).

The upper and lower limits of the non-neutral region are used to precisely determine the width and the position of the double layer and evaluate the density and potential drops. The potential drop associated with the density drop is ∼12 V and is accompanied by a charging of the source of about 10 V. Commonly, double layers are characterized by the ratio $e\Phi_{DL}/k_BT_e$ and the thickness over which the potential drop occurs. In the present case $e\Phi_{DL}/k_BT_e \sim 2.8$, a characteristic of strong[11] double layers [12], and its thickness is less than 20 Debye lengths, which is rather small.

Let us derive the expected double-layer potential drop as a function of the density drop and the current through the double layer by adapting the classical derivation of the sheath potential to the present case (see Lieberman and Lichtenberg 2005, p. 172). $\Delta\Gamma$ is the net current through the double layer

$$\Delta\Gamma = \Gamma_e - \Gamma_i, \tag{3.14}$$

where Γ_e and Γ_i are the electron and ion fluxes through a plane located at the downstream edge of the double layer. The ions are assumed to be collisionless in the double layer since their mean free path under the present conditions is approximatively 3 cm, which is much larger than the double-layer thickness. The ions are assumed to enter the double layer with the sound speed c_s (discussed in Chapter 4)

$$c_s = \sqrt{\frac{k_BT_e}{m_i}}, \tag{3.15}$$

where m_i is the ion mass. The ion flux is then given by

$$\Gamma_i = \alpha n c_s, \tag{3.16}$$

where n is the downstream density and α the upstream to downstream density ratio. The electrons are assumed to be Maxwellian (discussed in Chapter4) and their net flux is given by the sum of the flux coming from the upstream side

[11] Although laboratory double layers of such a strength are generally qualified as being *strong*, the space plasma physicist community would qualify the present double layer as being *weak*.

[12] For the ratio $e\Phi_{DL}/k_BT_e$, the downstream "Boltzmann temperature" obtained in Chapter 4, i.e. $T_e = 4.2$ eV, was used.

and the flux coming from the downstream side

$$\Gamma_e = \frac{1}{4} n \overline{v_e} \left[\alpha \exp\left(-\frac{e\Phi_{\mathrm{DL}}}{k_B T_e} \right) - 1 \right], \tag{3.17}$$

where Φ_{DL} is the potential drop across the double layer and $\overline{v_e}$ is the electron mean energy equal to

$$\overline{v_e} = \sqrt{\frac{8 k_B T_e}{\pi m_e}}. \tag{3.18}$$

Substituting equations 3.16 and 3.17 into 3.14 and rearranging yields

$$\frac{e\Phi_{\mathrm{DL}}}{k_B T_e} = -\ln\left(\gamma + \sqrt{\frac{2\pi m_e}{m_i}} + \frac{1}{\alpha} \right), \tag{3.19}$$

where γ is the ratio between the net current $\Delta\Gamma$ and the upstream electron current $\Gamma_{\mathrm{e,up}}$

$$\gamma = \frac{\Delta\Gamma}{\Gamma_{\mathrm{e,up}}} = \frac{\Delta\Gamma}{\frac{1}{4}\alpha n \overline{v_e}}. \tag{3.20}$$

As the double layer is current free (discussed later), $\gamma = 0$. For $\alpha < 20$, equation 3.19 can be approximated within a 5% error by

$$\frac{e\Phi_{\mathrm{DL}}}{k_B T_e} \sim \ln \alpha, \tag{3.21}$$

Under the present conditions, $\alpha \sim 15$, hence $e\Phi_{DL}/k_B T_e \sim 2.7$, which is in good agreement with the value measured in the simulation (see above) and the experiment (Charles and Boswell 2003).

When α becomes very large, the influence of the downstream plasma is negligible, the asymptote of equation 3.19 is the classical wall sheath potential, where $e\Phi_{DL}/k_B T_e \sim 4.7$ for argon.

Figure 3.8 shows the time development of the current-free double layer. Although the potential drop can be observed at the very beginning of the discharge, a solitary propagating ion acoustic wave forms in the first μs of the simulation in the vicinity of the potential drop and propagates away towards the diffusion chamber at approximatively the ion sound speed and dies somewhere in the downstream plasma. The double layer forms and reaches a steady state after approximatively 15 μs, which is much faster than experimentally observed, where the double layer seems to form in ~ 100 μs (Charles and Boswell 2004b). But once again, the real mechanisms underlying the experimental double layer are presumably very different from a simple particle loss process.

3.4.2 Current-free nature of the double layer

Figure 3.9 shows the plasma potential profiles for loss frequencies, from 0 to 10^6 s^{-1}. For a loss frequency of 10^6 s^{-1} (dotted line) a double layer with a potential drop of around 12 V over a distance of less than 20 Debye lengths is observed, while no double layer is observed below about this threshold. Double layers are generally thick compared to the Debye length λ_D, their width is

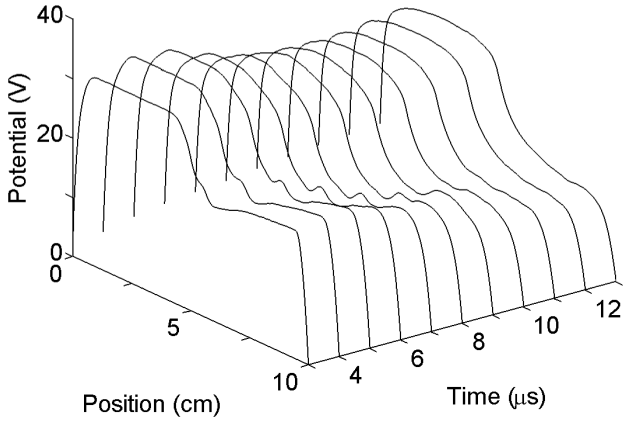

Figure 3.8: Time evolution of the plasma potential profile at the formation of the double layer. A solitary wave formed in the vicinity of the low potential-side of the double layer and propagating towards the right wall is observed. It propagates at about the ion sound speed and decays away from the double layer.

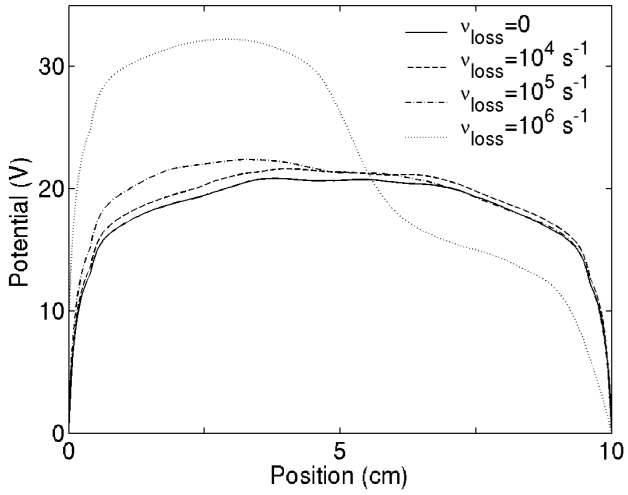

Figure 3.9: Plasma potential spatial profiles for various loss frequencies, ranging from 0 to 10^6 s^{-1}, at a pressure of 1 mTorr.

Table 3.3: Electron temperatures T_e in the double-layer particle-in-cell simulations for various neutral pressures P, and corresponding rate coefficients R and ionization frequencies ν_{iz} .

P (mTorr)	0.1	1	10
T_e (eV)	38	6	4
R ($\times 10^{-15}$ m^3/s)	100	5	1
ν_{iz} ($\times 10^5$ Hz)	3.3	1.6	3.3

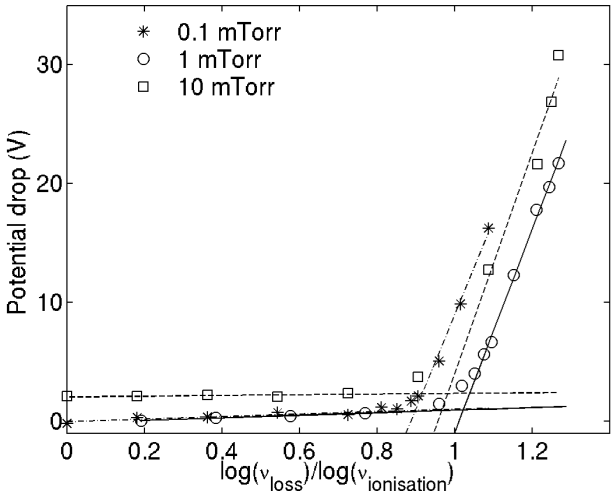

Figure 3.10: Double-layer potential drop as a function of the loss frequency, normalized to the ionization frequency.

generally on the order of $\sqrt{m_i/m_e}\lambda_D$, which is $\sim 270\lambda_D$ in argon; however, double layers whose thickness was $30\lambda_D$ have been observed in argon (Block 1978). By changing the shape of the loss frequency profile, the thickness of the double layer can be increased, but cannot be reduced further.

Figure 3.10 represents the double-layer potential drop as a function of the loss frequency normalized to the ionization frequencies, given in table 3.3, for various neutral pressures ranging from 0.1 to 10 mTorr. No potential drop is observed for loss frequencies below the ionization frequency, while above this threshold, the potential drop is proportional to the logarithm of the loss frequency; this was recently confirmed by Lieberman (2006a, private communication) using his analytical model of the current-free double layer.

Figure 3.11 represents the source end wall potential (floating boundary condition) corresponding to the potential drops shown in figure 3.10; this shows that the formation of the double layer is accompanied by a significant charging of the source wall.

The plasma potential obtained for identical parameters are shown in figure 3.12. The source end wall is floating in one case (dashed line), while it is grounded in the other case (solid line). In both cases the spatial potential profile and the double-layer potential drop are very similar. However, the sheath

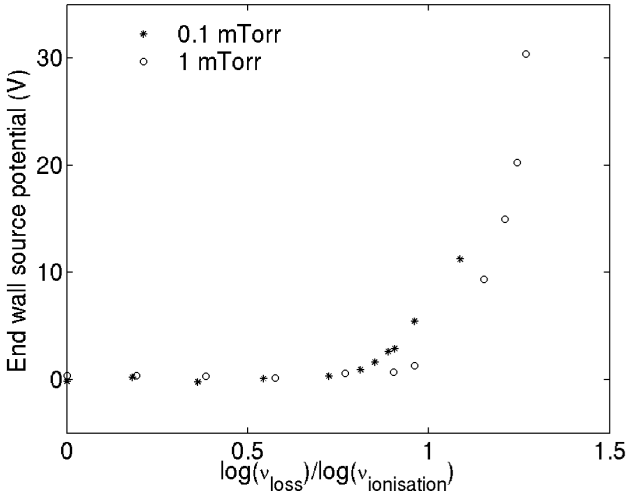

Figure 3.11: Source wall potential as a function of loss frequency.

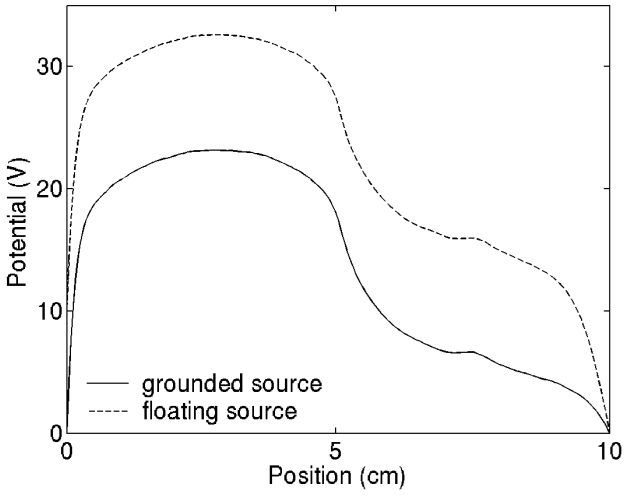

Figure 3.12: Spatial plasma potential profiles. The solid and dashed lines represent the grounded and floating source end wall, respectively.

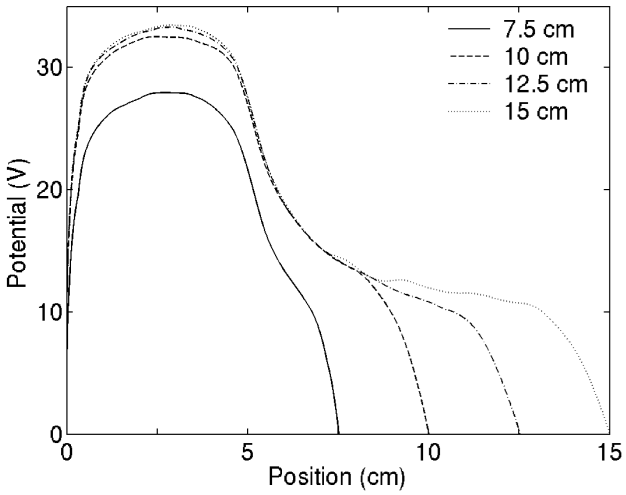

Figure 3.13: Plasma potential profiles for various right wall positions, ranging from 7.5 to 15 cm.

on the right boundary is very low when both walls are grounded (solid line), indicating that a net electron current is flowing to the right boundary; for the present conditions, the net current flowing is 0.21 A/m^2. Naturally, when the left boundary floats, no current flows through the system and the double layer is current free.

Let us suppose for the moment that the electrons are in Bolzmann equilibrium with a uniform electron temperature T_e (discussed in Chapter 4). Also, it is assumed that the ions enter the left wall sheath with the sound speed c_s and the right wall sheath with a velocity v_i that may be greater than c_s because of possible acceleration through the potential drop of the double layer (Chapter 4). A simple flux balance (similar to the calculation above) shows that

$$\frac{e\Phi_w}{k_B T_e} \sim \ln\left(\alpha \frac{c_s}{v_i}\right) \leq \frac{e\Phi_{\mathrm{DL}}}{k_B T_e}, \tag{3.22}$$

where α is the upstream to downstream density ratio and Φ_w the left wall potential. If the right wall is far enough from the double layer (a few ion mean free paths), we have $v_i = c_s$, hence equation 3.22 shows that the left wall charges up to a potential corresponding to the double-layer potential drop.

Figure 3.13 shows the plasma potential profiles for various right wall positions, ranging from 7.5 to 15 cm (from 2.5 cm to 10 cm from the double layer). The position of the double layer is not affected by the position of the right grounded wall. The broken lines show that, if the right wall is a few ion mean free paths away from the double layer, the precise position of the wall has little influence on the potential profile; the wall was even moved 50 cm away from the double layer, and the plasma potential, as well as the potential drop did not present any significant differences. By extrapolation, it can be supposed that the right wall can be moved away from the current-free double layer indefinitely without changing its properties.

On the other hand, if the the right wall is less than about an ion mean free path away from the double layer (as for the 7.5 cm case), then the average velocity v_i of the ions entering the sheath is greater than the sound speed c_s, as they are accelerated by the potential drop of the double layer (Chapter 4). As a consequence of the current-free nature of the plasma, and as shown by equation 3.22, having $v_i > c_s$ produces a decrease of the left wall potential Φ_w, hence a decrease of the whole potential profile; this is shown by the solid line in figure 3.13, where the whole plasma potential profile is shifted down by a few volts, with respect to the other profiles.

3.5 Thoughts on possible important parameters in the formation of the current-free double layer

The original aims of the simulation were i) to gain insight in the fundamental mechanisms underlying the formation of the current-free double layer observed by Charles and Boswell (2003) and ii) to investigate the particle transport, and especially the formation of an ion beam, in a current-free double-layer plasma. Hence, the primary concern of the present work was the spontaneous formation of a current-free double layer as a result of a non-trivial combination of phenomena, resulting in a non-linear behavior, rather than the formation of a double layer being more or less the direct consequence of what was "put" in the simulation, as was done when using the artificial particle loss process. In the following, attempts to spontaneously form current-free double layers, thoughts on possible important parameters and hints for future investigation are presented.

3.5.1 Sudden geometric expansion

In cylindrical systems, in the absence of confining magnetic field, radial particle losses are a decreasing function of the radius; hence, ignoring the effect of the magnetic field in the double-layer experiment described by Charles and Boswell (2003), because the source radius is smaller than the diffusion chamber radius, particle radial losses may be larger in the source than in the diffusion chamber. As it was originally shown by Andrews and Allen (1971), this kind of systems, i.e. a sudden geometric expansion, is propitious to the formation of double layers. Following up with this idea, Lieberman and Charles (2006) have developed a theory for the formation of the current-free double layer. In short, the authors obtained conditions to embed a double layer in a quasi-neutral and current-free plasma, using *five* groups of charged particles. The first four groups of particles are thermal and accelerated electrons and ions. The accelerated ions are mono-energetic while the accelerated electrons are "beam-like" and formed downstream from a "nearly" half-Maxwellian electron distribution. The fifth group of particles is the counter-streaming group of electrons, formed by the reflection on the sheath at the insulated wall of the "beam-like" electrons. The fifth group of particles ensures the current-free nature of the double layer. Finally the particle balance upstream of the double layer is found to determine

the double-layer potential drop. In this paper, the authors show that one of the *raisons d'être* of the double layer is to accelerate the downstream electrons towards the source, in order to "boost" the upstream ionization and balance the important losses of particles to the walls.

It would be interesting to validate the theory by using a one-dimensional particle-in-cell simulation including a particle loss process accounting for the radial losses in the experiment. The particle loss process would be very different to that previously described: i) the loss process should be energy-dependent, as the electrons with a kinetic energy greater than the local plasma potential only may escape to the walls. ii) Also, the loss frequency should be a decreasing function of the local chamber radius, i.e. the loss frequency should be larger in the source than in the diffusion chamber. An estimation of the loss frequency corresponding to radial losses is derived in Chapter 5.

In such a model, the static magnetic field would not be taken into account. However, Charles and Boswell (2003) have shown that the formation of the current-free double layer was only possible for sufficiently important diverging magnetic field, it is not clear why this is the case. In other words, the role played by the magnetic field in the formation of the current-free double layer is not yet understood. For example, although the theory for the formation of current-free double layers, developed by Lieberman and Charles (2006), is in very good agreement with the previous current-free double-layer experiment results, the model does not show any requirement of a static diverging magnetic field. Actually, it even seems that the presence of a magnetic field goes against their theory as it may reduce significantly the radial particle losses in the source. Nevertheless, it may well be that the magnetic is "only" required to allow the formation of the five groups of particles.

3.5.2 Possible significant role of the magnetic force

In Charles and Boswell's experiment, the magnetic field decays from 120 G in the source to 20 G over ∼15 cm, hence it can be expected that the magnetic force plays a significant role in the formation of the double layer. To verify this with the PIC simulation, most of the physical parameters have to be scaled down to keep the simulations tractable. The characteristic length of decay of the magnetic field should also be scaled down accordingly and has to be much sharper in the simulation than in reality. Physically the sharpness of the magnetic field decay out of the solenoid is controlled by the radius of the solenoid; the sharpness increases with a decrease of the solenoid radius.

Scaling the magnetic field is therefore not an issue, however, its strength and sharpness in the simulation should be compatible with a good conservation of the magnetic moment for the electrons, as in the experiment; the characteristic length of decay has to be large (10 times larger) compared to the electron gyro-radius. A more quantitative criterion can be given

$$\left(\frac{1}{\omega_{ce}}\frac{\partial \omega_{ce}}{\partial x}\right)\left(v_e\frac{2\pi}{\omega_{ce}}\right) \ll 1, \tag{3.23}$$

where the first term of the left-hand side is the fractional change in the cyclotron

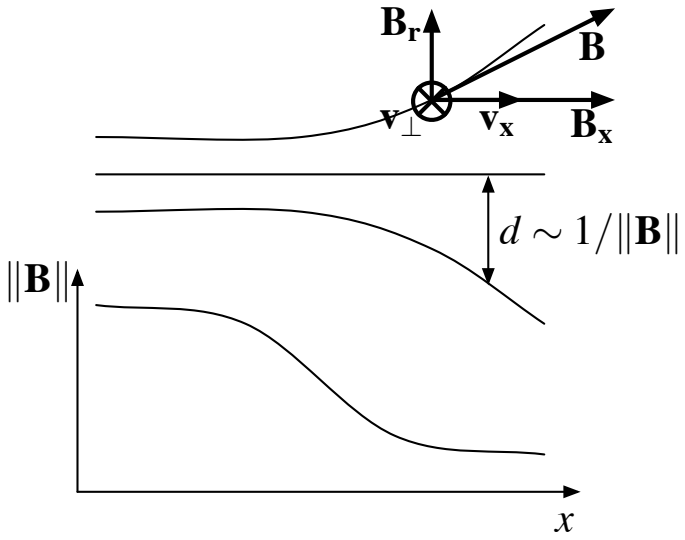

Figure 3.14: Cartoon of the expanding magnetic field lines and corresponding magnitude.

frequency ω_{ce} (or in the magnetic field B) when the electron move a distance ∂x, and the second term is the distance moved along x in the time of a gyro-motion, where v_e is a characteristic velocity of the electrons.

Because the simulation is 1D the gyro-motion is of course not resolved and the motion of the guiding center alone is calculated. The following algorithm ensures conservation of energy but not conservation of magnetic moment. We tried to investigate a more sophisticated model where both magnetic moment and energy where conserved, but had insufficient time and this should be investigated further in future. Nevertheless, it should be kept in mind that the real goal here is to estimate the possible effects of the magnetic force converting perpendicular energy into parallel energy in the direction of the magnetic expansion.

Let us consider a diverging magnetic field $\boldsymbol{B}$ symmetric about the x axis and whose magnitude decreases with x, as shown in figure 3.14. In reality, because of the conservation of the magnetic moment, electrons receive a net force $\boldsymbol{F}_{\parallel}$ accelerating them towards the direction of expansion

$$\boldsymbol{F}_{\parallel} = -\frac{1}{2}\frac{mv_{\perp}^2}{B}\frac{\partial B_x}{\partial x}\,\boldsymbol{e_x}; \tag{3.24}$$

simultaneously a force $\boldsymbol{F}_{\perp}$ ensures that the gain (resp. loss) in parallel energy is accompanied with a loss (resp. gain) of perpendicular energy (see Chen 1984, p. 30, for example). The ions are taken non-magnetized, their gyro-radius being much larger than the characteristic length of the present system. Because the PIC simulation is one dimensional, electrons do not have a cyclotron rotation movement and it is simply considered that $v_{\perp} = \sqrt{v_y^2 + v_z^2}$. The on-axis magnetic expansion is to be simulated; hence, $\|\boldsymbol{B_x}\|$ can be approximated by $\|\boldsymbol{B}\|$ in 3.24. All the electrons in the simulation "feel" the force $\boldsymbol{F}_{\parallel}$, accelerating them in the direction of expansion, conservation of kinetic energy being

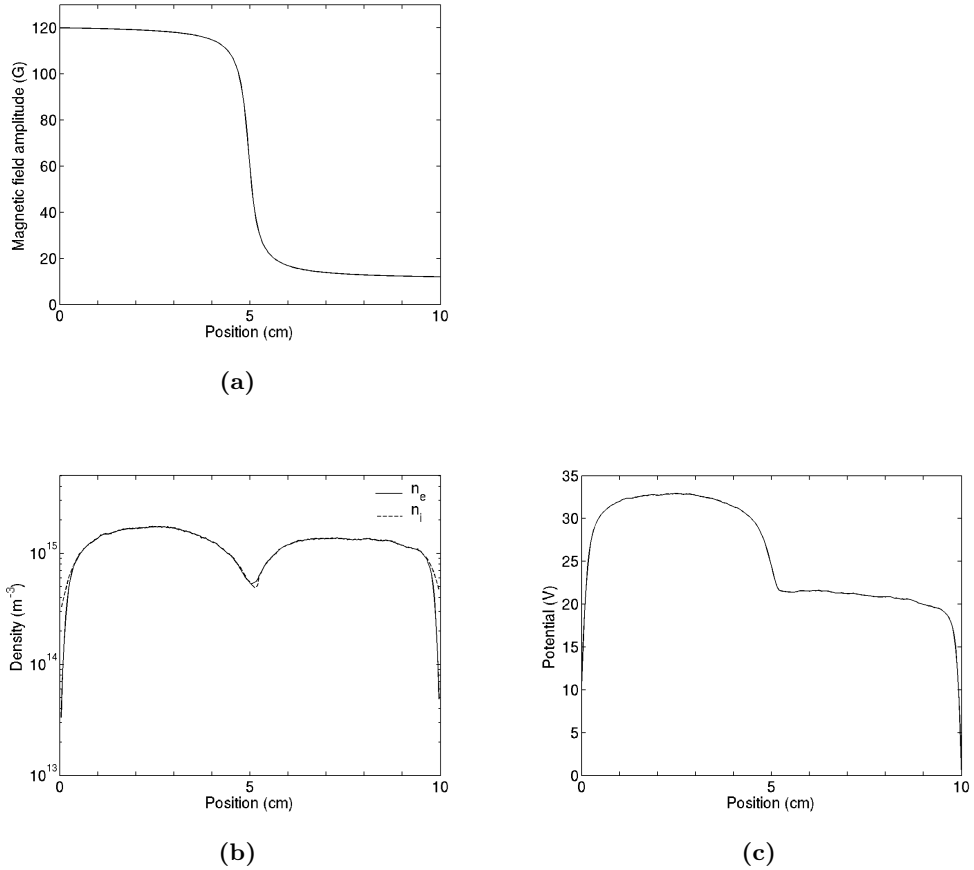

Figure 3.15: (a) Model of the magnetic field magnitude, (b) plasma density and (c) plasma potential with a PIC simulation including a simple model of conservation of the magnetic moment.

ensured "manually" by decreasing (resp. increasing) the perpendicular energy accordingly when moving in the direction of expansion (resp. contraction).

Figures 3.15(b) and 3.15(c) show the density and potential profiles obtained with the magnetic field magnitude profile shown in figure 3.15(a). A significant drop is observed in both the densities and the potential at the position of the magnetic field drop. Both the density and the potential profile are very similar to that observed by Charles and Boswell (2003) and this approach seems to be very promising. However, this should not be mis-interpreted and one should not immediately conclude that the magnetic force is responsible for the current-free double layer in the experiment. i) First, the expansion itself of the plasma, due to the diverging magnetic field was not included in the model above. ii) The present model is rather simple and although it ensures conservation of energy, for the reasons mentioned earlier on, the adiabaticity is not conserved (a time resolution of the magnetic moment μ shows that it is not constant). iii) Also, the criterion proposed before (equation 3.23) and for which adiabaticity would be conserved, is hardly satisfied. iv) Finally, in Chapter 4, the possible

loss of adiabaticity when electrons of the experimental device hit the walls of the diffusion chamber and the resulting magnetically-trapped population of electrons are also discussed. Unfortunately, this was not considered until recently and is not taken into account in the present model and investigated in depth in the present thesis; this shall be investigated further in future.

Nevertheless, although the model is rather simple and fails to account for various phenomena, a current-free double layer is formed. This approach is therefore extremely promising and it would be worthwhile investigating further the possible effects of the magnetic force on the current-free double layer observed by Charles and Boswell (2003).

It seems that until quite recently the importance of the magnetic field in the formation of the current-free double layer was under-estimated. There has been considerable interest recently in investigating the possible effects of the magnetic force (Hagelaar 2005a, Lieberman 2006b, Chen 2006). Also, a very recent paper by Fruchtman (2006) has shown that the magnetic-field force increases the plasma thrust along the flow in the case of a current-free double layer.

3.6 Conclusion

An rf electric field perpendicular to the spatial dimension was included in the left half (source) of a PIC/MCC simulation to model inductive excitation of the plasma without solving electromagnetic field equations. An advantage of this scheme is that it avoids rf excursions of the plasma potential, characteristic of capacitive coupling.

In addition to the localized inductive heating mechanism, an energy-independent loss process was introduced in the right half (diffusion chamber) of the simulation. Although the loss process does not present any obvious physical justification and does not explain the current-free double layer observed by Charles and Boswell (2003), it produces an axial decrease in the plasma density and an associated potential drop with the properties of a current-free double layer. The loss process was a way of creating and investigating a current-free double layer. Also, one of the primary concerns was to investigate the particle transport, and especially the formation of an ion beam in a current-free plasma sustaining a double-layer; this is presented in Chapter 4

Finally, by using a simple algorithm converting the perpendicular energy into parallel energy in the direction of the magnetic expansion, it was shown that the magnetic force may play a significant role in the formation of the current-free double layer. However, a recent theory on the formation of the current-free double layer, in good agreement with the experiment has also shown that, in principle, a static magnetic field was not required for the formation of the double layer. The role of the geometric and magnetic expansion should be investigated further by numerical simulation in future.

Chapter 4

Particle transport in the current-free double layer

One of the primary motivations of the current-free double-layer particle-in-cell simulation, where both electrons and ions are treated as particles, was to investigate the particle transport in such a plasma and to compare it with experimental data. In particular, the formation of an electron and an ion beam, resulting from charged particles accelerated through the potential drop of the double layer were of particular relevance. In the present chapter, both electron and ion transport are investigated.

4.1 Depletion of the electron energy distribution function[1]

4.1.1 Background

The form of the escaping electron energy distribution function (eedf) has always been the subject of considerable discussion, as has the Maxwellianization of the electrons trapped between opposing sheaths. In capacitively-coupled plasmas, two-temperature electron distribution functions are not rare and fall into two categories. i) The first type, generally observed at some tens of mTorr, has a concave shape, presents a more energetic tail than the bulk Maxwellian distribution and can be approximated as a sum of two Maxwellian distributions. Such bi-Maxwellian distributions are thought to be the result of a combination of the Ramsauer minimum in the electron-neutral elastic collision cross-section and the distribution function non-locality, as was shown experimentally by Godyak and Piejak (1990), Godyak et al. (1992) and confirmed by subsequent experiments and particle-in-cell simulations by Turner et al. (1993). ii) The second type has a convex shape and is observed at higher pressure, i.e. some hundreds of mTorr. In this case, the distribution function presents a drop or break in the slope, defining a sudden divergence away from the bulk Maxwellian distribution. The presence of this rapid drop for electron energies higher than a certain

[1] This section, in slightly altered form, has been published in Meige and Boswell (2006).

threshold is generally attributed to inelastic collisions (Godyak and Piejak 1993, Godyak et al. 1995).

In inductively-coupled plasmas (ICP), Godyak and Kolobov (1998) measured even more complex distributions, having a three-temperature structure. Once again, the depletion at high energy, compared to Maxwellian, is in general attributed to inelastic collisions and, at lower pressure, to the escape of the fastest electrons, as it was shown by Granovski (1971) and Godyak et al. (2002).

In low-pressure discharges, below a few mTorr, collisions and especially inelastic collisions are rare and cannot alone explain the high-energy break in the eedf. Biondi (1954) already showed over 50 years ago that the loss to the walls might be responsible for the depleted tail of the distribution. He had identified this phenomenon, that he named "diffusive cooling", to be the main electron cooling mechanism in the afterglow of his "ionised gas". The effect of diffusive cooling has been previously studied, both theoretically and experimentally, in swarm physics (Robson 2000, Parker 1965, Rhymes and Crompton 1975) and plasma physics by a number of models (Ashida et al. 1995 1996, Kolobov et al. 1997). In these studies, the loss of electrons to the walls was shown to be the main energy loss mechanism, but the assumption of Maxwellian distributions was made.

A more accurate kinetic approach was recently performed by Arslanbekov et al. (2001) and Arslanbekov and Kudryavtsev (1998) where they showed that two main mechanisms exist for electron and energy loss: the first they called "cutoff effect" and occurs when the trapped electrons become free electrons as the plasma potential collapses during the discharge afterglow. The second effect occurs when the trapped electrons gain energy through electron-electron collisions and are eventually pushed to energies higher than the plasma potential, thus becoming free electrons and escaping to the walls. Unlike the cutoff effect that occurs during the afterglow of a discharge, the second effect occurs even during the steady state. Kortshagen, Maresca and co-workers have experimentally shown some of Arslanbekovs results (Kortshagen et al. 2002, Maresca et al. 2002). However, these experiments were only conducted in the afterglow regime of inductively-coupled plasmas, i.e. in transitory regimes.

In this section, the experimental measurements performed by Granovski (1971) and Godyak et al. (2002), showing that at low pressure, the high-energy depletion of the eedf is due to the fastest electrons escaping to the walls, are confirmed by the use of the particle-in-cell simulation. It is shown that in steady-state plasmas, when the electron mean free path, and more precisely the energy relaxation length is of the order of or greater than the system length, electrons trapped in the well formed by the two sheaths at the boundaries have a Maxwellian distribution, while the high energy tail of the eedf is distinctly depleted. Clear evidence that the depletion at high energy of the eedf is essentially due to the loss of the most energetic electrons to the walls is presented. The break energy, for which the depletion of the Maxwellian starts, occurs at the local plasma potential. That this break point tracks the plasma potential through the length of the simulation is due to the non-locality of the electron distribution function.

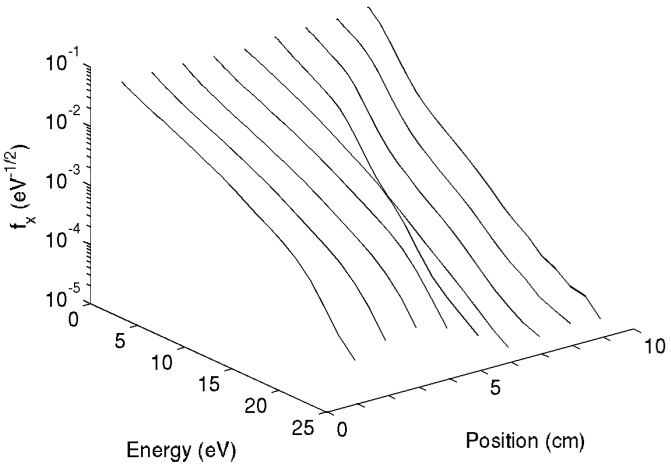

Figure 4.1: x-velocity component of the evdf f_x represented in log scale, as a function of the electron energy and at different positions in a double-layer plasma. The distributions are Maxwellian for the low-energy group of electrons and present a depleted tail at higher energy.

In the following, eedfs are given in terms of normalized electron velocity distribution functions (evdfs), resolved for the three different velocity components. They are measured along the abscissa with a spatial average over a distance of 0.4 mm and a temporal average over 100 rf cycles. The ordinate is log scale and a function of the electron energy, so that a Maxwellian distribution yields a straight line. To recapitulate, the simulated system has a finite size of 10 cm along the x direction, while it is infinite along the two other y and z directions, which allows the actual effect of the walls on the eedfs to be determinated.

4.1.2 Double-layer plasma

The eedf the double layer obtained with the parameters given in table 3.2 and shown in figure 3.7 are first investigated. As the bulk plasma itself is supporting the 12 V double layer, this system presents an ideal opportunity to study the eedf for different local plasma potentials.

Figure 4.1 shows the evdf as a function of the electron energy at different positions in the plasma and it is quite clear that each of these distributions is Maxwellian at low energy, but presents a depleted tail at higher energy. The plasma potential profile along the system is shown as a solid line in figure 4.2 and about half way across the system, i.e. at 5 cm where the loss process begins, the double layer can be seen at the interface between the source and the diffusion chamber. Of particular relevance here, the break energy $\mathcal{E}^*$ depends on the position in the plasma and tracks the local plasma potential. This is a direct consequence of the non-locality of the electron distribution, where the eedf is not in equilibrium with the local electric field (Bernstein and Holstein 1954, Tsendin 1974, Kolobov and Godyak 1995).

To make this point very clear, the dotted and dashed lines in figure 4.2

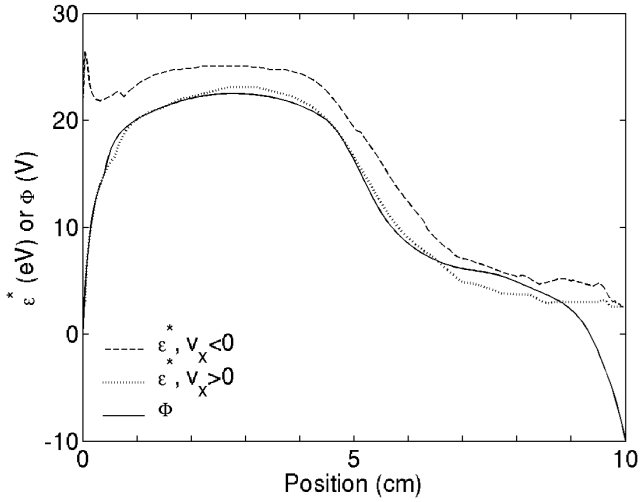

Figure 4.2: Energy $\mathcal{E}^*$ of the evdf break for positive (dotted line) and negative (dashed line) velocities as a function of position. The energy of the break tracks the plasma potential Φ of the double-layer plasma (solid line).

show the evdf break energy, measured in eV, for both positive (right directed) and negative (left directed) electron velocities, respectively. For both cases, the energy corresponding to the break follows the local plasma potential. The evdf break energy for negative velocities is found to occur at energies slightly higher than for positive velocities, presumably due to the asymmetry of the plasma potential profile and the potential difference between the left and right walls. When both walls are grounded a much less pronounced difference between the positive and negative velocities is observed.

4.1.3 Inductively-coupled plasma

To check that the loss process that creates the double layer does not introduce non-physical features in the eedf, a simple inductively-coupled plasma (ICP) is now investigated. The same parameters as in the previous section are used with the "inductive" heating mechanism on the left half of the system but the particle loss process on the right half was deactivated. Figure 4.3 shows evdfs across the plasma which are Maxwellian distributions with a depleted tail. Once again, as shown by figure 4.4, the evdf break energy $\mathcal{E}^*$ tracks the plasma potential, but unlike the double-layer case, the break energy for the positive and negative velocities is the same. This tends to confirm that the difference between positive and negative velocities in the double-layer case was due to the highly non-symmetrical nature of the system.

Hence, for both the double-layer plasma and the ICP, the presence of a sudden break in the eedf for high-energy electrons was shown and due to the non-locality of the eedf, the energy of the break tracks the local plasma potential. As stated previously, at higher pressures, the break has been attributed to atomic processes arising from inelastic collisions, and at lower pressure to the

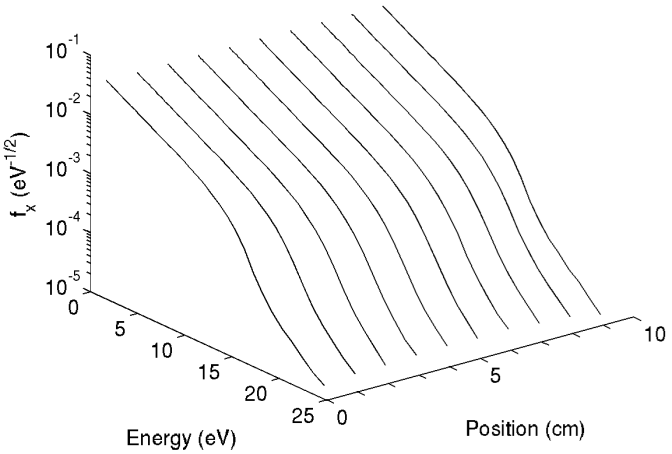

Figure 4.3: x-velocity component of the evdf f_x represented in log scale, as a function of the electron energy and at different positions in a simple inductively-coupled plasma. The distributions are Maxwellian for the low-energy group of electrons and present a depleted tail at higher energy.

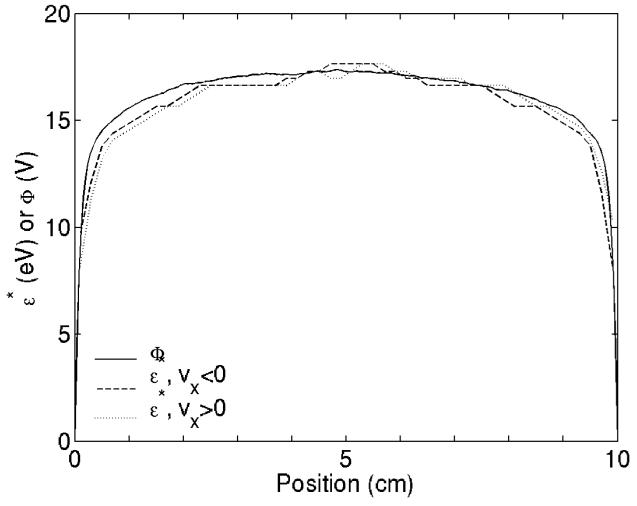

Figure 4.4: Energy $\mathcal{E}^*$ of the evdf break for positive (dotted line) and negative (dashed line) velocities as a function of position. The energy of the break tracks the plasma potential Φ of the simple inductively-coupled plasma (solid line).

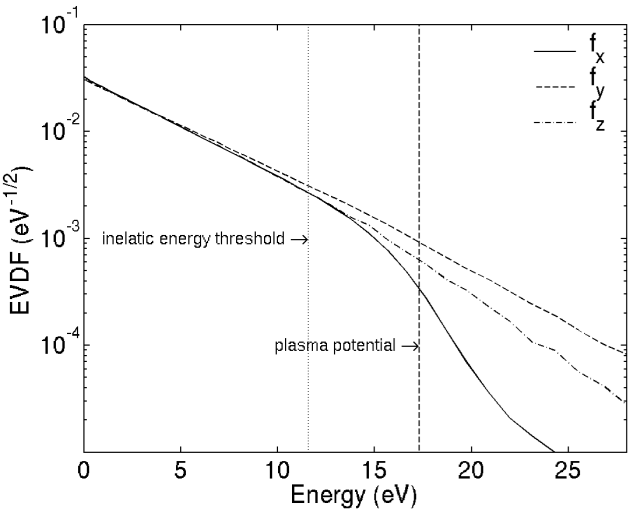

Figure 4.5: Three velocity components of the evdf measured in the bulk of the ICP and plotted as a function of electron energy. The distribution is depleted, compared to Maxwellian distribution, for the spatially limited velocity direction (f_x, solid line). On the other hand, evdfs corresponding to the velocity direction for which the plasma is not bounded are Maxwellian (f_y and f_z, broken lines). The vertical dotted and dashed lines show the inelastic energy threshold and the local plasma potential, respectively.

high-energy electrons lost to the walls.

Figure 4.5 shows the evdf in the bulk of the ICP for the three different velocity components and the spatially limited velocity direction of the evdf f_x (solid line) alone displays a break at high electron energies. The evdf f_y and f_z (broken lines) corresponding to the perpendicular directions, i.e. where the plasma is not bounded, are almost Maxwellian, except for a very slight inflexion, which is presumably due to rare inelastic collisions. If the significant break observed in f_x were also due to inelastic collisions, this would be clearly seen in the f_y and f_z components. In other words the substantial break observed in evdf of the spatially limited direction appears to be mostly due to the loss of high-energy electrons to the walls.

As previously stated, the inductive heating mechanism acts in the perpendicular direction of the simulation (Chapter 3) and, at low pressure, the energy relaxation rate is much longer than the momentum relaxation rate. Consequently, electrons suddenly acquiring enough momentum along x to be able to reach the walls after a single elastic collision have a high probability of actually escaping without undergoing another collision, and hence without being able to repopulate the tail of the distribution function. These electrons lost to the walls, i.e. the most energetic ones, depopulate the tail of the distribution.

For completeness, the numerical experiment was repeated for pressures between 0.1 to 100 mTorr. As expected from many experiments and glow discharge theory, the bulk electron temperature decreases when the pressure increases. Additionally, the evdf break moves to lower energies, corresponding to the inelastic collision energy threshold, when increasing pressure. At low

pressure, i.e. below a few mTorr, the plasma potential defines the limit of the Maxwellianisation of the electrons, while at higher pressure the electron distribution appears to be governed by the shorter electron mean free path of the various elastic and inelastic processes.

4.1.4 Discussion

The fact that the electron energy distribution functions presented above for both the double-layer plasmas and the ICP did not have any low-energy electron population was not considered until now. This appears to be in contradiction with the many experiments previously reported (Godyak et al. 2002).

At higher density, electron-electron Coulomb collisions are no longer negligible and would Maxwellianize the low-energy part of the distribution, and could explain the absence of low-energy population in the results presented above. However, under the conditions that were considered (low density), electron-electron Coulomb collisions are negligible and were not included in the model. To explain the absence of a low-energy peak in the distribution, we shall go back to its origin in real experimental systems. Low-energy electrons are trapped by the ambipolar electric field in the plasma bulk, thus they are prevented from participating in the heating process taking place in the skin layer. As stated previously, in the simulation the heating mechanism is located in the the whole "source", i.e. in the whole left half of the simulation. Therefore, unlike in real inductively-coupled plasma, there are no trapped electrons and all the electrons participate in the heating mechanism, which presumably explains the absence of low-energy population.

In addition, in the previous simulations, after an ionization event, the energy between the scattered and the created electron was chosen to be shared with a probability not depending on the energy of the incident electron, hence favoring the creation of relatively energetic electrons, which could presumably explain the absence of a cold population even when the width of the heating region was reduced to allow the existence of a non-heated trapped population of electrons.

To confirm this assumption, simulations where the heating region was as small as 0.5 cm, where a significant fraction of the electrons do not participate in the heating mechanism were run with a different energy-sharing algorithm. Rather than equally sharing the energy between the scattered electron and the newly created electron after an ionization event, an energy-dependent mechanism, where the energy of the newly created electron is forced to be less than 1 eV was implemented. In this case a low-energy population of electrons was observed. However, this population of low-energy electrons is far from being as important as that experimentally measured and reported by Godyak et al. (2002), for example. It may well be that electrons in the elastic energy range suffer from numerical heating or that the simulations are simply not completely steady state, although run for thousands of rf cycles. This issue is currently being investigated by Legradic (2006) both experimentally and by computer simulation.

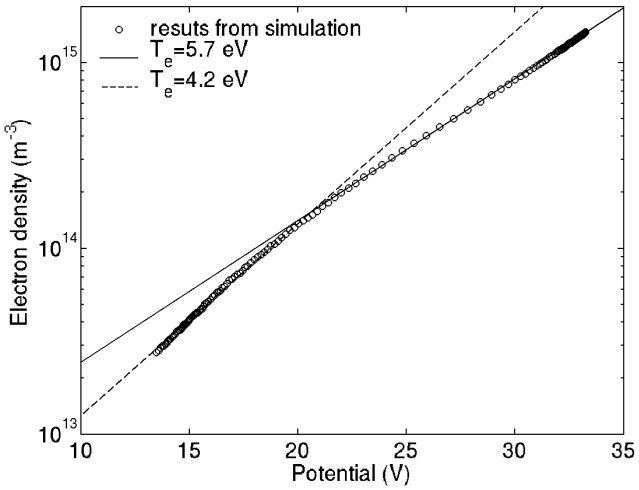

Figure 4.6: Electron density in log scale as a function of the plasma potential, so that Boltzmann electrons yield a straight line. When the double layer is formed, two distinct populations of electrons exist.

4.2 A Bolzmann equilibrium "by part"

In the previous section, it was shown that electrons trapped by the ambipolar electric field have a Maxwellian distribution, while those whose energy is greater than the plasma potential have a depleted distribution. Also, no electron beam was observed on the high-potential side of the double layer. The presence of an electron beam in the simulation and especially in the experiment is of particular relevance as it would validate the theory recently developed by Lieberman and Charles (2006) on the formation of the current-free double layer, as it requires an electron beam. That such an electron beam was not observed in the simulation is not too surprising as the electron density is much smaller downstream than upstream; thus even if an electron beam was formed, it would result from electrons accelerated from the downstream side, the relative density of the beam (upstream) would be extremely small.

Figure 4.6 shows the electron density as a function of the plasma potential, so that Boltzmann electrons yield a straight line, for the typical double layer obtained for the parameters given in table 3.2 (Chapter 3) and a loss frequency of 10^6 s^{-1}. Two distinct populations of Boltzmann electrons with distinct "Boltzmann temperatures"[2] are noticeable. A population of hot electrons is observed on the high-potential side, with a temperature of 5.7 eV and a colder population downstream of the potential drop, with a temperature of 4.2 eV. That the electrons are in Boltzmann equilibrium, even "by part", tends to confirm that no electron beam exists in the simulation.

A number of double-layer experiments have reported two electron temperatures; for example Chan and Hershkowitz (1983, and references therein) have

[2]What is meant by "Boltzmann temperature" is the inverse of the slope of the electron density in log scale $\ln(n_e)$ plotted as a function of plasma potential Φ.

measured a high temperature on the high-potential side of the double layer and have investigated this peculiar behavior into detail. They have shown that the thermalization of the "bump-on-tail" distribution, due to the electrons accelerated from the downstream to the upstream side, was not responsible for the two distinct electron temperatures, and believes that turbulence in the double-layer region, cold-electron convection and thermoelectric effects may play a significant role in the temperature non-uniformity.

Charles and Boswell (2003) have also measured two distinct electron temperatures when the current-free double layer was formed. Although this is still not fully understood, it is presumably a combination of the electrons trapped by the electrostatic potential of the double layer and a loss of the adiabaticity (Lieberman 2006b, private communication). In short, there is a first population of electrons, trapped upstream of the double layer by the electrostatic potential. These electrostatically trapped electrons "see" the heating mechanism from the source constantly, and are permanently heated. Some of these electrons may escape the potential well and be accelerated towards the walls of the diffusion chamber by the magnetic force converting their perpendicular energy into parallel energy (conservation of the magnetic moment). At some point these accelerated electrons reach the sheath at wall of the diffusion chamber and those which are not lost to the wall suffer from specular reflections, hence loosing their adiabaticity. Thus, instead of returning to the source following the same way they came, these electrons are then trapped in the diffusion chamber by the magnetic mirror, suffering from elastic collisions; the loss of energy in collisions is not balanced as these magnetically trapped electrons never "see" the heating mechanism. Eventually these electrons enter a loss cone and are able to return to the source etc. In summary, it seems that an electrostatically-confined hot electron population exist in the source and another magnetically-confined colder electron population in the diffusion chamber.

In the present simulation, the two distinct electron temperatures observed may be explained in a different way. They may be a consequence of a combination of both the depletion and the non-locality of the x-directed electron energy distribution function (Section 4.1). Upstream of the double layer, the depletion of the distribution function starts for energies higher than ~ 20 eV, while it starts at ~ 8 eV downstream of the double layer; hence the effective temperature [3] of the distribution (figure 4.7) is higher upstream than downstream of the double layer, in good qualitative agreement with the "Boltzmann temperature" given above. However, the "Boltzmann temperature" and the "effective temperature" defined above are not equal; the qualitative trends are the same, but the numbers are slightly different. This is presumably because of the anisotropy of the eedf; for example, is the temperature derived from the Boltzmann relation related to that derived from the x-directed eedf, or from the full three-dimensional eedf (the 3D effective temperature is actually rather uniform in the whole system).

[3] What is meant by "effective temperature" is the temperature that would have a Maxwellian distribution with the same mean energy as the present non-Maxwellian distribution.

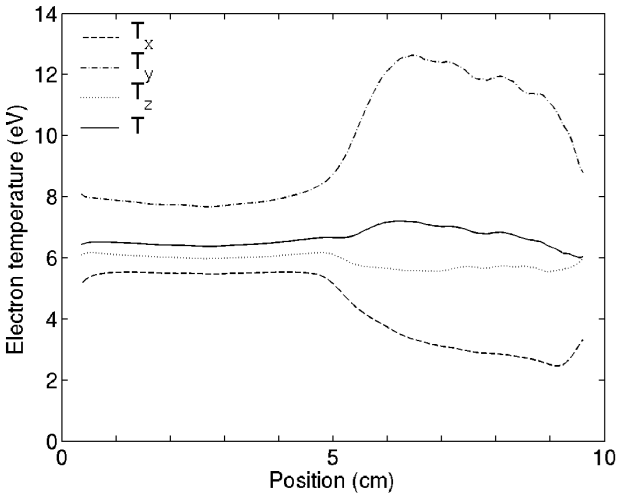

Figure 4.7: x, y and z-directed effective electron temperature spatial profiles.

In summary, the two distinct temperatures measured by Charles and Boswell (2003) in the current-free double layer seem to have a different origin from that observed in the present simulated current-free double layer. It seems unlikely that the explanation given for the simulation could also be valid in the experiment as the experiment chamber is much longer than in the simulation, resulting presumably in a much less depleted eedf. However, the existence of two distinct Boltzmann populations seems to be a good sign for both the experiment and the simulation as it was shown by Verheest and Hellberg (1997) that double layer cannot be supported by only one Boltzmann population irrespective of the number of cold fluid species (ions).

It would be interesting to try and model with the PIC simulation the loss of adiabaticity evoked above, in a similar way as presented in Chaper 3 as it may trigger the spontaneous formation of a current-free double layer; however, the possible significant role of this phenomenon was not proposed until recently and cannot be investigated in depth in the present thesis.

4.3 The electrons seem to be hotter where they are not heated

As mentioned in the previous section, according to their "Boltzmann temperature", the electrons are more energetic on the high-potential side of the double layer, where they are heated. The solid line in figure 4.7 shows that the 3D effective temperature profile is rather uniform and does not seem to decrease much on the low-potential side; on the contrary, before the net decrease of the effective electron temperature on the downstream side, a slight increase just after the double layer is first observed. This is due to a combination of two effects being somewhat in competition: the respective increase and decrease of the x and y-directed electron temperatures downstream of the double layer. i)

The decrease of the x-directed electron effective temperature T_x (dashed line) was already explained in the previous section; this is due to a combination of the depletion and the non-locality of the x-directed eedf. ii) The increase of the y-directed electron temperature T_y (dotted-dashed line) was also explained earlier; recall from Chapter 2 that electrons with a low parallel energy are electrostatically trapped in the source, while the fastest electrons are not and can be affected by some sort of stochastic heating in the non-uniform perpendicular rf electric field. Under the present conditions of pressure, the stochastic heating dominates over the classical ohmic heating; hence, electrons that are stochastically heated are more anisotropic than those that are not. These "more anisotropic" energetic electrons are present on both sides of the system. This is clearly visible on the low-potential side of the system, where the y-directed electron mean energy $\mathcal{E}_y$ is 1 eV larger than $\mathcal{E}_x$. However, because these "more anisotropic" energetic electrons are much less numerous than the low-energy trapped electrons on the high-potential side, they are more visible in this region; $\mathcal{E}_y$ is only 0.5 eV larger than $\mathcal{E}_x$, hence giving the impression that electrons are somewhat cooler where they are heated than where they are not.

4.4 Formation of an ion beam, comparison with experiment[4]

The results obtained with the particle-in-cell simulation were consistent with the retarding electric field analyzer (RFEA) measurements performed by Charles (2004) in *Chi-Kung* that indicated a sharp discontinuity in the plasma potential and the formation of a super-sonic ion beam. However, no experimental ion phase space measurement was originally available for further comparison. A LIF (laser-induced fluorescence) measurement of the ion phase space was later performed and was in relatively good agreement with that obtained with the PIC simulation.

Figure 4.8(a) shows the ion velocity distribution in phase space when the current-free double layer is formed. The abscissa represents the position (spatial dimension of the simulation) and the ordinate represents the ion velocity. The same parameters as the "typical double layer" shown in figure 3.7 were used, the potential drop across the double layer is approximately 12 V over a thickness of less than 20 Debye lengths and it is associated with a charging of the source up to 10 V. Throughout the simulation length, a low-energy population of ions created by ionization and charge exchange collisions is observed. A high-energy population of ions is observed downstream of the double layer and constitutes an ion beam. These high-energy ions are those accelerated while traversing the potential drop of the double layer. The sound speed c_s in argon under the present conditions (T_e =5.7 eV) is ~3.7 km/s. Figure 4.8(a) shows that a pre-sheath upstream of the double layer first accelerates the ions up to the sound speed; once the ion flow becomes super-sonic, the double layer forms (the quasi-neutrality is locally violated) and the ions are then accelerated up to

[4]The results presented in this section were published in Meige et al. (2005a), Sun et al. (2005) and Keesee et al. (2005).

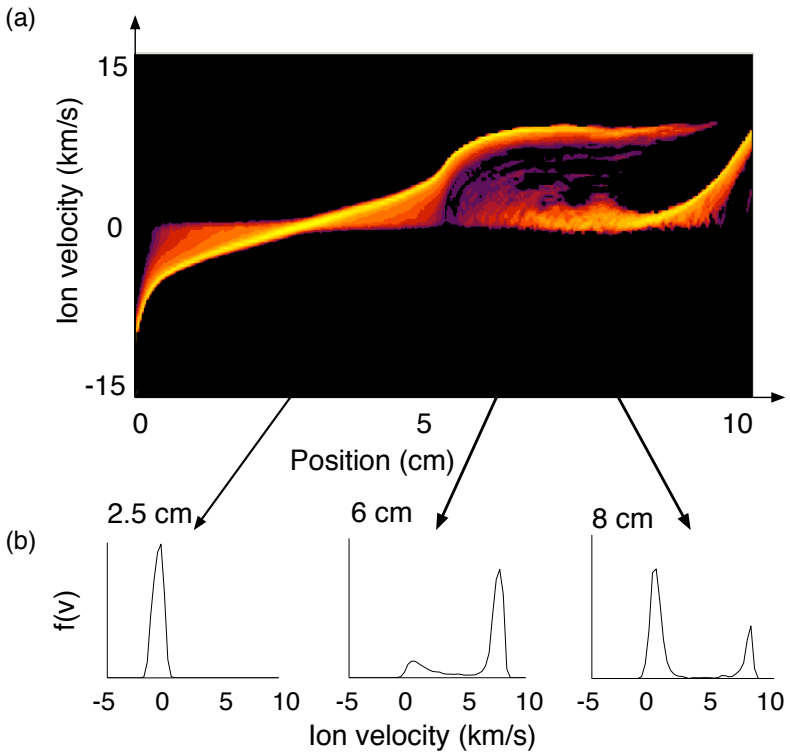

Figure 4.8: (a) Ion velocity distribution in phase space with the full PIC simulation under the conditions of the double layer; a super-sonic ion beam is observed. Increased brightness indicates increased density. (b) x-directed ion velocity distribution function $f(v)$ in arbitrary units at various positions.

twice the sound speed (the average velocity of the ion beam is 8.1 km/s) after less than 20 Debye lengths.

The acceleration of the background ion population to the floating and grounded boundaries of the simulation volume where the ions fall through the sheath is also evident at the sides of figure 4.8(a).

Figure 4.8(b) shows that the density of the ion beam decreases away from the double layer as a result of ion-neutral collisions (charge exchange and elastic collisions).

The ion argon velocity distribution function (ivdf) along the axis of *Chi-Kung* (the ion phase-space density) was nonperturbatively measured (Keesee et al. 2005) with a portable, tunable diode laser, LIF diagnostic and compared to the simulation. Figure 4.9(a) shows the log of the LIF signal versus parallel ion flow speed and axial position in *Chi-Kung* in the conditions of the double-layer formation; a strong acceleration of the ions is visible in the LIF data (from 25 to 28 cm), which is in good agreement with the RFEA measurement. Downstream of the double layer, the trapped ion population created by ionization and charge-exchange collisions as well as its acceleration through the sheath to the grounded end wall are also clearly visible. For all accessible neutral pressures in *Chi-Kung*, the ion beam is not detectable by LIF beyond the acceleration region, although the ion beam is clearly measured with the RFEA. Previous measurements by Cohen et al. (2003) indicated that such low density ion beams become undetectable within a few cm of the double layer by low-power LIF because of the metastable density decreasing exponentially in the expansion region.

For completeness and to be able to compare the ion phase space predicted by the PIC simulation with experimental data, the LIF measurements of double-layer formation were repeated in the higher-density, larger-diameter helicon source, called HELIX (Sun et al. 2005). The plasma potential profile measured with a rf-compensated, planar Langmuir probe and LIF measurements of the parallel ivdf for a neutral pressure of 1.3 mTorr are shown in figure 4.9(b) and (c). The ions accelerate through the presheath upstream of the double layer and reach a peak energy of approximately 18 eV. The ivdf is well fitted by a single Maxwellian distribution. Since the downstream plasma electron temperature is 5.0 eV, the ion beam is supersonic with a Mach number of roughly 2.0. The LIF measurements indicate that the total ion acceleration occurs over approximately 20 cm with strong ion acceleration occurring over a much narrower region, 5 cm, located at the maximum of the magnetic field strength gradient.

4.5 Conclusion

Recall from Chapter 3 that one of the primary motivations for the particle-in-cell simulation of a current-free double layer was to investigate the particle transport in such a plasma. Although, the particle loss process introduced into the PIC scheme does not present any obvious physical justification, it allowed a current-free double layer to form, hence giving us the opportunity to investigate in depth the particle transport.

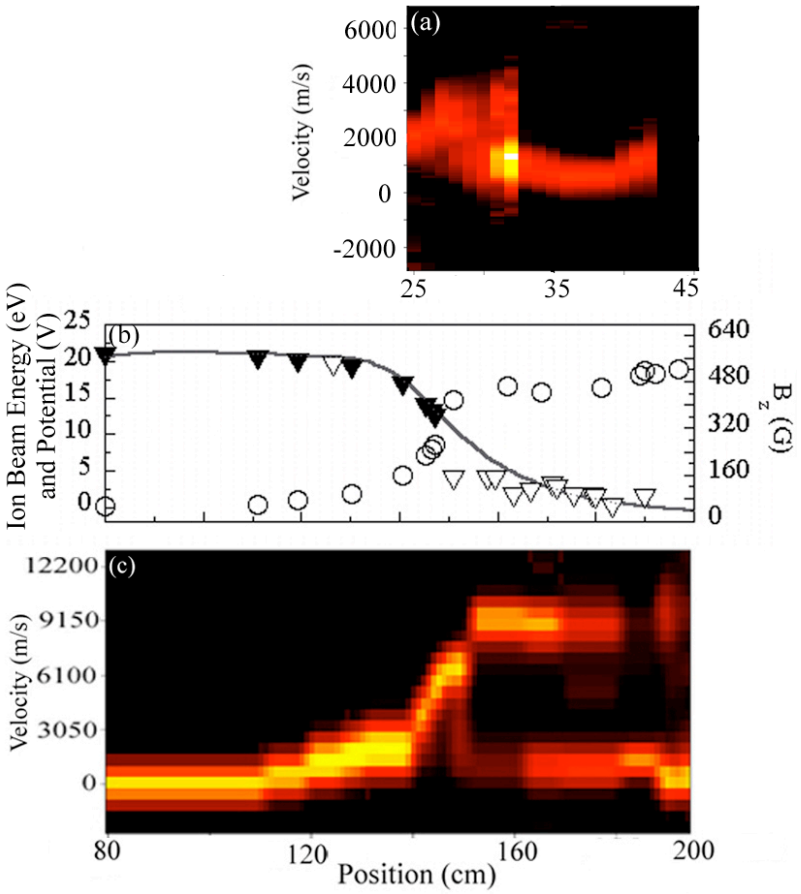

Figure 4.9: (a) Logarithm of amplitude of parallel ivdf (color bar) versus parallel velocity and axial position as measured by LIF in the *Chi-Kung* experiment. (b) double-layer potential difference (plasma potential - 9.8 V) versus axial position as measured with a rf-compensated, planar Langmuir probe in HELIX (open triangles), ion-beam energy as measured with LIF (open circles), predicted upstream potential difference based on ion-beam data (solid triangles), and axial magnetic field strength (solid line). (c) Logarithm of amplitude of parallel ivdf (color bar) versus parallel velocity and axial position in HELIX. Figure components (a), (b), and (c) have been aligned by location of the beginning of rapidly expanding magnetic field (Sun et al. 2005).

For inductively-coupled plasmas (with or without an electric double layer), it was shown that when the electron energy relaxation length is greater than the system dimension, electrons lost to the walls are the main mechanism for the high-energy depletion of the eedf. These results confirm earlier experimental results by Granovski (1971) and Godyak et al. (2002). The depletion of the eedf is of particular relevance as it has strong consequences on the electron flux to the walls. This is often neglected in a number of so-called hybrid simulations, where the electrons are assumed to have a Maxwell-Boltzmann distribution, even at low pressure, leading to a miscalculation of quantities such as the plasma potential, as demonstrated in Chapter 3.

No electron beam was observed on the high-potential side of the double layer. The presence of an electron beam in the simulation and especially in the experiment would validate the theory recently developed by Lieberman and Charles (2006) on the formation of the current-free double layer, as it requires an electron beam. That no electron beam was observed in the simulation is presumably because of the very large upstream to downstream density ratio. Although this was not checked, it may well be that an electron beam was formed in the the double-layer simulation of Section 3.5.2; this shall be investigated further in future.

Finally, the spatial structure, beam energy, character of the ion acceleration region, and ion heating in the presheath predicted with PIC simulation of the current-free double layer are all consistent with the LIF measurements. Both the simulation and the experiment have shown the formation of a super-sonic ion beam resulting from the ions accelerated through the double-layer potential drop. Because of the formation of a super-sonic ion beam, the current-free double layer has many potential applications, such as in plasma processing (Charles 2006) and plasma propulsion (Gesto 2005, Gesto et al. 2006, Charles et al. 2006) etc. For example, because the double layer is completely current free, the electron and ion fluxes across the double layer are equal, which is of great interest for space propulsion as there is no need to neutralize the ion beam providing the thrust.

Chapter 5

An improved hybrid Boltzmann–particle-in-cell simulation

5.1 Introduction

Particle-in-cell (PIC) is a purely kinetic representation of a system containing ions and electrons, considered as individual particles, which move under the influence of their own self-consistent electric field (Birdsall and Fuss 1969, Langdon and Birdsall 1970, Hockney and Eastwood 1988, Birdsall and Langdon 1985). PIC simulations use first principles (Poisson's equation and Newton's laws) only. Each particle of the simulation is actually a macro-particle which is allowed to represent a large number of real particles (on the order of 10^9 or 10^{10} particles per macro-particle) and which can move inside the simulated domain. With a small number of these macro-particles (typically between 10^4 and 10^5 for a 1D system), a realistic steady-state plasma can be obtained in a few hours on a modern desktop computer.

The time step and the cell size of full particle-in-cell simulations, where both ions and electrons are treated as particles have to resolve both the plasma frequency and the Debye length to ensure stable and accurate simulations. These extremely stiff conditions become a real issue when simulating high density plasmas as the plasma frequency is proportional to the square root of the plasma density. The higher the density of the simulated plasma is, the shorter the time step and the smaller the cells. For example, to simulate plasmas at a density of 10^{17} m^{-3}, the time step should be as small as 10^{-11} s, which is still tractable as long as one is interested in simulating phenomena reaching a steady state over a few electron time scales. However, when dealing with phenomena related to ion transport or of which time scale is large, e.g. of the order of the millisecond, full particle-in-cell simulations become cumbersome, as they would require several billions of time steps and several days of calculation.

Increasing the speed of particle-in-cell simulations is a challenging issue that has been going on for years; Kawamura et al. (2000) have written a very interesting review of the various techniques that are commonly used. As early

as the beginning of the 80's Cohen and Freis (1982) and Langdon et al. (1983) had developed the so-called implicit scheme for PIC simulations allowing the use of larger time steps than with the classical explicit scheme. More recently, the use of variable macro-particle weight was developed (Cooperberg et al. 1994, Coppa et al. 1996, Shon et al. 2001). Some techniques also involve optimization of the codes with respect to the physical architecture of the computers (Liewer and Decyk 1989, Bowers 2001) etc.

The speed of PIC simulations can also be increased by making a certain number of assumptions on the electron transport. Under isothermal and collisional conditions, the relationship between the density gradient and the plasma potential agrees well with the simplified Boltzmann equation that reads

$$n_e = n_0 \exp \frac{e\Phi}{k_B T_e}, \tag{5.1}$$

where n_e is the electron density, n_0 the electron reference density where the potential is null, Φ is the plasma potential and T_e is the electron temperature. This assumption can be implemented *a priori* and instead of solving the electron transport *self-consistently*, one can assume that the electron density is given by equation 5.1, which allows to jump over the electron plasma frequency, hence saving a significant amount of computing time and smoothing out any fluctuation in the time range less than the plasma frequency. The only constraint on the time step remaining in this case is that it should be short enough to prevent the particle ions from crossing a whole cell. Typically, for the plasmas considered above, the time steps can be as large as 10^{-7} s, which is several thousands times larger than the time step required for a full PIC under the same conditions. In section 5.2.5, a necessary condition on the time step to ensure stability and accuracy of the simulation is given. This kind of simulation is called *hybrid* simulation as the different species are not treated in the same way: electrons are treated as a fluid, described by the Boltzmann relation, while ions are treated as particles. In the following, "hybrid Boltzmann-PIC" simulations will be referred to as "classical hybrid" or simply "hybrid" simulations. However, note that various other types of "hybrid" simulations exist, such as fluid equations coupled to Monte Carlo simulations.

Hybrid simulations work quite well and have been used extensively in many different fields of plasma physics such as plasma propulsion (Garrigues et al. 2000), plasma processing (Ventzek et al. 1993, Kwok et al. 2001), fundamental plasma physics (Chabert and Sheridan 2000) etc.

In a very interesting paper, Cartwright et al. (2000) proposed an improvement on the classical hybrid scheme accounting for depleted energy distribution functions. The authors included in their scheme an energy equation to calculate the electron temperature and an electron balance. They also proposed the inclusion of particle electrons to retain some kinetic effects. To some extend, this paper presents a number of similarities with the work presented below, though developed independently. A detailed comparison between the approach below and that of Cartwright et al. (2000) would be interesting, but beyond the scope of the present chapter and thesis.

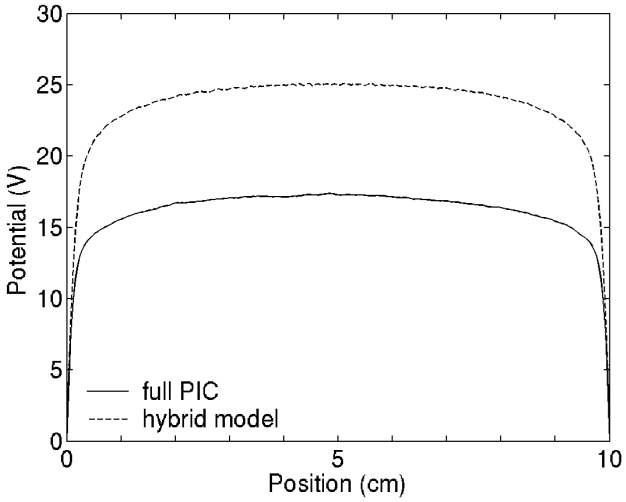

Figure 5.1: The solid and the dashed lines represent the plasma potential profiles obtained with a full particle-in-cell (PIC) simulation and a hybrid simulation, respectively. These two simulations were run under the same conditions. The self-consistently electron temperature calculated with the PIC was used as a parameter in the hybrid.

Some of the disadvantages of most hybrid models is that they are not self-consistent and the assumptions they are based on are not necessarily appropriate. i) They are not self-consistent because the electron temperature is not calculated but is a parameter of the simulation and so is the particle creation source term, i.e. the number of ions injected in the simulation per time step. In principle, the temperature and the creation source term are somewhat related. In classical hybrid simulations, they are both parameters, and their consistency can only be verified *a posteriori*. ii) In addition, assuming that the electrons have a Maxwell-Boltzmann distribution is not necessarily adequate. For example, a *real* low-pressure (a few mTorr) and bounded plasma (where the electron energy relaxation length is larger than the system) would have an electron energy distribution function depleted at energies higher than the plasma potential, as shown in Chapter4. In such a case, assuming a Maxwell-Boltzmann distribution leads to an over-estimation of the electron flux to the wall and therefore to an over-estimation of the plasma potential. This is shown in figure 5.1, where the steady-state plasma potential profiles obtained with a full PIC and a classical hybrid model, under the same conditions of temperature ($T_e = 4.6$ eV), pressure ($P = 1$ mTorr) and plasma density ($n_e = 2.4 \times 10^{15}\text{m}^{-3}$) are compared. For higher pressures, when the PIC electrons have a "more Maxwellian" distribution, the two plasma potential profile are closer.

Another example, where the use of Boltzmann electrons may fail to account for important phenomena, was recently investigated by Meige et al. (2005b). In this paper we show that in Plasma Immersion Ion Implantation (PIII) systems (Conrad et al. 1987, Chu et al. 1996), where a short rise time is applied to the substrate, an electron shock wave may form, heating the electrons up to high energies. Many of these fast electrons are expelled from the plasma leading to

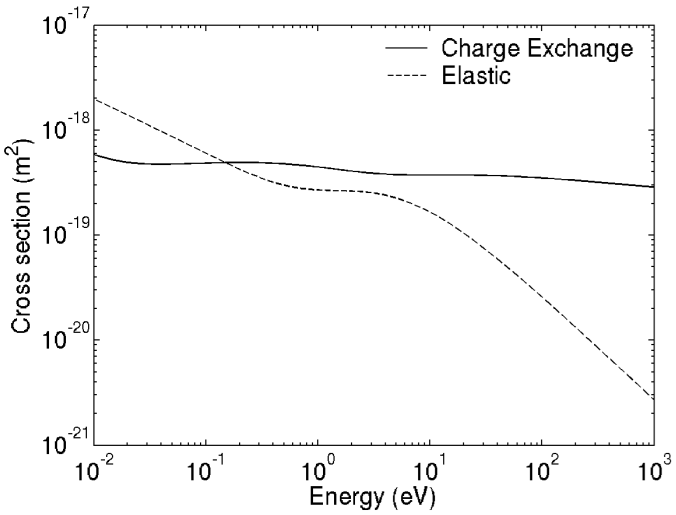

Figure 5.2: Ion-neutral collision cross sections in argon.

a high plasma potential and thus to a high surface electric field on the earthed electrode which could give rise to non-negligible electron field emission. The investigation of short-rise-time-pulse PIII systems is very commonly done by the use of hybrid simulations (Kwok et al. 2001), hence failing to account for any temporal fluctuations less than the plasma frequency, such as the electron shock observed with the full PIC simulation.

In this chapter, the basic equations behind classical hybrid models are presented. Then, a novel scheme, where a Monte Carlo simulation for particle electrons is coupled to the classical hybrid model is presented; this model allows a self-consistent calculation of the electron energy distribution function, accounting for non-Maxwellian distributions, the electron temperature and the source term profiles. Finally, the results obtained with a full PIC simulation, a standard hybrid simulation and the improved hybrid model presented here, are compared. The results obtained with the novel scheme are in much better agreement with the full PIC simulation than the classical non self-consistent hybrid model.

5.2 Basic equations of the hybrid model

5.2.1 Linearization of Poisson's equation

The hybrid simulation follows the same steps as a standard PIC simulation (Birdsall and Fuss 1969, Langdon and Birdsall 1970, Hockney and Eastwood 1988, Birdsall and Langdon 1985). In short, (i) the charges are accumulated on the mesh, (ii) Poisson's equation is solved to find the corresponding electric field, (iii) Newton's law is used to push the particles according to the electric field. These steps constitute one iteration. The iterations are repeated until the simulation reaches the steady state. The ions are treated as particles, while the electrons are assumed to be in Boltzmann equilibrium, i.e. their density is

given by equation 5.1. Note that the ions undergo elastic and charge-exchange collisions with neutrals, following the Monte Carlo scheme developed by Vahedi and Surendra (1995) for PIC simulations and using the cross sections shown in figure 5.2.

In the following, the time integration of Poisson's equation coupled with the Boltzmann relation is presented. Let upper indices refer to a moment in time and let Δt be a time step, with $t^{k+1} = t^k + \Delta t$. Assume that the values of the quantities are known at t^k and to be calculated at t^{k+1}. Equations are given for a one-dimensional system, however, one could easily generalize to two and three-dimensional systems.

Poisson's equation reads

$$\left(\frac{\partial^2 \Phi}{\partial x^2}\right)^{k+1} = -\frac{\rho}{\varepsilon_0} = -\frac{e}{\varepsilon_0}\left(n_i^k - n_e^l\right), \tag{5.2}$$

where n_i is the ion density coming from the accumulation of the particle ion charges on the mesh and n_e the electron density given by the Boltzmann relation. The electron density can be evaluated either at time t^k ($l = k$) or at time t^{k+1} ($l = k + 1$). Evaluation at time t^k is explicit, since all quantities at time t^k are already known. This is computationally attractive, but can lead to fluctuations or even instabilities in the calculation, unless restrictions are applied to the time step Δt. Evaluation at time t^{k+1} must be implicit, since no values are known yet. Implicit treatment does not lead to fluctuations or instabilities, but is harder to implement, since when the electron density is replaced by its expression (equation 5.1), the potential Φ at time t^{k+1} appears on the right-hand side in a non-linear way

$$\left(\frac{\partial^2 \Phi}{\partial x^2}\right)^{k+1} = -\frac{e}{\varepsilon_0}\left(n_i^k - n_0 \exp\frac{e\Phi^{k+1}}{k_B T_e}\right). \tag{5.3}$$

This issue is generally worked around by taking the first order estimate $\tilde{n}_e^{k+1}$ of the electron density at t^{k+1}

$$\tilde{n}_e^{k+1} = n_e^k\left[1 + \frac{e}{k_B T_e}\left(\Phi^{k+1} - \Phi^k\right)\right], \tag{5.4}$$

which allows equation 5.3 to be linearized

$$\left(\frac{\partial^2 \Phi}{\partial x^2}\right)^{k+1} - \frac{1}{{\lambda_D^k}^2}\Phi^{k+1} = -\frac{e}{\varepsilon_0}\left[n_i^k - n_e^k\left(1 - \frac{e}{k_B T_e}\Phi^k\right)\right], \tag{5.5}$$

where the local Debye length, λ_D^k is given by

$$\lambda_D^k = \sqrt{\frac{\varepsilon_0 k_B T_e}{e^2 n_e^k}}. \tag{5.6}$$

The spatial integration of equation 5.5 is not presented here as it can be easily done by any classical algorithm solving tri-diagonal systems (Press et al. 1992) for 1D simulations or five-point equations (Shneider and Zedan 1981) for 2D systems.

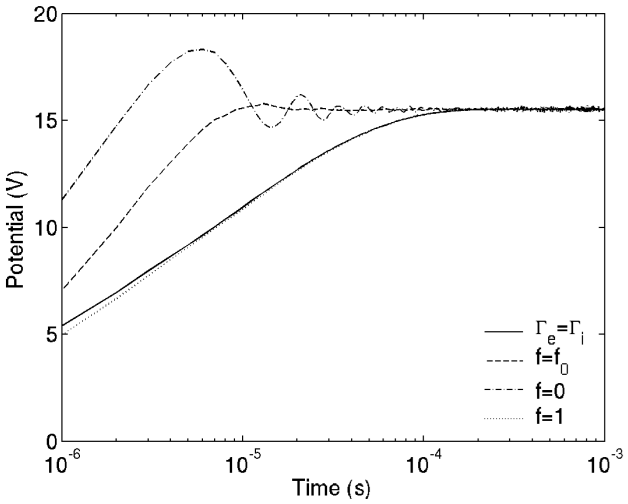

Figure 5.3: Time evolution of the plasma potentials using equation 5.12 (solid line) and 5.17 (broken lines) to calculate n_0. Critical damping is obtained for $f = f_0 = \sqrt{q\Delta t/p}$.

5.2.2 Calculation of the density reference n_0

In hybrid models, the electron density reference n_0 is very commonly imposed or hidden in the normalization of variables. This is not an issue as long as Poisson's equation is not solved, i.e. as long as quasi-neutrality of the plasma is assumed, but care should be taken when the Boltzmann relation is coupled with Poisson's equation as imposing n_0 leads to a miscalculation of the sheath potential and all the associated consequences. Here, various methods to estimate n_0 are proposed.

Steady-state value for n_0

The most straightforward and probably the most stable method to estimate n_0 is to assume (i) that at each instant the electron flux to the walls equals the ion flux and (ii) that the ion flux is balanced by creation in volume (steady-state regime). Let q be

$$q = \oiint_{\mathcal{S}} \frac{1}{4}\overline{v} \exp\left(\frac{e\Phi}{k_B T e}\right) \boldsymbol{n} \cdot \mathrm{d}\boldsymbol{\mathcal{S}}, \tag{5.7}$$

where $\mathcal{S}$ is the surface of the system and $\overline{v}$ is the average electron velocity,

$$\overline{v} = \sqrt{\frac{8k_B T_e}{\pi m_e}}. \tag{5.8}$$

Conditions (i) and (ii) above lead to

$$\oiint_{\mathcal{S}} \boldsymbol{\Gamma}_i \cdot \mathrm{d}\boldsymbol{\mathcal{S}} = \oiint_{\mathcal{S}} \boldsymbol{\Gamma}_e \cdot \mathrm{d}\boldsymbol{\mathcal{S}} = q n_0, \tag{5.9}$$

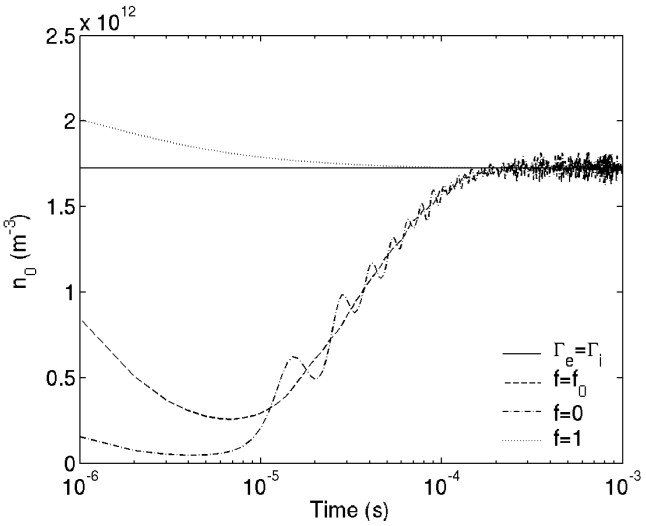

Figure 5.4: Time evolution of the electron density reference n_0 calculated with equation 5.12 (solid line) and 5.17 (broken lines). Critical damping is obtained for $f = f_0 = \sqrt{q\Delta t/p}$.

and

$$\oiint_{\mathcal{S}} \boldsymbol{\Gamma}_i \cdot \mathrm{d}\boldsymbol{\mathcal{S}} = \iiint_{\mathcal{V}} S_{\mathrm{iz}}\, \mathrm{d}\mathcal{V} = S_{\mathrm{iz}}\mathcal{V}, \tag{5.10}$$

respectively. In equations 5.9 and 5.10, $\boldsymbol{\Gamma}_i$ and $\boldsymbol{\Gamma}_e$ are the ion and electron fluxes to the walls respectively and $\mathcal{V}$ the volume of the system. The source term S_{iz} is constant in time, uniform in space and is a parameter of the simulation corresponding to the number of real ions injected in the simulation per unit of time and volume. Equation 5.10 should also account for losses in volume if required (e.g. attachment in the case of discharges with electronegative gases). Combining and rearranging equations 5.9 and 5.10

$$n_0 = \frac{S_{\mathrm{iz}}\mathcal{V}}{q}, \tag{5.11}$$

or

$$n_0 = \frac{4S_{\mathrm{iz}}\mathcal{L}}{\overline{v}\left[\exp\left(\frac{e\Phi_L}{k_B T_e}\right) + \exp\left(\frac{e\Phi_R}{k_B T_e}\right)\right]}. \tag{5.12}$$

for a 1D system and where Φ_L and Φ_R are the left and right wall potentials, respectively and $\mathcal{L}$ the length of the system. This demonstrates what was previously stated: n_0 and S_{iz} cannot be imposed simultaneously, as for a given S_{iz}, there is one and only one value of n_0 satisfying the steady-state null-current condition.

This manner of estimating n_0 is convenient to implement and leads to quite stable simulations as its only time dependency is through the wall potentials Φ_L and Φ_r, which are also constant when grounded. The drawback of this method is that the time development of the discharge (the breakdown) is not properly simulated, hence, only the steady-state quantities are accurate. This could be

slightly improved by computing the real ion flux to the walls at each time step, which would allow any fluctuations on the ion time scale to be followed.

Real electron balance for an accurate time development of n_0[1]

When a proper time development of a discharge is required, one cannot simply assume that the electron flux equals the ion flux. Indeed, this might be true on average in the stationary regime, but it is not necessarily the case in the transitory regime. Hence, the real electron flux to the walls has to be estimated. Let p be

$$p = \iiint_{\mathcal{V}} \exp\left(\frac{e\Phi}{k_B T e}\right) \mathrm{d}\mathcal{V}. \tag{5.13}$$

The total number of electrons present in the system is $N_e = n_0 p$, while the number of electrons lost during a time step is $N_l = n_0 q \Delta t$, q being defined by equation 5.7. Hence, the fraction of electrons lost during a time step is given by

$$\frac{N_l}{N_e} = \frac{q\Delta t}{p}. \tag{5.14}$$

This yields

$$N_e^{k+1} = N_e^k \left(1 - \frac{q\Delta t}{p}\right) + S_{\mathrm{iz}} \mathcal{V} \Delta t, \tag{5.15}$$

where $S_{\mathrm{iz}}\mathcal{V}\Delta t$ is the number of real electrons created in the volume during one time step. This last term should also account for losses in volume if appropriate (e.g. attachment in the case of discharges with electronegative gases, as in Chapter 6). Trivially, n_0^{k+1} is given by

$$n_0^{k+1} = \frac{N_e^{k+1}}{p}. \tag{5.16}$$

Using equation 5.15 and 5.16 to calculate n_0 at each time step leads to instabilities on the plasma potential that eventually damp out. These instabilities are not physical and are just an artifact of the method. A stabilization term to complete equation 5.15 and 5.16 was empirically found

$$n_0^{k+1} = \frac{1}{p}\left[N_e^k \left(1 - \frac{q\Delta t}{p}\right) + S_{\mathrm{iz}} \mathcal{V} \Delta t + f\left(p n_0^k - N_e^k\right)\right], \tag{5.17}$$

where f is an arbitrary coefficient. Critical damping is obtained for $f = f_0 = \sqrt{q\Delta t/p}$. Figure 5.3 shows the time evolution of the plasma potentials using equation 5.12 (solid line) and 5.17 (broken lines) to calculate n_0 for different values of f, while figure 5.4 shows the corresponding values of n_0. Note that this calculation of n_0 was also successfully tried in the case of non-stationary discharges, such as an capacitive rf discharge, where an rf potential is applied at one of the boundaries. Note that Hagelaar (2006) has recently written an report where the approach presented above is detailed.

[1] The calculation of n_0 seems to be an unresolved and not a well-known issue, and to the best of my knowledge, not discussed in the literature, except by Cartwright et al. (2000). The expression of n_0 given in this section is new. I would like to acknowledge my advisor Gerjan Hagelaar for the useful discussions on this topic.

5.2.3 Ion source term profile

In hybrid models, because the electrons are modeled as a fluid, no real collision events occur, and both the electron temperature and the particle creation profiles are parameters of the simulations. The injection of new ions in the simulation is therefore not accomplished in a self-consistent way and may or may not be realistic. In all cases the integral of the particle creation source term, i.e. the number $S_{\text{iz}}\mathcal{V}\Delta t$ of ions injected at each time step, has to be imposed to allow the simulation to reach a steady state. This is equivalent to fixing the power injected in the plasma. The velocity of the new ions injected in the simulation is taken from a Maxwellian distribution at room temperature (0.026 eV). Here, several methods to inject new ions are presented, from the easiest to the most sophisticated.

i) The first method assumes that the source term profile is uniform. In this case the new ions are created uniformly between the two boundaries irrespective of the electron density and temperature.

ii) The real ionization source term is proportional to the electron density and reads $S_{\text{iz}} = k_{\text{iz}} n_n n_e$, where n_n and n_e are the neutral gas and the electron density. It can be assumed that the reaction rate k_{iz} and the neutral gas density n_n are uniform and independent of the electron temperature. Hence, another method is to inject the new ions with a probability proportional to the electron density $n_e(x)$, which is slightly better.

iii) By integrating the cross sections corresponding to ionizing collisions over a certain electron energy distribution (e.g. a Maxwellian distribution or truncated Maxwellian distribution accounting for the high energy depletion), an energy-dependent ionization rate $k_{\text{iz}}(\mathcal{E})$ can be obtained and fitted[2]. By substituting a specified electron temperature profile $\mathcal{E}(x)$ (parameter of the simulation) into the energy-dependent ionization rate $k_{\text{iz}}(\mathcal{E})$, a spatial ionization rate $k_{\text{iz}}[\mathcal{E}(x)]$ profile is determined. In this case, new ions are injected in the simulation with a probability proportional to $k_{\text{iz}}[\mathcal{E}(x)]n_e(x)$. It should then be verified *a posteriori* that

$$\iiint_{\mathcal{V}} S_{\text{iz}} \, \mathrm{d}\mathcal{V} = \iiint_{\mathcal{V}} k_{\text{iz}} n_n n_e \, \mathrm{d}\mathcal{V}, \tag{5.18}$$

where S_{iz} and k_{iz} are both parameters of the simulation. However, this is still limited because the validity of the parameters can only be verified *a posteriori*. In section 5.3, a method to calculate the ionization source term self-consistently is proposed.

5.2.4 Ion radial loss to model 2D effects

In real plasma discharges, particle radial loss might play a significant role, especially when the radius of the system is small compared to its length and when no magnetic field exists to axially confine particles.

[2] Reaction rate coefficients k can generally be well fitted by a generalized Arrhenius function of the energy $\mathcal{E}$, of the form $k(\mathcal{E}) = \exp(a + b\ln\mathcal{E} + c/\mathcal{E} + d/\mathcal{E}^2 + e/\mathcal{E}^3)$.

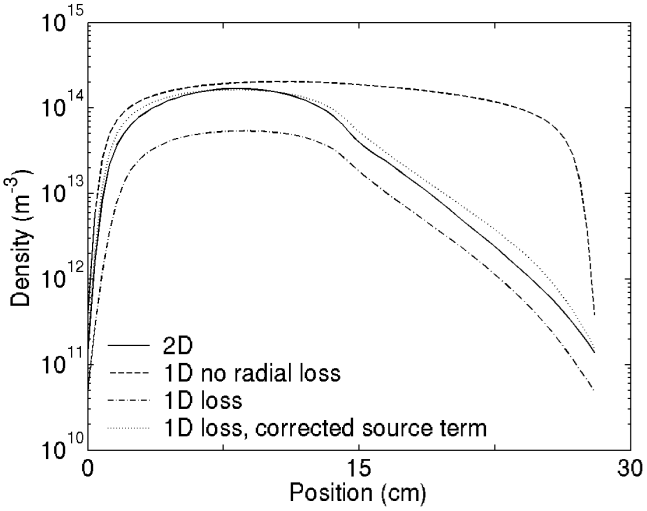

Figure 5.5: Comparison of the electron density profiles with the 2D model (solid line), and the 1D model (broken lines) in the same conditions. For an infinite "virtual" radius (dashed line), the density is rather uniform. For a "virtual" radius equal to that used in the 2D model (dotted and dashed-dotted lines), the density profiles are similar to that obtained with the 2D model.

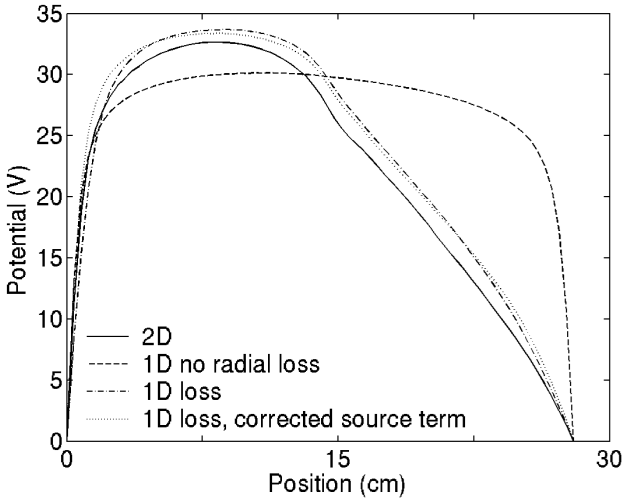

Figure 5.6: Comparison of the plasma potential profiles with the 2D model (solid line), and the 1D model (broken lines) in the same conditions. For an infinite "virtual" radius (dashed line), the potential is rather uniform. For a "virtual" radius equal to that used in the 2D model (dotted and dashed-dotted lines), the potentials are similar to that obtained with the 2D model.

Consider a system in which the radius is very large (infinite or a 1D system with no radial loss) compared to its length and where ionization takes place in the source (left half of the system) only. As shown by the dashed lines in figures 5.5 and 5.6, the electron density and the plasma potential are rather uniform and hardly decrease from the source to the diffusion chamber (right half of the system), despite the fact that the plasma is created in the source. This is because particles can only be lost at either end; hence, although particles are created in the source, they eventually reach the diffusion chamber to fill it up.

This is not the case anymore for a system in which the radius is small compared to its length and where particles can move radially and be lost to the walls before reaching the diffusion chamber. In this later case, differences between the source and the diffusion chamber are enhanced by the particle radial losses, as it is shown by the solid lines in figures 5.5 and 5.6, where the radius is 6 cm (2D model).

In a hybrid model, the radial loss of particles is modeled for ions only; the electron density, given by the Boltzann relation and coupled to the ion density via Poisson's equation automatically follows the ion density. Considering a real system of radius R, the ion radial loss can be modeled for a 1D system as follows. The real radial ion flux to the wall Γ_w is given by

$$\Gamma_w = \Gamma_s = n_s c_s = \alpha n_b c_s, \tag{5.19}$$

where Γ_s, n_s and c_s are the ion flux, density and velocity at the sheath-presheath interface. The ion density n_b in the bulk of the plasma is given by the 1D model. The coefficient α represents the finite divergence of the ion flux (creation and loss in volume). It was empirically adjusted to match results obtained with a 2D hybrid model, $\alpha = 0.75$ (as explained below). The ion sound speed c_s is given by $c_s = \sqrt{k_B T_e / m_i}$. Then, considering that the ion radial flux can be seen as a loss in volume, an ion loss frequency can be defined

$$\nu_{\text{i,loss}} = \frac{2\alpha c_s}{R}, \tag{5.20}$$

where R is the "virtual" radius of the 1D system.

Figures 5.5 and 5.6 show the electron densities and the plasma potentials obtained with the 2D model (solid line), and the 1D model (broken lines) under the same conditions. For an infinite "virtual" radius (dashed line), the density is essentially uniform. The dotted-dashed lines show the density and the potential given by the 1D model, where the "virtual" radius and the ionization source term ($S_{\text{iz}} = 2 \times 10^{18}$ m^{-3}s^{-1}) were equal to that used in the 2D model; α was empirically adjusted to 0.75 in such a way that the density profile was as close as possible to the axial density obtained with the 2D model. The ionization source term was a factor of 3 higher in the 1D compared to the 2D model to improve the matching of the density profiles; this is shown by the dotted lines. Similar calculations were preformed for various densities and geometries and it was found that $\alpha \sim 0.75$ and $S_{\text{iz,1D}} \sim 3 S_{\text{iz,2D}}$ were generally sufficient to simulate the axial behavior of a 2D geometry, with a 1D model.

5.2.5 Stability criteria

A maximal value for the time step is to be found; this maximal time step has to allow harmonic motion of an ion in its own electric field, assuming quasi-neutrality of the plasma. Let us consider a single ion of mass m_i in a cell of size Δx. The ion is moved away from its original position of equilibrium, i.e. from the center of the cell. Its position x is measured with respect to the center of the cell and x is supposed to be small compared to the cell size. The "density" of this single ion is accumulated on the two nodes A and B defining the cell, thus the ion density at each node reads

$$\begin{cases} n_A = \frac{1}{2}\left(1 - 2x/\Delta x\right) \\ n_B = \frac{1}{2}\left(1 + 2x/\Delta x\right) \end{cases} \tag{5.21}$$

If it is assumed that the plasma is quasi-neutral and that the electron are in Boltzmann equilibrium, i.e. that their density is given by equation 5.1, the electric field E created by the single ion reads

$$E = \frac{k_B T_e}{e\Delta x}(\ln n_A - \ln n_B), \tag{5.22}$$

which can be approximated to first order if x is small compared to Δx by

$$E = -\frac{4k_B T_e}{e\Delta x^2}x. \tag{5.23}$$

Applying the law of motion $eE = m_i \partial^2 x/\partial t^2$ yields

$$\frac{\partial^2 x}{\partial t^2} + \frac{x}{\tau^2} = 0, \tag{5.24}$$

with

$$\tau = \frac{\Delta x}{2}\sqrt{\frac{m_i}{k_B T_e}} = \frac{\Delta x}{2c_s}, \tag{5.25}$$

where c_s is the ion sound speed defined above.

The time step Δt of the hybrid simulation has to be short to resolve the harmonic motion of period τ described by equation 5.23, thus

$$\Delta t < \frac{\Delta x}{2}\sqrt{\frac{m_i}{k_B T_e}}. \tag{5.26}$$

5.3 Self-consistent calculations of the electron energy and source term profiles: model *h2x*

5.3.1 Introduction

Hybrid models, such as that presented in section 5.2, are widely used in many fields of plasma physics like plasma propulsion (Garrigues et al. 2000), plasma processing (Ventzek et al. 1993, Kwok et al. 2001), fundamental plasma physics (Chabert and Sheridan 2000) etc. These models provide a complete, description of the discharge, at relatively low computational cost, using the Boltzmann

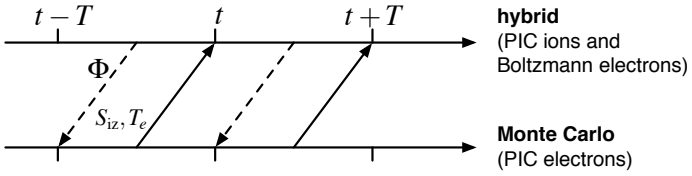

Figure 5.7: The model *h2x* (*hybrid* 2×) is composed of two sub-models coupled to each-other, allowing to self-consistently simulate low-pressure high-density plasmas. i) The first sub-model is a classical hybrid model where the ions are treated as particles while electrons obey the Boltzmann relation and determine the plasma potential. ii) The second sub-model is a Monte Carlo for particle electrons which calculates the electron temperature and the ionization source term.

relation to describe the electron transport, coupled to Poisson's equation to describe the electric field. However, unlike full particle-in-cell simulations, hybrid models are based on restrictive assumptions for the electron energy distribution function (eedf), as it is assumed that electrons have a Maxwell-Boltzmann distribution with a certain temperature, thus failing (i) to account for possible more complex distributions, for example having an over-populated group of low energy electrons or a depleted tail and (ii) to self-consistently calculate the creation source term profiles.

In this section, we show how to self-consistently calculate the electron temperature[3] and the source term profile by coupling a Monte Carlo model for particle electrons to the classical hybrid model. In the following, the novel model shall be called *h2x*, standing for *hybrid* 2× as it is a hybrid PIC-Boltzmann–Monte Carlo.

5.3.2 Coupling the Monte Carlo to the hybrid model: model *h2x*

As shown in figure 5.7, the general concept of *h2x* is to have two sub-models coupled to each-other, each of them using the results of the other as input parameters. Iterations between the two parts of the model are done until the steady state is reached. Each part of the model transfers its results to the other part at a regular period T, a parameter of the simulation. It was empirically found that the update period T should be around 5×10^{-5} s as it has to be sufficiently short to prevent any part of the model from diverging away from the solution and long enough to allow the electron lives to be simulated properly in the Monte Carlo sub-model.

Hybrid sub-model

The hybrid sub-model calculates the plasma potential profile Φ as described in section 5.2 using the electron temperature previously calculated by the Monte Carlo sub-model. The ions are created in the hybrid sub-model following the

[3]Here, the term "temperature" is used loosely, as the eedf may not be Maxwellian. What is meant by "temperature" is "the temperature that would have a Maxwellian distribution with the same mean energy".

ionization source term calculated in the Monte Carlo sub-model. The hybrid sub-model runs for a predetermined period T and the plasma potential profile is then averaged over this period and fed back into the Monte Carlo sub-model.

Monte Carlo sub-model

Since it only describes the electron transport, the Monte Carlo sub-model does not give a complete description of the discharge and requires the input of several plasma quantities such as the electric field. The electric field obtained with the hybrid model is used for this purpose.

Compared to the number of ions followed in the hybrid sub-model, the Monte Carlo sub-model simulates the path of a rather small number of individual electrons, typically less than a thousand. The electrons are followed, one by one, on their passage through the plasma. The occurrence and effect of collisions are treated using random numbers. Elastic, exciting and ionizing electron neutral collisions are taken into account in the model. The way these collisions are treated is developed in section 5.3.3. The velocity of the argon atoms is assumed to be negligible compared to the electron velocity. Furthermore the center of mass of the collision partners is assumed not to move in the laboratory system.

At each iteration of the Monte Carlo, two types of electrons are used. i) The first type is constituted of the electrons that were already present during the previous iteration and that have not escaped to the walls. These electrons are put back in the new potential well. Putting these "old" electrons in a new potential well may lead to numerical cooling or heating, however this the best that can be done, as no assumption should be made on the initial electron energy. ii) The second type of electrons correspond to the "new" sample electrons injected at each Monte Carlo iteration. Their number N_s is fixed and is a parameter of the simulation. These "new" electrons are taken from the real ionization events that occurred during the previous Monte Carlo iteration. If the number N_{iz} of real ionization events that previously took place is greater than N_s, the surplus of these events is simply dropped. On the contrary, if N_{iz} is smaller than N_s, the real events are duplicated. In the improbable case of having no real events at all, the "new" electrons are taken from a 2 eV Maxwellian distribution. The number N_s of sample electrons should match the number N_{iz} of ionizations really taking place. This is explained in details in section 5.3.4.

At the end of a Monte Carlo iteration, the newly calculated electron temperature and the source term profile are averaged over the period T and fed back into the hybrid model for the next iteration to correct the electric field in a self-consistent way.

Note that the newly computed electron temperature T_e^{new} is actually fed back into the hybrid side using the following algorithm

$$T_e^{new} = \alpha T_e^{old} + (1-\alpha) T_e^{MC}, \tag{5.27}$$

where T_e^{old} is the previous electron temperature used in the hybrid, T_e^{MC} is the electron temperature calculated in the Monte Carlo and α is a coefficient of

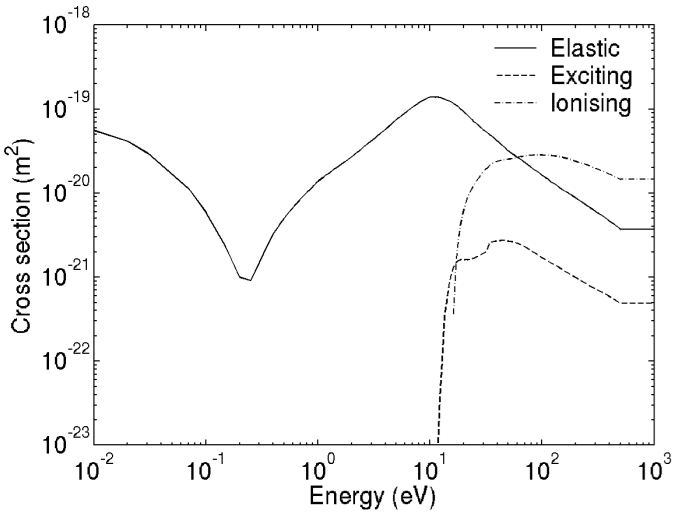

Figure 5.8: Electron-neutral collision cross sections in argon.

under-relaxation. The temperature should be allowed to change rapidly before reaching steady state, and then should be quite stable. Thus, α is defined by

$$\alpha = 1 - \exp\left(-\frac{t}{\tau}\right), \tag{5.28}$$

where τ is the characteristic time over which the under-relaxation becomes "strong". Typically, $\tau = 50T$, where T is the update period defined previously, was used. This allows a very weak under-relaxation of the temperature during the first micro-seconds, with an increasing strength as steady state is reached.

5.3.3 Simulation of an electron path

Here, the simulation of the path of an individual electron is described. Consider a test electron somewhere in the plasma at a moment $t = t_0$. The probability P that the electron has no collision before time t is given by

$$P(t) = \exp\left(-\int_{t_0}^{t} \nu_t t' \, \mathrm{d}t'\right), \tag{5.29}$$

where total collision frequency ν_t depends on both the position x and the energy $\mathcal{E}$ of the electron, and reads

$$\nu_t(x, \mathcal{E}) = \sum_k \nu_k(x, \mathcal{E}) = \sum_k n_n(x)\sigma_k(\mathcal{E})\sqrt{\frac{2\mathcal{E}}{m_e}}, \tag{5.30}$$

where n_n is the neutral gas density and where $\sigma_k(\mathcal{E})$ represents the various cross sections taken into account in the Monte Carlo and shown in figure 5.8. The probability for the electron to undergo a collision, after t_0, between t and $t + dt$ is given by

$$p(t)dt = P(t) - P(t + dt) = \nu_t(t)P(t). \tag{5.31}$$

Therefore a random collision time t_c can be determined

$$\int_{t_0}^{t_c} p(t)\,\mathrm{d}t = R_1 \int_{t_0}^{\infty} p(t)\,\mathrm{d}t, \tag{5.32}$$

where R_1 is a uniformly distributed random number between 0 and 1. The direct calculation of t_c would be cumbersome. The null collision method (Skullerud 1968) simplifies this calculation. In essence, this method introduces an imaginary collision type with frequency ν_0 such that when added to the other collision frequencies the total collision frequency becomes independent of energy and position. This imaginary collision type is called *null collision* as it has no real effect on the electron. The total collision frequency ν_t', including ν_0 is therefore given by

$$\nu_t' = \nu_0(x, \mathcal{E}) + \nu_t(x, \mathcal{E}) = \max_{x,\mathcal{E}} \nu_t(x, \mathcal{E}), \tag{5.33}$$

which when applied to equation 5.32 yields

$$t_c = t_0 - \frac{1}{\nu_t'} \ln(1 - R_1). \tag{5.34}$$

Between two collisions, i.e. between t_0 and t_c, the electron moves freely according to the law of motion

$$\frac{\partial^2 x}{\partial t^2} = -\frac{e}{m_e} E(x), \tag{5.35}$$

which has to be integrated. As the electric field profile E is arbitrary, the integration of equation 5.35 is done numerically using the well-known leapfrog scheme (Birdsall and Fuss 1969).

Once the energy $\mathcal{E}_c$ and the position x_c at the moment t_c of the collision are known, the nature of the collision is determined from another uniformly distributed random number R_2 between 0 and 1, taking into account the relative probabilities of the various collision types. Since the null collision method is used to find t_c, one of the possible collision types is the null collision, which has no effect on the electron. The other collision types affect the electron velocity and energy.

The change in the direction of the electron velocity after a collision is described by two angles, the azimuthal angle ϕ and the scattering angle χ which are determined in the same way as Vahedi and Surendra (1995): considering the differential cross section, one can estimate χ as follows

$$\cos\chi = \frac{2\mathcal{E}_0 + \mathcal{E}_c - 2(\mathcal{E}_0 + \mathcal{E}_c)^{R_3}}{\mathcal{E}_c}, \tag{5.36}$$

where $\mathcal{E}_0 = 1$ eV and R_3 is another uniformly distributed random number between 0 and 1. Equation 5.36 gives an anisotropic scattering angle, i.e. mostly small angles (forward scattering) are obtained for energetic incident electrons,

while the scattering is more isotropic for low energy electrons. The azimuthal angle ϕ is uniformly distributed between 0 and 2π:

$$\phi = 2\pi R_4, \tag{5.37}$$

where R_4 is another uniformly distributed random number between 0 and 1. The direction of the scattered velocity is obtained by geometric considerations

$$\boldsymbol{v}_{\text{scat}} = \boldsymbol{v}_{\text{inc}} \cos\chi + \boldsymbol{v}_{\text{inc}} \times \boldsymbol{i} \frac{\sin\chi \sin\phi}{\sin\theta} + \boldsymbol{v}_{\text{inc}} \times (\boldsymbol{i} \times \boldsymbol{v}_{\text{inc}}) \frac{\sin\chi \sin\phi}{\sin\theta}, \tag{5.38}$$

where $\boldsymbol{v}_{\text{inc}}$, $\boldsymbol{v}_{\text{scat}}$ and $\boldsymbol{i}$ are unit vectors parallel to the incident and scattered velocities and the x axis, respectively. Also, $\cos\theta$ is defined by $\cos\theta = \boldsymbol{v}_{\text{inc}} \cdot \boldsymbol{i}$. The energy loss for all the collisions is given by

$$\Delta\mathcal{E} = \frac{2m_e}{M}(1 - \cos\chi)\mathcal{E}_c, \tag{5.39}$$

where m_e and M are the electron and neutral masses, respectively. In an inelastic collision, the incident electron loses the energy corresponding to the threshold and is then scattered.

5.3.4 Control of the electric field amplitude

The mechanism heating the electrons in the Monte Carlo sub-model is similar to that described in Meige et al. (2005a). In short, an rf electric field is applied in the y direction, perpendicular to the spatial dimension of the simulation, x. Momentum and energy are transfered to the other x and z directions via electron-neutral collisions.

The number N_s of sample electrons, i.e. the number of new electrons injected into the Monte Carlo at each communication time, should match the number N_{iz} of ionizations really taking place. This is done by adjusting the amplitude $E_{y,0}$ of the electric field, at each communication time as follows

$$E_{y,0}^{\text{new}} = E_{y,0}^{\text{old}} \left[\alpha + (1 - \alpha) \frac{N_s}{N_{\text{iz}}} \right], \tag{5.40}$$

where α is a coefficient of under-relaxation. The best compromise was met with $\alpha = 0.2$. This value of under-relaxation allows the amplitude of the electric field to react fast enough, but without being too sensitive to the statistical noise. However, this value was adequate for the range of parameters that were tried, but the under-relaxation should not be strong at the beginning of the discharge to allow the field to react quickly enough during the transitory regime, but then should get increasingly stronger while approaching the steady state. Thus, having α defined by equation 5.28 works also rather well.

5.3.5 Matching the Monte Carlo and hybrid electron densities

When the model was first developed, it was not expected to have to "adjust" anything to force the electron density in the Monte Carlo and the hybrid to

match, as it was thought to occur naturally. This was actually not the case at all, as the electron density in the hybrid turned out to be several times smaller than in the Monte Carlo. The reason for this is that in the hybrid sub-model, the electrons have a Maxwell-Boltzmann distribution by definition, while on the Monte Carlo side, due to the electrons lost to the walls and inelastic collisions, the particle electrons have a depleted distribution. Hence, the electron flux to the wall, used in the hybrid model was over-estimated, leading to an under-estimation of n_0 (equation 5.12 or 5.17) and an over-estimation of the plasma potential. Therefore, the over-estimated plasma potential, calculated on the hybrid side and used as a parameter for the Monte Carlo led to an over-estimation of the density of the more confined particle electrons.

The inconsistency between the electron densities of the two sub-models is not a problem as such, as long as it is known. However, the over-estimation of the plasma potential leads to a miscalculation of the ionization source term profile as the electron life time was considerably over-estimated. To make this point clear, an electron generally has a rather short time to undergo an ionizing collision as its energy has to be above the ionizing threshold but below the plasma wall potential, energy above which the electron would be lost to the walls. When the plasma potential is over-estimated, even if it is only by a few volts, the electron life time is completely miscalculated and so is the creation source term.

Solving this issue was one of the most challenging tasks in developing the model, as most of the attempts led to strong instabilities or worse. To fix the issue, the over-estimation of the electron flux to the wall on the hybrid side has to be adjusted, with respect to the Monte Carlo side of the model. Knowing that the densities of the Monte Carlo and the hybrid should be equal, a correcting coefficient on the electron flux to the wall Γ_e was introduced to impose the equality,

$$\left[\oiint_{\mathcal{S}} \boldsymbol{\Gamma}_e \cdot \mathrm{d}\boldsymbol{\mathcal{S}}\right]_{\text{corrected}} = \gamma \left[\oiint_{\mathcal{S}} \boldsymbol{\Gamma}_e \cdot \mathrm{d}\boldsymbol{\mathcal{S}}\right]_{\text{Maxwellian}}, \tag{5.41}$$

where γ is given by,

$$\begin{aligned} \gamma^{\text{new}} &= \gamma^{\text{old}} \left(\frac{n_{\text{e,hyb}}}{n_{\text{e,MC}}}\right)^{0.05} && \text{if } 2\left|\frac{n_{\text{e,hyb}}-n_{\text{e,MC}}}{n_{\text{e,hyb}}+n_{\text{e,MC}}}\right| > 0.05, \\ &= \gamma^{\text{old}} && \text{otherwise.} \end{aligned} \tag{5.42}$$

The coefficient γ adjusts itself very slowly to make the ratio $n_{\text{e,hyb}}/n_{\text{e,MC}}$ tend to 1. Also, γ is subject to hysteresis to avoid triggering oscillations, i.e. if the relative difference between the two densities is less than 5%, γ is not changed. Instead of calculating n_0 with the Maxwellian electron flux as shown before by equation 5.17, the "corrected" electron flux is used, giving

$$n_0^{k+1} = \frac{1}{p}\left[N_e^k\left(1 - \frac{\gamma q \Delta t}{p}\right) + S\mathcal{V}\Delta t + f'\left(pn_0^k - N_e^k\right)\right], \tag{5.43}$$

where $f' = f'_0 = \sqrt{\gamma q \Delta t / p}$.

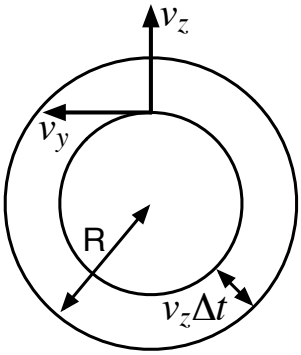

Figure 5.9: Schematic of the section of a plasma discharge at a certain position x. The local radius at the position x is R. The component of the electron speed parallel to the wall is chosen to be v_y (direction parallel to the heating rf electric field), while the component perpendicular to the wall is chosen to be v_z. The electrons that may be lost within Δt are within the ring of thickness $v_z \Delta t$.

Before finding the solution above (equation 5.42), several other methods were investigated, however, as stated before, they all led to strong instabilities. For example, γ was first defined by

$$\gamma^{\text{new}} = \gamma^{\text{old}} \left[\alpha + (1-\alpha) \frac{n_{\text{e,hyb}}}{n_{\text{e,MC}}} \right], \tag{5.44}$$

where α was a coefficient of under-relaxation. If the under-relaxation was not strong enough, any variation in one of the electron densities lead to an over-reaction of γ, while too small over-relaxation lead to unstable oscillations as γ was reacting to slowly to any changes.

5.3.6 Electron radial loss to model 2D effects

As already stated, the particle radial loss might play a significant role in some discharges, especially when the radius of the system is small when compared to its length and when no magnetic field exists to axially confine particles. When the ion radial loss is activated in the hybrid sub-model, a similar mechanism should exist for the particle electrons in the Monte Carlo sub-model.

Assume that for a given position along x there is a radially uniform electron distribution of density n_e and that the wall axis is along z (the heating mechanism acting along y). An electron having an energy greater than the local plasma potential Φ has a certain probability to be lost radially. Finding the number of electrons in the ring of thickness $v_z \Delta t$ (figure 5.9), where v_z is the electron velocity along z, yields an estimation of the electron radial loss frequency

$$\begin{aligned} \nu_{\text{e,loss}} &= |v_z/R| \quad \text{if } \mathcal{E}_z > \Phi, \\ &= 0 \qquad\quad \text{otherwise.} \end{aligned} \tag{5.45}$$

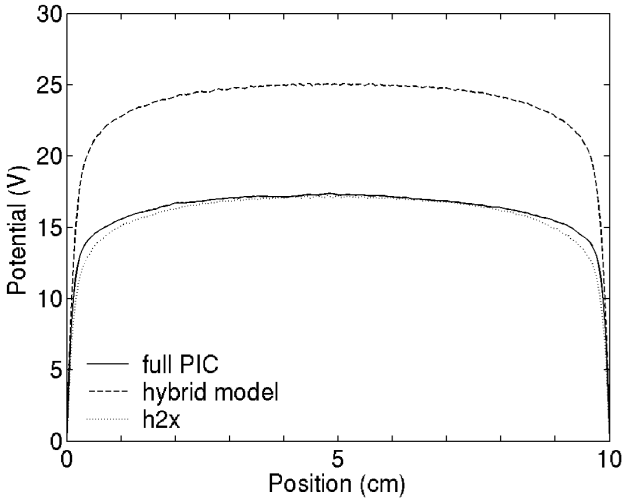

Figure 5.10: Plasma potential profiles with a full particle-in-cell (PIC) simulation (solid line), the standard hybrid simulation (dashed line) and the model *h2x* (dotted line). The three simulations were run under the same conditions. The electron temperature, calculated self-consistently with the PIC, was used as a parameter in the hybrid.

5.4 Results and applications: comparison PIC, hybrid and *h2x*

Here, the results obtained with a full particle-in-cell simulation, a classical hybrid model and the model *h2x* are compared. The conditions of pressure ($P =$ 1 mTorr), temperature ($T_e = 4.6$ eV), plasma density ($n_e = 2.4 \times 10^{15} \mathrm{m}^{-3}$) and neutral gas (argon) are the same. The electron temperature self-consistently calculated with the PIC model was used as a parameter in the classical hybrid model.

Whilst a full PIC simulation requires several hours of calculation for the present conditions, it is only a question of minutes for the classical hybrid simulation and a few dozens of minutes for the model *h2x*. The numerical constraints for the *h2x* model are not as strong as for the full PIC as nor the time step or the cell size have to resolve the electron plasma frequency or the Debye length, respectively. However, i) the time step in the hybrid sub-model has to allow ion oscillations, as shown by equation 5.26 in section 5.2.5, which leads to time steps on the order of 10^{-7} s. ii) The time step in the Monte Carlo sub-model has to be small enough to prevent too many electrons from crossing entire cells, which leads to time steps on the order of 5×10^{-10} s, although it depends on the number of cells.

Figure 5.10 shows the steady-state plasma potential profiles for the different models. The plasma potential given by the PIC simulation will be the reference as PIC simulations have been thoroughly studied and their validly has been proven. The plasma potential in the bulk, with respect to the grounded walls is 17.4 V. Hence the the ratio $e\Phi/k_B T_e = 3.8$ and is smaller than the theoretical

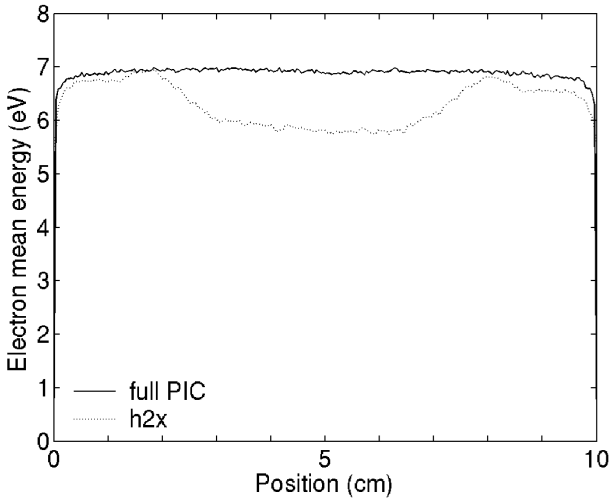

Figure 5.11: Electron mean energy profiles with a full particle-in-cell (PIC) simulation (solid line) and the model *h2x* (dotted line). The two simulations were run under the same conditions and are both self-consistent.

ratio of 5.2 obtained assuming a Maxwellian distribution (see Lieberman and Lichtenberg 2005, p. 172). The reason for this is that the eedf in the PIC simulation is not Maxwellian, the tail is depleted at high energies due to the electron lost to the walls and electron-neutral inelastic collisions. The electron flux to the walls and, as a result, the plasma potential and the ratio $e\Phi/k_BT_e$ are therefore smaller than they would be assuming a Maxwellian-Boltzmann distribution.

The dashed line shows the plasma obtained with the classical hybrid model where the electrons are "forced" to have a Maxwell-Boltzmann distribution by definition. The plasma potential is higher by almost 8 V and the ratio $e\Phi/k_BT_e = 5.5$ is therefore closer to the theoretical value. The difference between the hybrid model and the theoretical approach comes from the fact that, under the present conditions, the ions are not completely collisionless in the simulation, while they are assumed to be so in the theoretical approach. Compared to the collisionless case, collisions reduce the ion flux to the walls, which leads to a greater plasma potential. In summary, hybrid simulations are attractive for their low computational cost, but care should be taken when simulating low-pressure plasmas where the real eedf would not actually be Maxwellian.

The dotted line shows the plasma potential obtained with *h2x*, the self-consistent model. Although Boltzmann electrons are used in the hybrid sub-model, the correcting coefficient calculated via the Monte Carlo sub-model (Section 5.3.5) allows a more realistic electron flux to the walls to be calculated and thus a more realistic plasma potential. The ratio $e\Phi/k_BT_e$ in the model *h2x* is very close to that obtained the with PIC simulation. A small difference is observed in the shape of the potential profile. Although the "height" of the plasma potential profiles are the same for the PIC and the model *h2x*, the local plasma potential is slightly lower in the model *h2x* around the sheath – pre-

sheath region. This is presumably a consequence of the inconsistency between the transport of the Boltzmann electrons and the particle electrons.

Figure 5.11 shows the electron mean energy profiles obtained with the PIC and the model *h2x*. The electron mean energy for the PIC is, as expected, rather uniform. This is not the case for that obtained with the model *h2x* which presents a dip in the center of the discharge. This is presumably a consequence of the shape of the plasma potential. Although the potential well height is adapted for particle electrons via the correcting coefficient, its shape is not, since it is calculated solving Poisson's equation with Boltzmann electrons. Low energy particle electrons are therefore slightly more confined in the center of the discharge by the less flat potential profile, leading to a decrease of the electron mean energy in the confinement region. In future, a solution to this issue should be sought.

5.5 Conclusion

It was shown that classical hybrid simulations where ions are treated as particles and electrons are assumed to have a Maxwell-Boltzmann distribution, in addition to not being self-consistent, may lead to a miscalculation of the plasma potential.

An alternative to the fully-consistent computationally-expensive particle-in-cell simulations and hybrid simulations was proposed. This novel scheme, that was named *h2x* is composed of two coupled sub-models. Globally, the ions are treated as particles, while the electrons are treated simultaneously as a fluid obeying the Boltzmann relation and as particles.

Results obtained with the model *h2x* are in much better agreement with the full PIC simulation than the classical non self-consistent hybrid model, as it accounts for non-Maxwellian electron energy distribution functions.

Chapter 6

Simulations of double layers in electronegative plasmas

6.1 What makes electronegative plasmas different?

Electronegative plasmas are those where electrons have the ability to attach onto neutral atoms or molecules, thus forming a significant amount of negative ions. (Franklin 2002)

Although the research work done on electronegative gases is historically mostly driven by curiosity (see Emeleus and Woolsey 1970, and references therein), the extreme interest in these electronegative plasmas is now essentially led by the micro-chip industry.

Properties of electronegative plasmas are somewhat different from that of electropositive discharges that owe most of their properties to the large mass difference between the positive and negative charges. The reason why electronegative plasmas are so different from electropositive plasmas arises from the fact that the negative ion mass is much larger than the electron mass and their temperature is much lower than the electron temperature. Therefore the sheaths slowing down the electrons, and accelerating the positive ions towards the wall, reduces the negative ion wall flux to zero. Hence, negative ions are essentially created and destroyed in the volume of the plasma, as opposed to the other charged species that are essentially lost to the walls.

In the same way as the Bohm criterion is fundamental in electropositive discharges, its equivalent in electronegative plasmas also plays a significant role. At low pressures, an analogue to the Bohm speed was derived and is now well established (Braithwaite and Allen 1988, Franklin and Snell 1992)

$$u_s^2 = \frac{k_B T_+}{m_+} + \frac{kT_e T_-}{m_+} \frac{n_e + n_-}{T_- n_e + T_e n_-}, \tag{6.1}$$

where T_e, T_- and T_+ are the electron, negative ion and positive ion temperatures, respectively; n_- and n_e are the respective densities and m_+ the positive ion mass. It was suggested and then shown by Braithwaite and Allen (1988) that under certain conditions, typically $\gamma = T_e/T_- > 10$ and $\alpha > 3$ at the plasma edge, the plasma and the collisionless sheath could not join smoothly

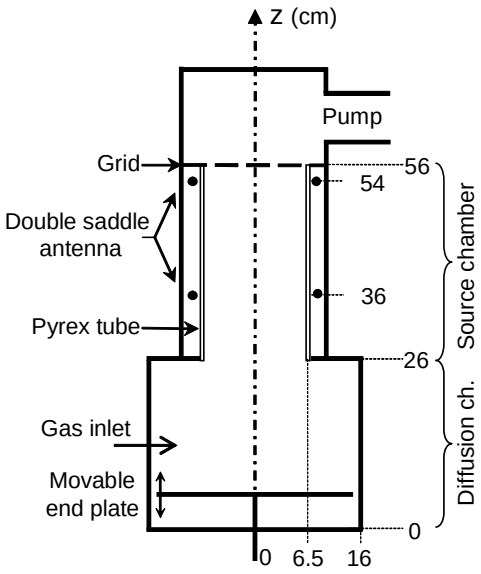

Figure 6.1: Schematic of the experimental setup (Plihon et al. 2005b).

and that the potential at the plasma edge becomes multi-valued. The plasma core region is terminated by an electric double-layer potential structure followed by spatial oscillations of the order of the Debye length which eventually terminate in a standard positive-ion-electron sheath. Although the presence of a double layer in front of the sheath has been observed in various models (Kouznetsov et al. 1999, Sheridan 1999, Sheridan et al. 1999ba, Chabert and Sheridan 2000, Boeuf 1987), the spatial oscillations following the double layer are claimed to be an artifact of the fluid equations; they have been observed in fluid models (Sheridan 1999, Sheridan et al. 1999b), but not in kinetic models (Kouznetsov et al. 1999, Sheridan et al. 1999a, Chabert and Sheridan 2000). Note that Kono (2001) showed that the spatial oscillations predicted by fluid models may actually correspond to real temporal instabilities in kinetic models.

Although double layers appear to be a common feature and have been extensively studied in electropositive discharges, they are much less known in electronegative plasmas.

6.2 Double-layer formation in the vicinity of the expanding region of an electronegative plasma

Recent experiments by Plihon et al. (2005ab) have demonstrated that double layers could form in the expanding region of an inductively coupled electronegative plasma composed of an Ar/SF_6 mixture. The experimental setup is similar to that of Charles and Boswell (2003), but without the use of a static diverging magnetic field. A schematic of the reactor is shown in figure 6.1. The system is composed of a source chamber, a 30-cm-long 15-cm-diameter cylinder of pyrex and surrounded by a double-saddle helicon antenna (Boswell 1970); the source

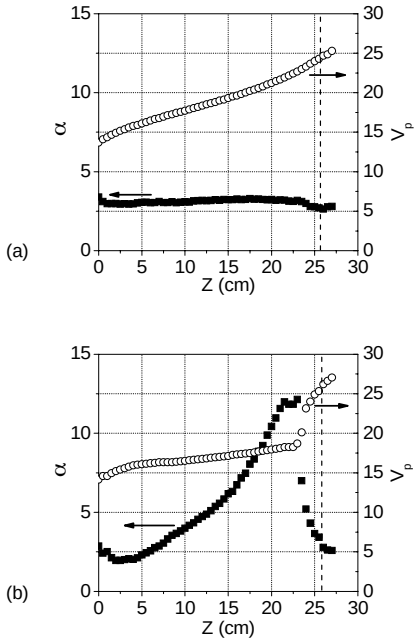

Figure 6.2: Spatial evolution of the plasma potential V_p and the electronegativity $\alpha = n_-/n_e$, in (a) the no DL case (6% SF_6 mixture), and (b) the DL case (9% SF_6 mixture), at 1 mTorr, 600 W (Plihon et al. 2005a).

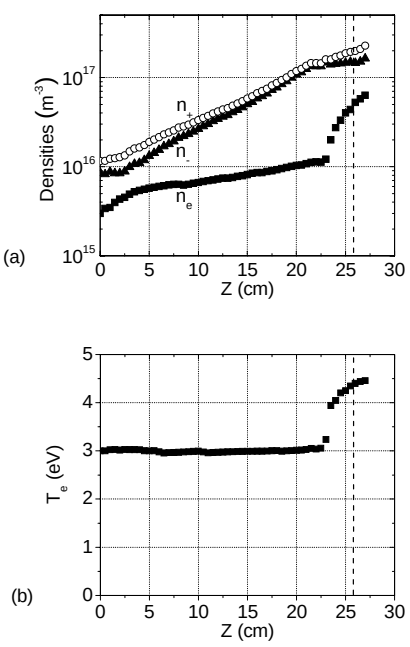

Figure 6.3: Spatial evolution of the particle densities and electron temperature for a 9% SF_6 mixture at 1 mTorr, 600 W (Plihon et al. 2005a).

is attached to a 26-cm-long 32-cm-diameter aluminum diffusion chamber. The helicon antenna is powered by an rf power supply operating at 13.56 MHz and capable of delivering 2 kW of forward power. The plasma is inductively heated (the helicon source is not operated in helicon mode).

Plihon et al. (2005a) showed that a stable double layer is formed in the vicinity of the expanding region of the system for a rather narrow range of parameters. For a neutral gas pressure of 1 mTorr and an input power of 600 W, stable double layers are formed for relative concentrations of SF_6 between 8% and 13%. For pressures below this window, no double layer is observed, while above this window, propagating double layers are observed. Figure 6.2 shows their measurement of the electronegativity α and the plasma potential V_p in both the non-DL (a) and DL (b) cases. In the later case, a potential drop of ~ 7 V (at the discontinuity position) corresponding to the double layer is observed accompanied by a maximum of the electronegativity of ~ 12. A full parametric investigation of the periodic formation of propagating double layers is presented in Plihon et al. (2005b). As shown in figure 6.4, the propagating double layers were born in the vicinity of the interface between the two chambers and propagate downwards, in the diffusion chamber. The speed and frequency of these propagating DLs are such that irrespective of the parameters, the number of DLs simultaneously present in the system is constant. The speed of

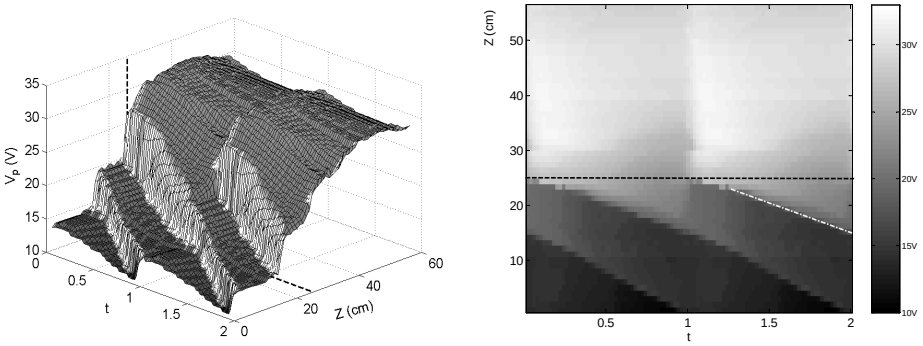

Figure 6.4: Spatiotemporal evolution of the plasma potential, two instability periods for a 25% SF_6 concentration plasma at 600 W and 1 mTorr. A 3D representation and a gray level amplitude image are shown (Plihon et al. 2005b).

propagation is of the order of 150 m/s and the frequency is of the order of kHz. The authors also compared their propagating double layers to the downstream instabilities observed by Tuszewski and White (2003), Tuszewski et al. (2003) and Tuszewski and Gary (2003). The two phenomena have many common features such as the propagating speed, the range of frequency etc., but there are also differences especially concerning the charged particle dynamics. Tuszewski and Gary (2003) have shown that their downstream instability was consistent with ion two-stream instabilities that would appear when positive and negative ions develop sufficiently large relative drift velocities in the downstream region.

Note that the electronegativity values reported by Plihon et al. (2005ab) were estimated assuming quasi-neutrality of the plasma. Recent experiments by Plihon (2005, private communication) and Plihon (2006), using a probe-based photo-detachment technique to directly detect negative ions in the plasma showed that the maximum of the electronegativity is actually ~ 1.3 in the case of the stable double layer and ~ 4 in the case of the propagating double layers. The electronegativity may be greater than the values above by 40% at most, depending on the dominant negative ion in the system, but is still smaller than the original estimation.

The physical processes underlying the formation of (propagating) double layers remain unclear, although it is now well established that double layers can form in low-pressure electronegative plasmas (Kouznetsov et al. 1999, Sheridan 1999, Sheridan et al. 1999ba, Chabert and Sheridan 2000, Boeuf 1987). The primary goal of this chapter is to investigate plasma discharges similar to that of Plihon et al. (2005ab) so as to shed light on the critical parameters and the conditions of formation of (propagating) electronegative double layers. This is first done by the use of a two-dimensional hybrid model and for the sake of self-consistency, the model *h2x* presented in Chapter 5 is then modified to handle electronegative discharges.

6.3 2D hybrid simulations of electronegative double layers

6.3.1 Model

The two-dimensional (2D) hybrid model developed for the present study describes the electrons as a fluid obeying the Boltzmann relation while both positive and negative ions are treated as particles. This follows the classical hybrid model scheme presented in Chapter 5. The main differences, essentially due to the presence of a third species (the negative ions), are presented in this section. The spatial discretization of Poisson's equation is detailed in Appendix 8.3.

Due to the presence of the third species, namely the negative ions, a number of events, such as attachment, detachment and recombination, have to be treated in addition to ionization. The attachment of electrons onto neutral atoms or molecules is the mechanism that gives birth to negative ions in the discharges. Negative ion loss processes in electronegative discharges fall in two categories, namely the detachment of an electron from a negative ion and the recombination of a positive and a negative ion. Certain gases, such as oxygen, are detachment-dominated, others, such as SF_6, are recombination-dominated. In the present model, a mixture of Ar and SF_6 is to be investigated and it is assumed that the mixture Ar/SF_6 is recombination-dominated.

The ionization, attachment and recombination source terms are given by

$$\begin{aligned} S_{\text{iz}} &= K_{\text{iz}} n_n n_e = \nu_{\text{iz}} n_e, \\ S_{\text{att}} &= K_{\text{att}} n_n n_e = \nu_{\text{att}} n_e, \\ S_{\text{rec}} &= K_{\text{rec}} n_+ n_-, \end{aligned} \tag{6.2}$$

respectively, where K_{iz}, K_{att} and K_{rec} are the ionization, attachment and recombination rate coefficients, respectively; n_n is the neutral gas density, ν_{iz} and ν_{att} are the ionization and attachment frequencies, respectively.

The various events (ionization, attachment and recombination) occur with a probability following their respective source term profiles involving the local electron density, the positive and negative ion densities. These densities are results from the simulation while the various rate coefficients are parameters of the simulation.

Although in reality the ionization and attachment rate coefficients depend on the form of the electron energy distribution function and, to some extend, on the electron temperature, the particular effect of each reaction is to be investigated independently. Hence, ionization and attachment rate profiles are taken as independent parameters of the simulation rather than being imposed by a single temperature profile.

6.3.2 Formation of a stable double layer

Figure 6.5 is a schematic of the simulated domain. Plihon's reactor was scaled down by a factor of 2 for computational time reasons. Table 6.1 gives the general parameters that were used for the present study.

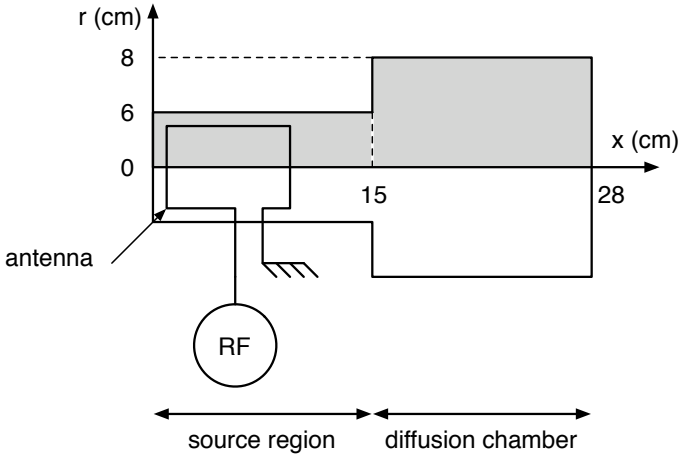

Figure 6.5: Schematic of the experimental setup and simulated domain. The gray area represents the simulated domain.

Table 6.1: General parameters of the 2D hybrid simulations.

Quantity	Value
system dimensions	30×10 cm
cell number	75×50
total duration	1-10 ms
time step	5×10^{-8} s
macro-particle weight	5×10^{6} m^{-3}
positive and negative ion mass (Ar)	6.68×10^{-26} kg
positive and negative ion charge	$+e$ and $-e$
electron temperature (Boltzmann relation)	4 eV
room temperature	297 K
source term	2×10^{18} m^{-3}s^{-1}
K_{rec}	1.1×10^{-10} m^{3}s^{-1}

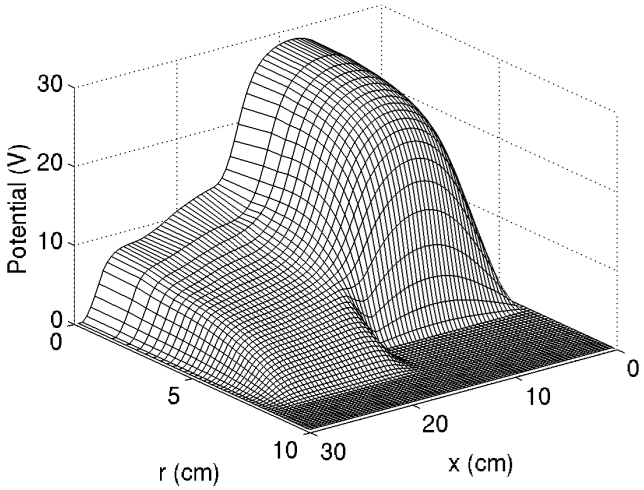

Figure 6.6: Steady-state plasma potential profile of a stable double layer.

Figure 6.6 shows the steady-state plasma potential in conditions where the plasma sustains a double layer at the interface of the source and the diffusion chamber. This double layer was obtained for the following conditions: the ionization frequency was 1.1×10^5 s^{-1} in the source, decreasing to 2.2×10^4 s^{-1} in the diffusion chamber. The attachment frequency was null in the source and 1.1×10^5 s^{-1} in the diffusion chamber. The recombination rate was $K_{\text{rec}} = 1.1 \times 10^{-10}$ m^3 s^{-1}, which is an extremely large value, but which was chosen to make the recombination significant, as discussed later. In this case, time-resolved densities and plasma potentials remain rather constant and the double layer is stable. Although the geometrical transition from the source to the diffusion chamber enhances the potential drop, it was found that the transition itself was not a critical parameter for the formation of the double layer in the simulation.

Figure 6.7 shows the spatially averaged densities over the source radius corresponding to the case above. This shows that the double layer separates a plasma essentially electropositive on the high-potential side from a highly electronegative plasma on the low-potential side, which seems to be in good qualitative agreement with the stable double layer reported by Plihon et al. (2005a).

The solid line in figure 6.8 represents the same plasma potential as in figure 6.6, averaged over the source radius; a potential drop of about 15 V is observed. The dashed line shows the plasma potential in the exact same conditions but without negative ions. A smooth decrease of the plasma potential corresponding to a classical diffusion profile is observed, but no double layer.

The double layer could only be formed when the source region was ionization-dominated, while the diffusion chamber was attachment-dominated. However, these conditions were not sufficient: the required significant downstream electronegativity can be obtained with i) low attachment and low recombination or ii) high attachment and high recombination. The former case does not lead to

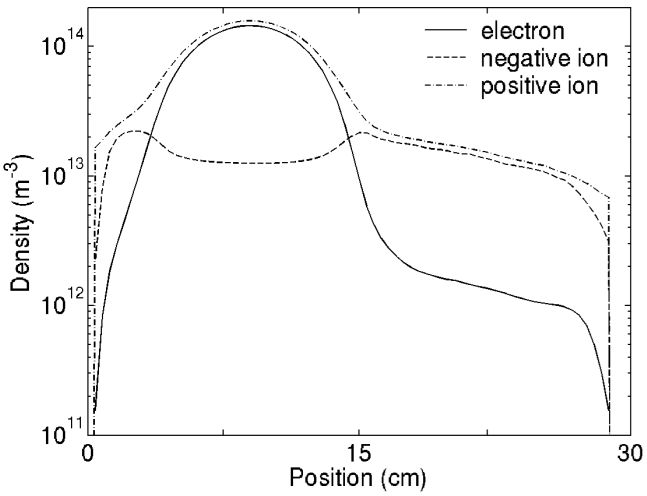

Figure 6.7: Steady-state density profiles of a stable double layer.

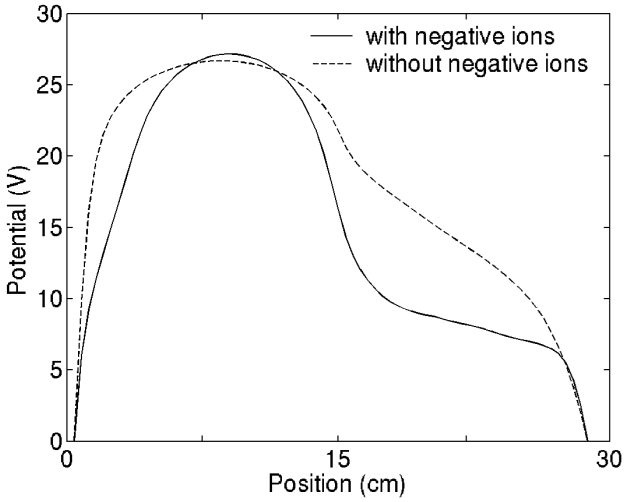

Figure 6.8: Steady-state plasma potential profile of a stable electronegative double layer (solid line) and of an electropositive plasma (dashed line) for the same parameters.

the formation of the double layer.

In Plihon's experiment, the electron temperature and densities are such that the recombination source term is less, but of the order of the ionization source term. However, with the present 2D model, simulations of such densities would be extremely time consuming. Densities between 10^{14} and 10^{15} m^{-3} is the best that could be achieved in a reasonable amount of time. For these low density simulations, recombination with a realistic recombination rate (of the order of 10^{-13} m^3s^{-1}) is negligible compared to ionization. Hence, the recombination rate was artificially increased to make it significant compared to ionization. In this case only, a double layer was formed, suggesting that a double layer can only appear when losses in volume are significant.

In summary, double layers could be formed by carefully adjusting ionization, attachment and recombination rates. In the simulation, electronegative double layers form when the three following conditions are met: i) high downstream electronegativity ii) obtained with high attachment and high recombination rates, rather than low attachment and low recombination (in which case no double layer forms). iii) Finally, the source should be ionization-dominated, while the diffusion chamber should be attachment-dominated.

The influence of various parameters, such as the relative positive to negative ion masses, the presence of a dielectric in the source (as in Plihon's experiment), the shape of the ionization and attachment frequency profiles etc. was investigated. It was found that the double layer was not much affected as long as the basic feature ionization-dominated source and attachment-dominated diffusion chamber was satisfied.

As already pointed out, the 2D model has a number of weaknesses: i) high densities cannot be simulated in a reasonable amount of time, ii) consequently double layers were found for only unphysical large recombination rates iii) and the model is not self-consistent. In the next section, a self-consistent simulation is described to provide better insight into the physical mechanisms and reveal some of the critical parameters.

6.4 The model *h2x* applied to electronegative plasmas

6.4.1 Model

The simulation of electronegative double layers and more particularly the simulation of propagating double layers is rather challenging; the challenge arises from various things such as the rather high plasma densities, the disparity between the negative ion and electron densities, the large time-scale oscillations, the necessity of self-consistency etc.

In this section, the model *h2x* presented in Chapter 5 is modified to handle electronegative discharges. A very simplified mixture of argon and SF_6 is to be simulated and, as in the previous section, in addition to ionization, the model accounts for the various reactions such as attachment and recombination. Only one type of negative ion with the same mass as the argon positive ion and with

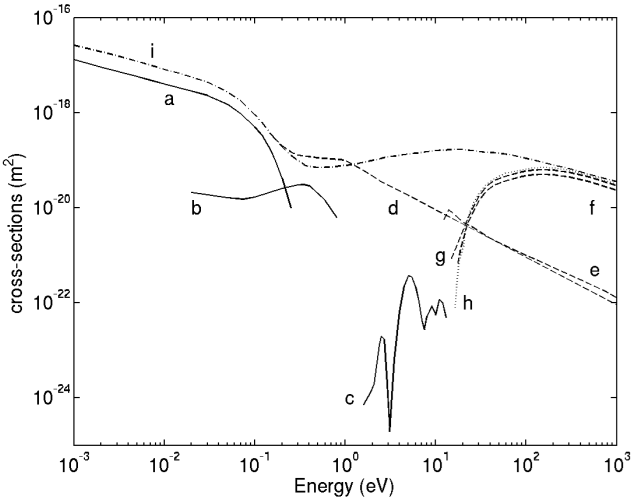

Figure 6.9: Electron-neutral collision cross-section with SF_6; (a), (b) and (c) attachment; (d), (e), (f) and (g) attachment; (h) ionization; (i) elastic collisions.

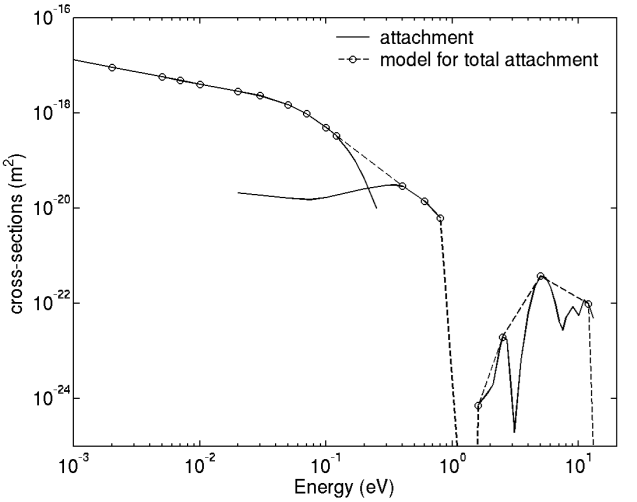

Figure 6.10: Attachment cross-section in SF_6 (solid lines) and simplified total attachment cross-section used in the 1D simulation (broken line)

Table 6.2: General parameters of the 1D simulation of spontaneous formation of propagating double layers. These parameters were used in the present investigation, unless stated otherwise.

Quantity	Value
system length	28 cm
cell number	70
total duration	10-100 ms
hybrid time step	5×10^{-8} s
Monte Carlo time step	5×10^{-10} s
macro-particle weight	1×10^{14} m^{-3}
positive and negative ion mass (Ar)	6.68×10^{-26} kg
positive and negative ion charge	$+e$ and $-e$
room temperature	297 K
source term	4×10^{21} m^{-3}s^{-1}
total neutral pressure	1 mTorr
K_{rec}	10^{-13} m^{3}s^{-1}
"virtual radius" [a]	10 cm (uniform)

[a] See Chapter 5 for the nomenclature "virtual radius".

an opposite charge $-e$ is considered.

The attachment source term profile is handled in the same way as the ionization source term profile described in Chapter 5, i.e. by the Monte Carlo sub-model. Simplified attachment cross-sections based on that of SF_6 compiled by Pitchford et al. were used. Figure 6.9 shows the electron-neutral collision cross-sections in SF_6, including elastic collisions (i), ionization (h), excitation (d,e,f and g) and attachment (a,b and c). Figure 6.10 shows the attachment cross-sections in SF_6 and the simplified attachment cross-sections that were used for the present simulations. In addition to undergoing collisions with argon neutral atoms, electrons can also undergo collisions with neutral SF_6; the cross-section corresponding to these collisions is shown by line (i) in figure 6.9. The other exciting and ionizing collisions with SF_6 are not considered. In the following, the simplified electronegative background gas is loosely called SF_6.

Recombination events are modeled in the same way as in the 2D model presented previously (Section 6.3). The recombination source term profile involves a recombination rate K_{rec} and the respective densities of negative and positive ions. Positive and negative ions undergo elastic and charge-exchange collisions with neutrals, with the same cross-section as argon.

6.4.2 Fully self-consistent electronegative double-layer simulation

Using the model above, with the general parameters given in table 6.2 and a relative SF_6 concentration of 15%, a high-density plasma sustaining spontaneous propagating double layers was self-consistently simulated.

Figure 6.11(a) shows a snapshot of the plasma potential profile as a function

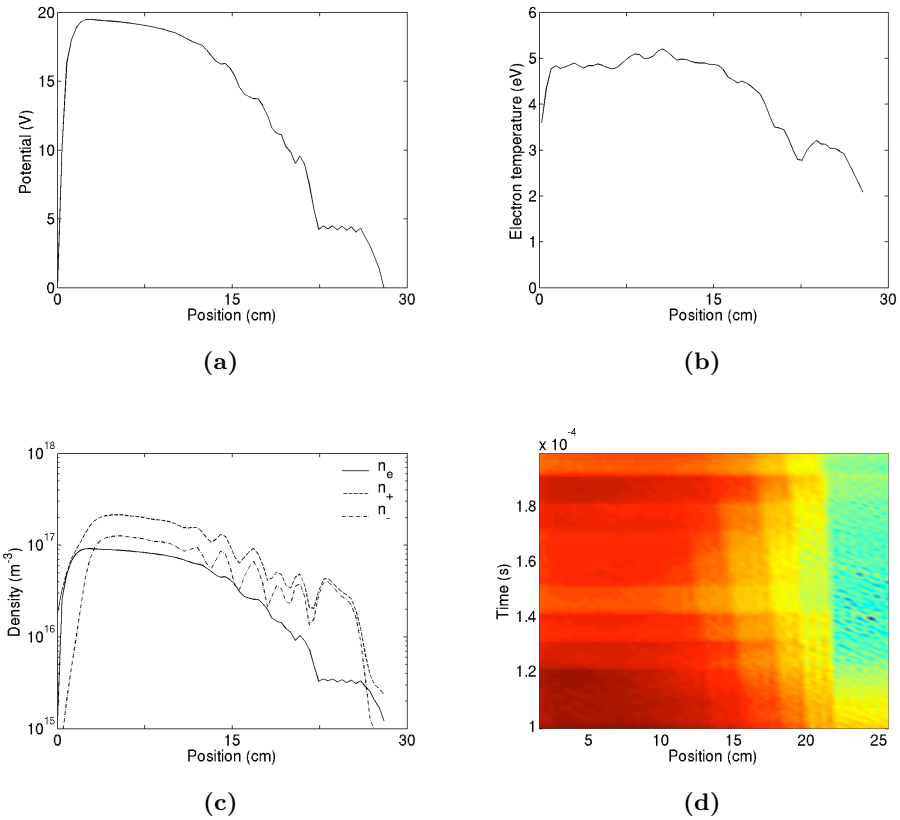

Figure 6.11: Self-consistent spontaneous formation of propagating double layers in an electronegative discharge. (a) Snapshot of the plasma potential profile presenting a clear drop of ~ 5 V; (b) snapshot of the corresponding electron temperature profile, also presenting a drop; (c) snapshot of the electron (solid line), positive ion (dashed line) and negative ion (dotted-dashed line) density profiles; (d) plasma potential as a function of space and time when the electronegative propagating double layers are formed.

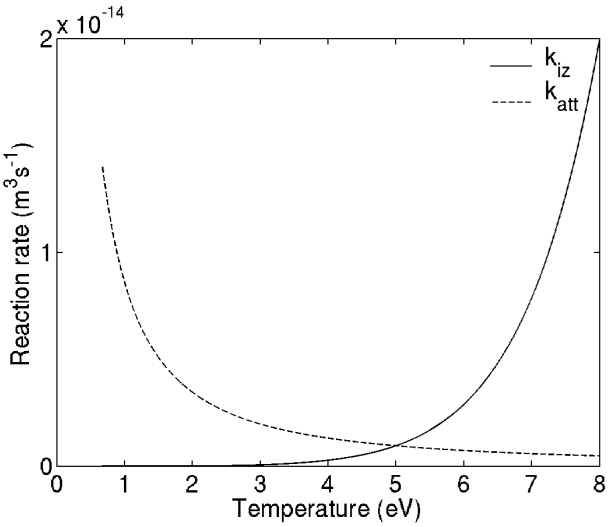

Figure 6.12: Reaction rate coefficients for ionization (solid line) and attachment (dashed line) as a function of electron temperature. The ionization rate coefficients were obtained by integrating the ionization cross-section of argon over a Maxwellian distribution truncated above 20 eV to account for the depletion of eedf above the plasma potential.

of position; in addition to the smooth decrease of the potential from the source to the diffusion chamber, a series of potential "steps" and a clear potential drop of ~ 5 V are observed in the downstream region. This sudden potential drop is extremely sharp and occurs within ~ 1 cm. Figure 6.11(b) shows that the potential drop is accompanied by an electron temperature drop; the high and low-potential side temperatures are ~ 5 eV and ~ 3.5 eV, respectively, which is surprisingly close to that experimentally measured by Plihon et al. (2005a).

Figure 6.11(c) shows the electron (solid line), positive (dashed line) and negative (dotted-dashed line) ion densities. A series of spatial oscillations in both positive and negative ion densities are observed on the downstream side. These oscillations are successive regions of rarefaction of positive and negative ions. Each of the ion density local minima correspond to a plasma potential "step" [figure 6.11(a)]. The electronegativity α is around 1 in the source region and as high as ~ 8 between two successive double layers.

Finally, figure 6.11(d) shows the plasma potential resolved in space (horizontal axis) and time (vertical axis). Five potential fronts, corresponding to five double layers are observed and are propagating towards the source region. A time-resolved analysis of the densities also shows that the spatial oscillations mentioned before propagate towards the source region, following the potential drops.

6.4.3 Parametric study of electronegative double layers

In the previous section, it was shown that the spontaneous formation of propagating double layers in an electronegative plasma by the use of a full self-consistent simulation was possible. In the present section, a parametric investi-

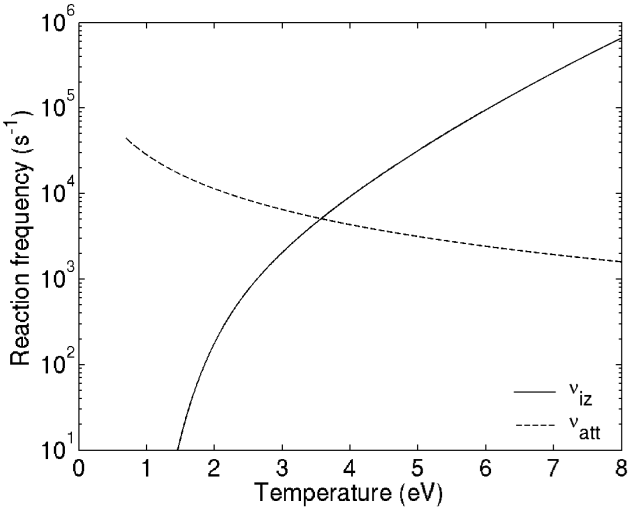

Figure 6.13: Reaction frequencies corresponding to the rate coefficients given in figure 6.12, for a neutral pressure of 1 mTorr.

gation of the spontaneous propagating double layers is presented. For the sake of simplicity, rather than coupling the two sub-models as was previously done, a temperature profile similar to that obtained self-consistently is now used as a *parameter* of the simulations (the electron Monte Carlo is deactivated). Figure 6.12 shows the ionization (solid line) and the attachment (dashed line) reaction rate fits[1] as a function of the electron temperature. Figure 6.13 shows the corresponding reaction frequencies for a neutral pressure of 1 mTorr.

The temperature profile used in the following decreases from 4.5 eV in the source to 3 eV in the diffusion chamber, following an arctan profile. The temperature drop is located at 15 cm and is constant in time.

The effect of almost every parameter such as the positive and negative ion masses, the concentration of SF_6, the "virtual radius", the temperature profile etc. was investigated; the most relevant are reported here. Note that the spatial resolution of the grid and the simulation time step were varied without significantly affecting the results.

Double layers form at low pressure with high attachment and recombination

Electronegativity: figure 6.14(a) shows a spatio-temporal representation of the plasma potential profiles and figure 6.14(b) shows snapshots of the plasma potential profiles as a function of space for various concentrations of SF_6. Propagating double layers do not form unless the relative concentration of SF_6 is

[1] Reaction rate coefficients k can generally be well fitted by a generalized Arrhenius function of the energy $\mathcal{E}$, of the form $k(\mathcal{E}) = \exp(a + b\ln\mathcal{E} + c/\mathcal{E} + d/\mathcal{E}^2 + e/\mathcal{E}^3)$. Note however that ionization may be more or less closely related to the electron temperature, as ionization is essentially controlled by the tail of the distribution which does not necessarily reflect the bulk electron distribution.

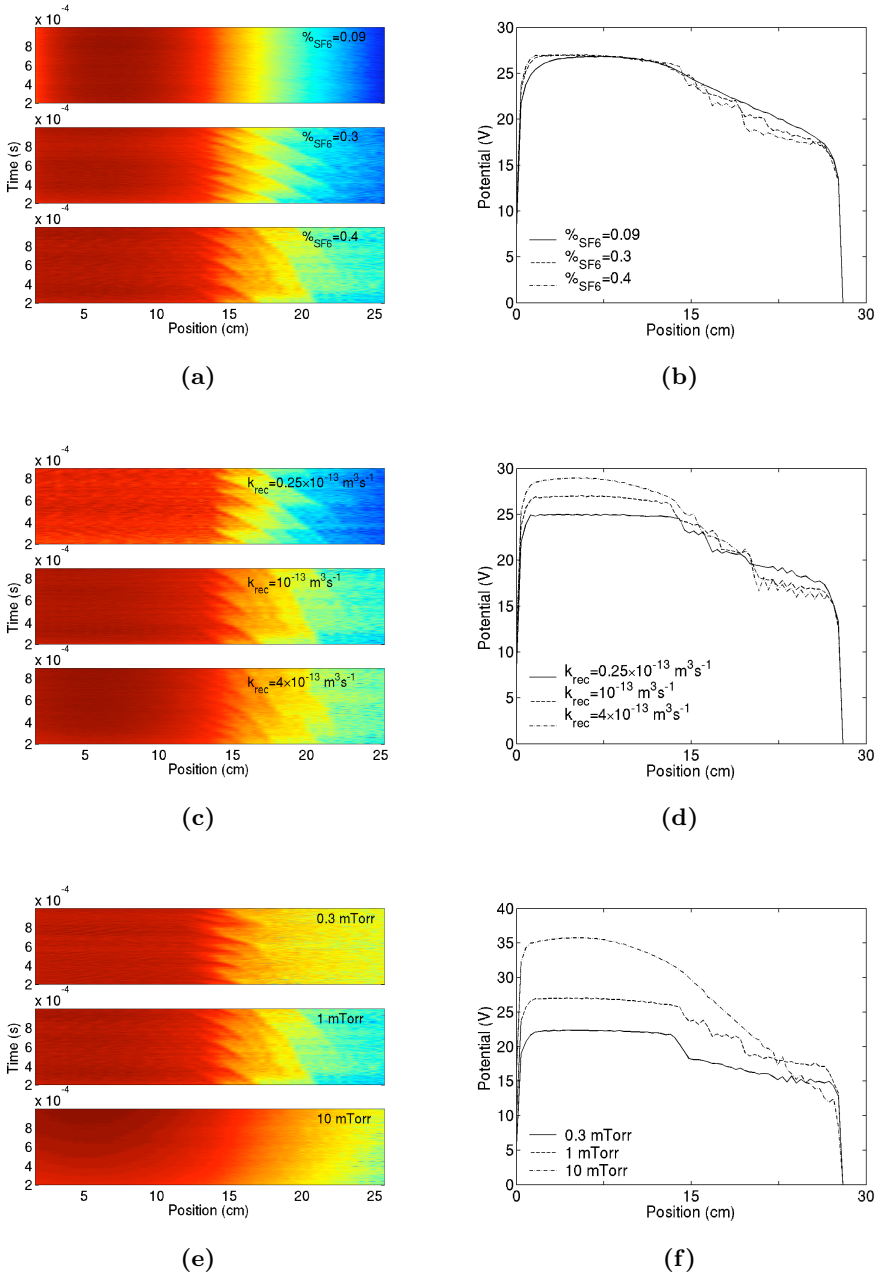

Figure 6.14: Contour-plots of the plasma potential profiles as a function of space and time, and snapshots of the plasma potential profiles, for various relative concentrations of SF_6 [(a) and (b)], recombination rate coefficients [(c) and (d)], and neutral gas pressures [(e) and (f)].

sufficiently large ($\gtrsim 30\%$ under the present conditions), confirming that a minimal electronegativity is required.

Eedf: when the *real* eedf was calculated by the simulation (Section 6.4.2), the minimal relative concentration of SF_6 required for the formation of propagating double layers (i.e. to reach sufficient electronegativity) was $\sim 15\%$. In the present case, when the eedf is assumed to be Maxwellian, almost twice this concentration ($\gtrsim 30\%$) is required to observe the propagating double layers. A reason for this is presumably that the eedf calculated by the Monte Carlo sub-model was not Maxwellian and was presenting a low-energy population favoring attachment to ionization, leading to sufficient electronegativity for the formation of propagating double layers. This low-energy population of electrons is not captured when assuming Maxwell-Boltzmann electrons. Thus, the concentration of SF_6 has to be increased accordingly in order to reach sufficient electronegativity, compatible with the double layers. This provides evidence supporting the fact that the eedf is a rather important parameter in the formation of electronegative double layers.

Potential drop: the second consequence of assuming Boltzmann electrons, is that there is no net electron flux associated with the double layer. In reality (experimentally or with particle electrons in the simulation) downstream electrons may be accelerated through the double layer towards the high-potential side. This may increase the upstream electron temperature and therefore enhance the potential drop of the double layer (for example by "boosting" the ionization on the high-potential side). This may explain the fact that the potential drops associated with the double layers observed here (where Boltzmann electrons are assumed) are between 1 V and 2 V, rather than the 5 V observed with the full self-consistent simulations, where the eedf was calculated. Also, it should be mentioned that although the temperature drop is positioned at 15 cm, the double layers propagate, irrespective of the temperature drop position, suggesting that the temperature drop observed in Section 6.4.2 was a consequence of the double-layer potential drop rather than the opposite. The point of these two remarks is that it seems that "something" creates the double layer, the double layer then generates a temperature drop and the temperature drop enhances the original potential drop.

Recombination rate: figure 6.14(c) shows the plasma potential profiles as a function of space and time while figure 6.14(d) shows snapshots of the plasma potential profiles as a function of space for various recombination rate coefficients K_{rec}. The electronegativity is maintained constant by changing the relative concentration of SF_6 accordingly. For the range of K_{rec} investigated, the double-layer potential drop increases with K_{rec}. In other words, for similar electronegativities, propagating double layers are only observed for sufficiently high attachment and recombination. This is in good agreement with what was concluded in Section 6.3 and also with previously simulated electronegative double layers (Sheridan et al. 1999b, Chabert and Sheridan 2000).

Pressure: finally, the total neutral gas pressure was varied from 0.1 to 10 mTorr, keeping the relative concentrations of argon and SF_6 constant. Figures 6.14(e) and 6.14(f) show that above a critical pressure ($\gtrsim 5$ mTorr) no double layer was formed.

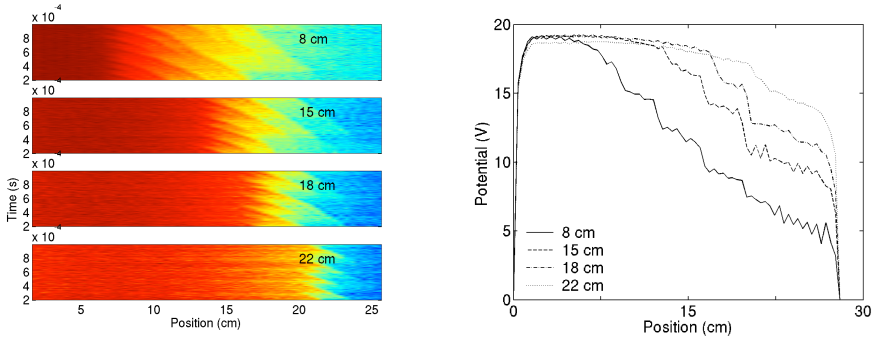

(a) **(b)**

Figure 6.15: (a) Contour-plots of the plasma potential profiles as a function of space and time, and (b) snapshots of the plasma potential profiles, for various temperature drop positions.

Small-diameter and long chambers are propitious to the formation of double layers

Chamber diameter: electron radial losses have presumably two main effects. The first and most obvious, observed under the present conditions of pressure (low pressure) is a depletion of the electron energy distribution function at energies higher than the plasma potential (Chapter 4). In response, the electron temperature tends to increase to "boost" the ionization, to counterbalance the radial losses and maintain the plasma.

The second effect of the electron radial losses, somewhat related to the first one, appears in particular when radial losses are combined with a localized heating mechanism. In such a case the electron temperature may increase more in the heating region than in the rest of the discharge, hence possibly leading to a non-uniformity of the electron temperature, with a higher temperature in the source than in the diffusion chamber. This phenomenon, observed irrespective of any geometric transition, is particularly propitious to the formation of electronegative double layers where the source (diffusion chamber) should be ionization-dominated (attachment-dominated), requiring a sufficiently high (low) electron temperature, favoring ionization to attachment (attachment to ionization). In addition, as mentioned in Chapter 5, ion radial losses tend to enhance asymmetries in the system.

Geometric transition: The radial losses of particles is rather important for the formation of electronegative double layers, as they really affect the eedf previously shown to be a fundamental parameter. However, the geometric transition between the source region and the diffusion chamber does not seem to be a fundamental parameter in both the experiment (Plihon et al. 2005b) and the simulation, as in both cases it was possible to form double layers without a geometric transition.

Chamber length: changing the position of the temperature drop in the temperature profile is a way of changing the relative length of the "source" and

"diffusion chamber" in the simulation. Figure 6.15(a) shows the plasma potential profiles as a function of space and time while figure 6.15(b) presents snapshots of the plasma potential profiles as a function of space for various positions of the temperature drop. Increasing the relative length of the diffusion chamber leads to an increase in the number of propagating double layers simultaneously present in the system. On the contrary, reducing the size of the diffusion chamber leads to a decrease of the number of propagating double layers. When the diffusion chamber length is sufficiently decreased, no propagating double layer forms.

Characterization of the propagating double layers

Direction of propagation: figure 6.16 shows various characteristics of typical propagating double layers for an SF_6 concentration of 40%. Figure 6.16(a) is a 3D mapping of the plasma potential as a function of time and space. Although the present double layers propagate in the opposite direction, they appear to be a phenomenon very similar to that observed by Plihon et al. (2005b) (figure 6.4, p. 110), as discussed later.

Velocity of propagation: figure 6.16(b) is a contour-plot over 10 ms of the plasma potential profile. As can be observed, the double layers always form at the same critical position and propagate towards the source at $\sim$ 100 m/s. Note that the simulation was run up to 100 ms without any major variation.

Electronegativity: figures 6.16(c) and 6.16(d) are snapshots of the plasma potential and the electron, positive and negative ion densities. At the position of each double layer, a region of positive and negative ion rarefaction can be observed. Figure 6.16(e) shows a snapshot of the electronegativity $\alpha = n_-/n_e$ at the same instant and the electronegativity is minimal at the positions of the double layers, but maximal immediately downstream. The regions of high electronegativity are trapped between two successive double layers, and are pushed towards the source by the moving double layers.

Source term profiles: figure 6.16(f) shows the ionization (solid line), attachment (dashed line) and recombination (dotted-dashed) source term profiles. The source is ionization-dominated, while the diffusion chamber is attachment-dominated. The recombination takes place mostly in the source, but also in the high-electronegativity regions, where the ion densities are maximum.

Frequency: figure 6.17 shows a low-frequency activity around 2-4 kHz in the downstream plasma. This activity corresponds to the train of propagating double layers born at some critical downstream position and propagating towards the source. In the range of pressures investigated, the frequency of the propagating double layers was found to be weakly dependent on the neutral gas pressure.

Bohm criterion: figure 6.18 shows a snapshot of the positive and negative ion average velocities, v_+ and $-v_-$. The ion sound speed (or Bohm velocity) in electronegative plasmas is given by equation 6.1. The average downstream ion sound speed is shown by the horizontal line. At the positions of the propagating double layers, shown by the vertical lines, both positive and negative ions reach the sound speed before entering the double layers from the high and low-

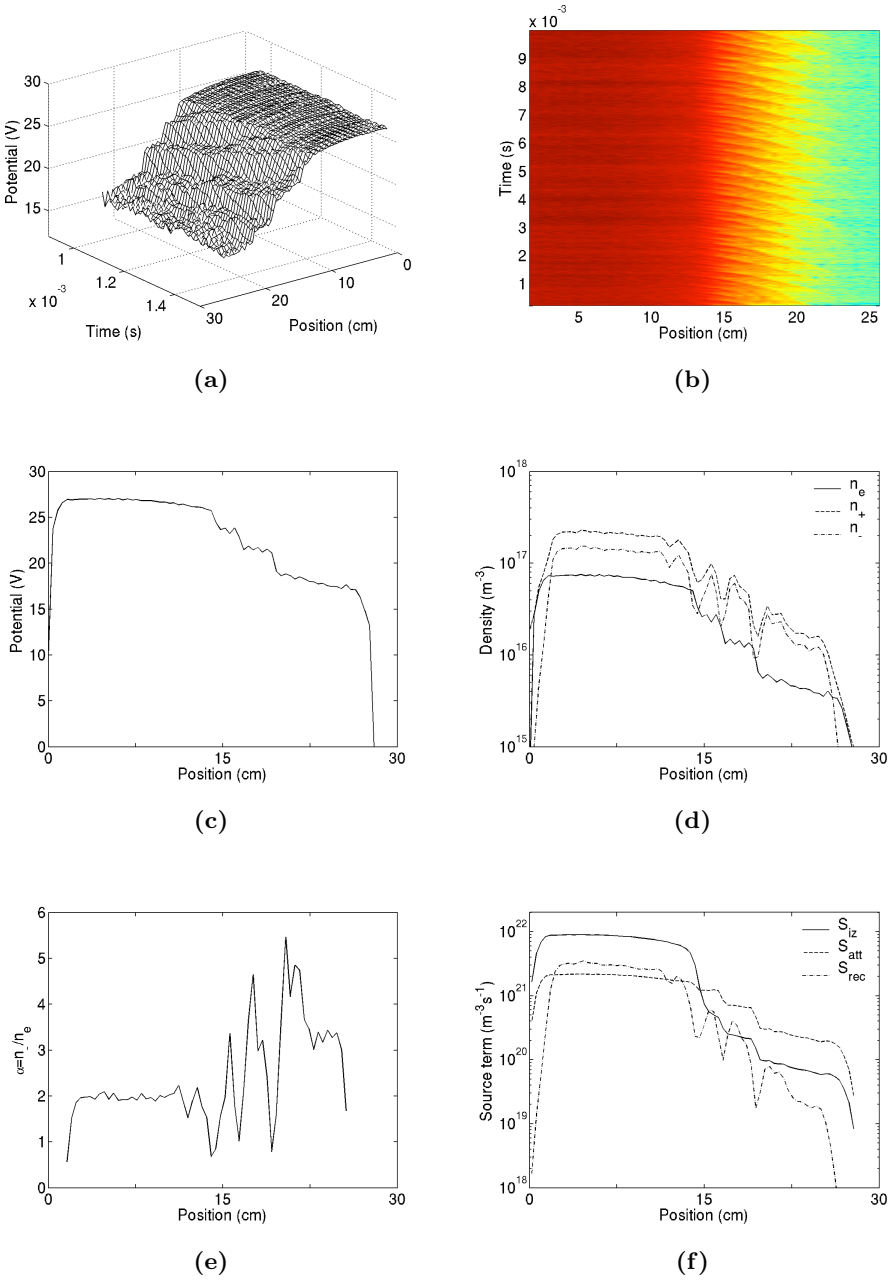

Figure 6.16: Propagating double layers in an Ar/SF_6 mixture, with an SF_6 relative concentration of 40% at 1 mTorr. (a) 3D mapping of the plasma potential profile as a function of space and time; (b) contour-plot of the plasma potential profile as a function of space and time, increased brightness indicates decreased potential; (c) snapshot of the plasma potential profile showing successive double layers, propagating from the diffusion chamber (right) to the source (left); (d) snapshots of the electron (solid line), positive (dashed line) and negative (dotted-dashed line) ion density profiles; (e) snapshot of the electronegativity $\alpha = n_-/n_e$ profile; (f) snapshots of ionization (solid line), attachment (dashed line) and recombination (dotted-dashed line) source term profiles.

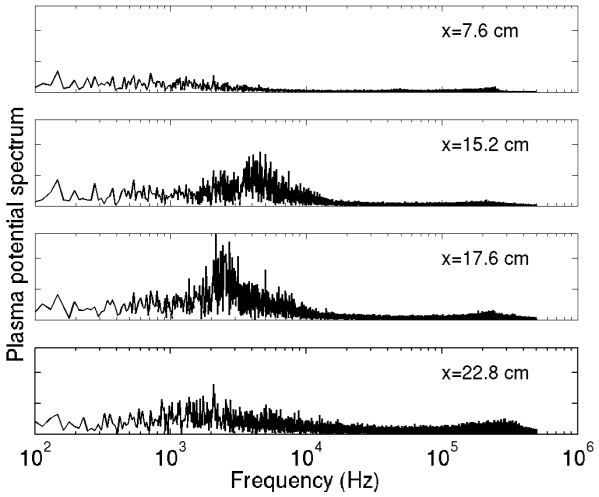

Figure 6.17: Frequency spectrum of the plasma potential at various positions in the system. For positions on the right-hand side of the temperature transition ($x > 15$ cm), a 2-4 kHz activity is observed.

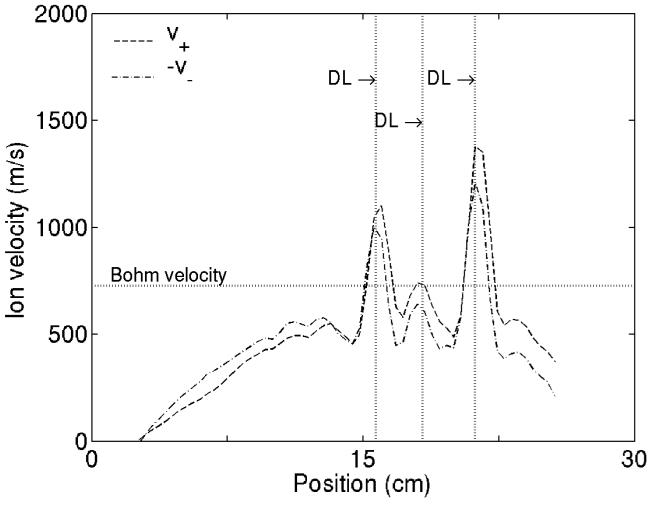

Figure 6.18: Snapshot of the positive and negative ion average velocities, v_+ and $-v_-$, as a function of position (broken lines). The vertical dotted lines show the positions of the double layers, while the horizontal line shows the Bohm velocity.

Table 6.3: (a) Plihon's propagating double layers (b) and propagating double layers reported in the present thesis.

Parameters	(a) Plihon's DL	(b) Simulated DLs
$\%_{SF_6}$	13-25%	15%[a]
K_{rec}	not a parameter	critical[b]
P[c]	$\sim$ 5 mTorr	$\sim$ 5 mTorr
Geometric transition	not critical	not critical
Small diameter	?	critical[d]
Chamber length	critical[e]	critical[e]
Properties	**(a) Plihon's DL**	**(b) Simulated DLs**
Frequency	$\sim$ kHz	$\sim$ 2 kHz
Velocity	150 m/s	100 m/s
Direction	$\rightarrow$	$\leftarrow$
α[f]	$\sim 5 \pm 40\%$	4-6
Potential drop	7 V[g]	5 V[h]
T_{up}/T_{down}	5/3.5 eV[i]	5/3.5 eV
Bohm criterion[j]	?	satisfied

[a] Minimal concentration allowing the formation of double layers in the simulation. 15% with fully self-consistent model; 30% when Boltzmann electrons are assumed.

[b] The simulation showed that DLs were formed only for sufficiently large recombination rate. DLs were observed in the simulation for realistic recombination rates ($K_{rec} = 10^{-13}$ m^3s^{-1}).

[c] Pressure P above which no double layer was formed.

[d] No double layer observed for large-diameter chambers.

[e] Sufficiently short diffusion chambers prevent the formation of double layers.

[f] Maximum of the electronegativity α obtained just downstream of the double layers. Measured via photo-detachment for Plihon's values (Plihon 2006).

[g] 7 V at the potential discontinuity, almost 10 V in total.

[h] 5 V with the fully self-consistent model, 1 V when Boltzmann electrons are assumed.

[i] Temperatures reported for the stable double layer.

[j] Bohm criterion for positive and negative ions.

potential sides, respectively. The ions are then accelerated through the double layers up to approximatively twice the sound speed.

6.5 Discussion and conclusion

Plihon et al. (2005b) have experimentally characterized the propagating double layers and fully determined the window of parameters, such as the neutral gas pressure, the relative concentration of SF_6, the input power etc. for which they form. The self-consistent simulation has allowed the spontaneous formation of propagating double layers that were shown to be a very similar phenomenon to that of Plihon et al. (2005b). The main features of the propagating double layers observed by Plihon et al. (2005b) and of those reported in the present thesis are summarized in table 6.3. Despite the fact that these propagating double layers

do not propagate in the same direction, they have many properties in common, such as their velocity of propagation, frequency, electronegativity, temperature drop etc. Also, they appear under the very similar conditions, such as neutral gas pressure, relative SF_6 concentration etc.

Hence, the simulation gave evidence supporting the observation that double layers may spontaneously form in electronegative plasmas. i) To observe this, both the experiment and the simulation have shown that a lower limit to the electronegativity is required, which is achieved thank to a sufficient relative concentration of SF_6 and sufficient attachment. ii) The losses in volume of both positive and negative ions via recombination also appear to be crucial. The simulation showed that below a critical recombination rate, no double layer could be formed. iii) The simulation also confirmed that the geometry of the chamber, i.e. a change in diameter, does not seem to be a critical parameter. iv) However, the diameter itself is crucial, since it can dramatically change the electron energy distribution function that controls the attachment and therefore the electronegativity. v) The simulation showed that for chambers below a certain length, no double layer could be sustained, which is in good agreement with the experimental observations. This may well be because positive and negative charges need to develop a sufficient relative drift velocity, which can be achieved only in sufficiently long chambers. vi) Finally the neutral gas pressure is also a fundamental parameter, as no double layer was observed for pressure above ~ 5 mTorr.

As a concluding remark, it may be noted that Plihon et al. (2005b) had compared their propagating double layers with the downstream instability reported by Tuszewski et al. (2003), Tuszewski and White (2003) and Tuszewski and Gary (2003), as they were a very similar phenomenon. Although they have not explicitly measured a double layer, Tuszewski et al. (2003) have observed that the plasma immediately downstream of the critical position, where the downstream instability seems to be born, was transiently electropositive, suggesting the existence of an internal sheath, i.e. a double layer. The double layers obtained with the simulation were also very similar to that observed by Tuszewski et al. (2003). The exact relationship between these three phenomena should be investigated further in future.

Chapter 7

Conclusion

Electron or ion beams have many applications ranging from plasma processing to electric propulsion for space applications etc. In plasma processing, electron or ion beams are used to functionalize and modify surfaces for applications such as microelectronics and bio-physics. In electric propulsion, the creation of an ion flux provides thrust for the spacecraft Hence, the acceleration of charged particles (electrons or ions) and understanding the mechanisms that can create and maintain electric fields in plasmas is of particular interest. An interesting and promising mechanism is the electric double layer, which is an electrostatic phenomenon where a large electric field is contained between two opposite space charge layers.

Traditionally, the understanding of physical phenomena, such as electric double layers, is obtained by combining experimental observation with a subsequent development of theoretical models. Gaining insight into complex discharge phenomena became possible as a result of advances in modern computer techniques and the use of computer simulations. As distinct from experiments where a limited number of quantities can be measured, numerical simulations provide direct access to most of the important parameters of the system under investigation. As numerical models can only accommodate a limited number of hypotheses, they are best used in conjunction with laboratory experiments. Hence experiment and simulation, together, provide an excellent way to understand the mechanisms underlying complex gas discharges.

The primary concern of this thesis was the development of numerical models to investigate the basic physics underlying and accompanying two distinct types of electric double layers in plasmas. In the first part of this thesis a simplified numerical simulation of double layers in current-free plasmas was presented, while in the second part, a self-consistent simulation confirmed earlier experimental results demonstrating the spontaneous formation of propagating double layers in electronegative plasmas.

7.1 Inductive plasma simulation and current-free double layer

Inductive plasmas were simulated by using a one-dimensional particle-in-cell simulation including Monte Carlo collision techniques. To mimic the inductive heating, a non-uniform rf electric field, perpendicular to the electron motion was included into the classical particle-in-cell scheme. The system constituted by the particle-in-cell scheme and the additional rf electric field was investigated. It was shown that this heating mechanism allows to sustain plasmas, without introducing any pathological features in the plasma potential or the electron transport. An analytical model describing a similar situation was developed. This analytical model showed that significant stochastic heating may arise from such a non-uniform electric field perpendicular to the electron motion.

The first type of double layers investigated is that of Charles and Boswell (2003) that form at the interface of the source and the diffusion chamber in a current-free plasma expanding along the lines of a diverging magnetic field. The investigation of current-free double layers is of particular relevance in various space plasma phenomena as their existence would, for example, free theoreticians of the need to find a current closure condition. Also, the existence of an ion beam associated with the current-free double layer may lead to various applications. For example, because the double layer is completely current free, the electron and ion fluxes across the double layer are equal, which is of great interest for space propulsion, and plasma acceleration in general, as there is no need to neutralize the ion beam providing the thrust.

The Monte Carlo collisions / particle-in-cell simulation including the perpendicular heating mechanism shows that double layers can be sustained by one-dimensional current-free plasmas. This adds a new phenomenon to those simulated in the last few decades where the double layers were always associated with applied potential difference or by drawing a current through the system.

The spatial structure, beam energy, character of the ion acceleration region, and ion heating in the presheath of the current-free double layer predicted with the simulation were all consistent with the LIF (Laser-Induced Fluorescence) measurements that were subsequently performed. Both the simulation and the experiment have shown the formation of a super-sonic ion beam resulting from ions accelerated through the double-layer potential drop.

The simulation also gave an excellent opportunity to investigate the electron transport in double-layer plasmas. Confirming earlier experimental results, the simulation showed that when the electron energy relaxation length is greater than the system dimension, electrons lost to the walls are the main mechanism for the high-energy depletion of the eedf.

In the laboratory (and space) experiments there is the added complication of an axial expanding magnetic field. By using a simple algorithm that converts the perpendicular energy into parallel energy in the direction of the magnetic expansion, the simulation showed that the magnetic force may play a significant role in the formation of the current-free double layer. The role of the geometric and magnetic expansion needs to be investigated further in future.

7.2 Self-consistent hybrid model and electronegative double layer

The second part of this thesis shows that classical hybrid simulations, where ions are treated as particles and electrons are assumed to have a Maxwell-Boltzmann distribution may lead to a miscalculation of the plasma potential. As an alternative to the fully self-consistent, computationally-expensive, particle-in-cell simulations, a novel hybrid simulation was proposed and shown to be in much better agreement with the full particle-in-cell simulation than the classical non self-consistent hybrid model.

This "improved" hybrid model was used to simulate electronegative plasmas under the same conditions as Plihon et al. (2005b). Under these conditions, propagating double layers were observed and provided evidence supporting the notion that double layers may spontaneously form in electronegative plasmas. The propagating double layers observed in the simulation share many common features with those of Plihon et al. (2005b). Thus, it was possible to show that critical parameters of the simulation were very much aligned with the critical parameters of the experiment allowing a more enlightened approach to the investigations both numerically and experimentally.

During the course of this work, a number of interesting phenomena related to double layers were observed but not investigated in depth, hence opening doors to new areas of research. For example, the role played by the magnetic force in the formation of the current-free double layer, or the exact nature of the propagating double layers observed in electronegative discharges. It would be extremely interesting to investigate these phenomena in depth in future work.

Chapter 8

Appendix

8.1 Trigonometric identities and transcendental integrals

$$\begin{array}{lcl} < \sin(a-\phi)\cos(b-\phi) >_\phi & = & \frac{1}{2}\sin(a-b) \\ < \sin(a-\phi)\sin(b-\phi) >_\phi & = & \frac{1}{2}\cos(a-b) \\ < \cos(a-\phi)\cos(b-\phi) >_\phi & = & \frac{1}{2}\cos(a-b). \end{array} \tag{8.1}$$

$$\int_0^\infty \exp(-\nu t)\sin(\omega t)\, dt = \frac{1/\omega}{1+(\nu/\omega)^2}. \tag{8.2}$$

8.2 Electron density in a Monte Carlo simulation

In the general case of a classical Monte Carlo model where a certain number N_s of sample electrons are followed one by one from their creation to the end of their life, the electron density in a cell is given by

$$n_{\text{cell}} = \frac{t_{\text{res,cell}} \iiint_{\mathcal{V}} S_{\text{iz}}\, \mathrm{d}\mathcal{V}}{\mathcal{V}_{\text{cell}}}, \tag{8.3}$$

where $t_{\text{res,cell}}$ is the average time of residency per electron in a cell, i.e. the cumulative time spent by the N_s electrons in a certain cell over N_s. The other quantities are self-explanatory, $\mathcal{V}_{\text{cell}}$ is the cell volume, Δx for a 1D simulation and $\iiint_{\mathcal{V}} S_{\text{iz}}\, \mathrm{d}\mathcal{V}$ is the integral of the real ionization source term over the whole volume, $S_{\text{iz}}\mathcal{L}$ for a 1D simulation of length $\mathcal{L}$.

For the model *h2x*, N_s new electrons are injected in the Monte Carlo at each communication time in addition to those that were already present from the previous iteration. One might therefore expect a formula different from equation 8.3; this is not the case. The number of sample electrons in the Monte Carlo is still N_s, the other electrons, already present in the simulation from the previous iteration, represent the "future life" of these new N_s electrons if their whole life were simulated, and not only the first instants of their life during two communication time steps. The electron density in the Monte Carlo sub-model

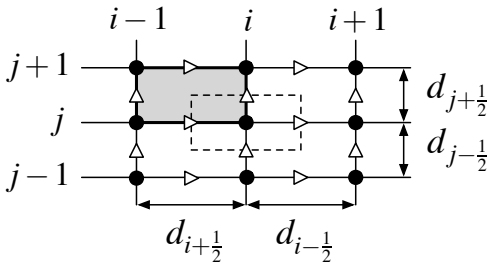

Figure 8.1: Two-dimensional mesh of the hybrid model: the nodes of the mesh, where the scalar quantities are calculated by default, are indicated by the black dots. Cells are defined by four nodes (grey square); they are used to defined the geometry of the domain. A so-called control volume is defined around each node, as represented by the dashed square. The vectorial quantities are defined on the different faces of a control volume, in between two nodes; this is represented by the white triangles, ▷ and △, for the vector along the x and r directions, respectively.

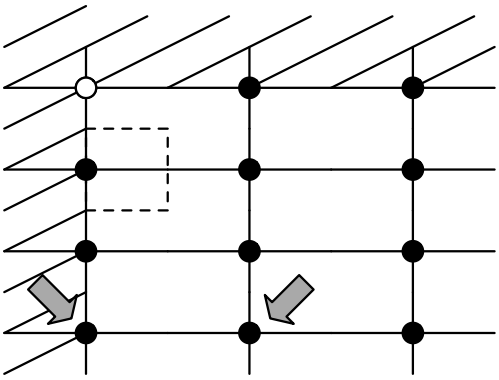

Figure 8.2: This schematic shows that the wall control volumes, represented by the dashed square, are half sized, and that they are null outside the plasma. Finally, the grey arrows represent the allocation of such or such material of a cell to a node; the four corners of a cell "electrode" are "electrode", while for other materials (plasma or dielectric), the material of the cell is allocated to its bottom-left-hand corner.

of the model *h2x* is thus given by equation 8.3, but were $t_{\text{res,cell}}$ represents the cumulative time spent by all the electrons ("old" and "new") electrons in a certain cell during two communication time steps divided by the number N_s of sample electrons.

8.3 Spatial discretization of Poisson's equation

Equations solved in the present model are the same as that of Chapter 5, namely Poisson's equation coupled to the Boltzmann relation. The time discretization has been thoroughly explained previously, so here the focus is put on the spatial discretization. In the following, terms such as cells, nodes, control volumes etc. are used, this nomenclature is defined in figure 8.1. The model assumes a cylindrical symmetry and equations are solved on a 2D mesh defined by the directions x and r, which is taken to be linear in x and r^2 (the distance

between two nodes of the grid goes as $\sqrt{r}$). The choice of such a grid allows cells representing the same volume irrespective of their x and r position, and therefore to have a uniform particle density described by a uniform macro-particle number per cell.

The grid is composed of N_x (resp. N_r) cells and $N_x + 1$ (resp. $N_r + 1$) nodes in the x (resp. r) direction. The index i (resp. j) refers to the x (resp. r) direction. The distance from the node (i, j) to its neighbors are defined on figure 8.1 and are called $d_{i+\frac{1}{2}}$, $d_{i-\frac{1}{2}}$, $d_{j+\frac{1}{2}}$, $d_{j-\frac{1}{2}}$. An arbitrary domain is defined by assigning a material and characteristics to each cell of the grid. The material can be either plasma, dielectric or electrode. The characteristics are, for example, the relative permitivity of the dielectric, the potential of an electrode etc. A node represents the same material and characteristics as the cell of which it is the bottom-left-hand corner, except if the cell is an electrode, in which case the four nodes of the cell are an electrode (this is represented by the grey arrows in figure 8.2).

A so-called control volume is defined around each node of the mesh that is in the plasma (figure 8.1). Each control volume $\mathcal{V}_i$ has four surfaces and they are called $\mathcal{S}_{i+\frac{1}{2},j}$, $\mathcal{S}_{i-\frac{1}{2},j}$, $\mathcal{S}_{i,j+\frac{1}{2}}$, $\mathcal{S}_{i,j-\frac{1}{2}}$. As shown in figure 8.2, the control volumes along the plasma boundaries are half sized. In the following, to lighten the notations, a quantity $Q_{i+\frac{1}{2},j}$ (resp. $Q_{i-\frac{1}{2},j}$, $Q_{i,j+\frac{1}{2}}$ and $Q_{i,j-\frac{1}{2}}$) will be represented either by this previous notation or by $Q^E_{i,j}$ (resp. $Q^W_{i,j}$, $Q^N_{i,j}$ and $Q^S_{i,j}$), where the upper index stands for *east* (resp. *west*, *north*, *south*).

Finally, unless stated otherwise, scalar quantities, such as the potential and the densities are calculated at the nodes (i, j), while vectorial quantities, such as the electric field are defined between two nodes $(i \pm \frac{1}{2}, j \pm \frac{1}{2})$. Poisson's equation is solved everywhere except in the electrodes.

As mentioned above, the Boltzmann relation is coupled to Poisson's equation to determined the electric field which depends on the space charge density ρ

$$\boldsymbol{\nabla} \cdot (\varepsilon \boldsymbol{E}) = -\nabla \cdot (\varepsilon \boldsymbol{\nabla} \Phi) = \rho, \tag{8.4}$$

where Φ is the potential and ε the dielectric constant. Rather than directly using the finite difference corresponding to Poisson's equation, the so-called control volume technique detailed below is used. This technique was originally developed for heat transfer and fluid flow calculations (Patankar 1980), the technique is used here to solve Poisson's equation for an arbitrary geometry and mesh, the system of coordinates being included in the control volumes. In order to discretize Poisson's equation, given by 8.4, it is integrated over the control volume of index i

$$\iiint_{\mathcal{V}_{i,j}} \boldsymbol{\nabla} \cdot (\varepsilon \boldsymbol{E}) \, \mathrm{d}\mathcal{V} = \iiint_{\mathcal{V}_{i,j}} \rho \, \mathrm{d}\mathcal{V} \Leftrightarrow \oiint_{\mathcal{S}_{i,j}} \varepsilon \boldsymbol{E} \cdot \mathrm{d}\boldsymbol{\mathcal{S}} = \rho_{i,j} \mathcal{V}_{i,j}, \tag{8.5}$$

which leads to

$$\varepsilon^E_{i,j} E^E_{i,j} \mathcal{S}^E_{i,j} + \varepsilon^W_{i,j} E^W_{i,j} \mathcal{S}^W_{i,j} + \varepsilon^N_{i,j} E^N_{i,j} \mathcal{S}^N_{i,j} + \varepsilon^S_{i,j} E^S_{i,j} \mathcal{S}^S_{i,j} = \rho_{i,j} \mathcal{V}_{i,j}. \tag{8.6}$$

Substituting the electric field in equation 8.6 yields, for example

$$E_{i,j}^{E} = -\frac{\Phi_{i+1,j} - \Phi_{i,j}}{d_i^E}, \tag{8.7}$$

a classical five-point equation is obtained

$$a_{i,j}^{C}\Phi_{i,j} + a_{i,j}^{E}\Phi_{i+1,j} + a_{i,j}^{W}\Phi_{i-1,j} + a_{i,j}^{N}\Phi_{i,j+1} + a_{i,j}^{S}\Phi_{i,j-1} = A_{i,j}, \tag{8.8}$$

where the east and central coefficients and right-hand side (rhs) of the equation are given by

$$a_{i,j}^{E} = -\frac{\varepsilon_{i,j}^{E}\mathcal{S}_{i,j}^{E}}{d_i^E}, \tag{8.9}$$

$$a_{i,j}^{C} = -(a_{i,j}^{E} + a_{i,j}^{W} + a_{i,j}^{N} + a_{i,j}^{S}), \tag{8.10}$$

and

$$A_{i,j} = \rho_{i,j}\mathcal{V}_{i,j}. \tag{8.11}$$

An expression similar to 8.9 exists for the west, north and south coefficients.

In Chapter 5, it was explained how to linearize the coupling of Poisson's equation and Boltzmann relation. The central coefficient and the rhs of the five-point equation above are modified according to equation 5.5 (Chapter 5) to account for the time linearization

$$\tilde{a}_{i,j}^{C} = a_{i,j}^{C} + \frac{\mathcal{V}_{i,j}}{\lambda_{i,j}^2}, \tag{8.12}$$

$$\tilde{A}_{i,j} = A_{i,j} + \tilde{a}_{i,j}^{C}\Phi_{i,j}^{\text{old}}, \tag{8.13}$$

where the symbol $\sim$ denotes the "modified" coefficients accounting for the linearization of Boltzmann relation and where the local Debye length $\lambda_{i,j}$ is given by

$$\lambda_{i,j} = \sqrt{\frac{e^2 n_{i,j}}{\varepsilon_{i,j} k_B T_e}}, \tag{8.14}$$

and where $n_{i,j}$ is the local electron density and $\Phi_{i,j}^{\text{old}}$ the potential calculated at the previous iteration.

A specific treatment is done to the various coefficients at the boundaries. For example, to fix the potential of an electrode, all the face coefficients are set to 0, the central coefficient to 1 and the rhs of the five-point equation to the electrode potential.

When the domain is defined, a relative permitivity is assigned to each cell of plasma or dielectric. As seen previously (equations 8.8 and 8.9), when solving Poisson's equation the permitivity has to be known on the faces of each control volume. They are estimated as follows

$$\varepsilon_{i+\frac{1}{2},j}^{x} = \frac{1}{2}\left(\varepsilon_{i,j}^{\text{cell}} + \varepsilon_{i,j-1}^{\text{cell}}\right), \tag{8.15}$$

and

$$\varepsilon_{i,j+\frac{1}{2}}^{r} = \frac{1}{2}\left(\varepsilon_{i,j}^{\text{cell}} + \varepsilon_{i-1,j}^{\text{cell}}\right). \tag{8.16}$$

Finally. rather than using the conventional successive over-relaxation technique (SOR), the Modified Strongly Implicit method developed by Shneider and Zedan (Shneider and Zedan 1981), and improved by Hagelaar (Hagelaar 2000), was used to solve the five-point equations coming from Poisson's equation (equation 8.8).

Bibliography

J. C. Adam, A. G. Serveniere, and A. B. Langdon. Electron sub-cycling in particle simulation of plasma. *Journal of Computational Physics*, 47:229–244, 1982. 47

R. D. Albert and P. J. Lindstrom. Auroral-Particle Precipitation and Trapping Caused by Electrostatic Double Layers in the Ionosphere. *Science*, 170:1398–1401, 1970. 16, 25, 43

H. Alfvén. On the theory of magnetic storms and aurorae. *Tellus*, 10(1):104–116, 1958. 16, 25, 43

H. Alfvén and P. Carlqvist. Currents in the Solar Atmosphere and a Theory of Solar Flares. *Solar Physics*, 1:220–+, 1967. 16, 25

Y. M. Aliev, I. D. Kaganovich, and H. Schlüter. Quasilinear theory of collisionless electron heating in radio frequency gas discharges. *Physics of Plasmas*, 4:2413–2421, July 1997. 32, 55

D. Andersson. Measurements of electron energy distributions in front of and behind a stationary plasma sheath. *Journal of Physics D Applied Physics*, 10:1549–1556, Aug. 1977. 23

J. G. Andrews and J. E. Allen. Theory of a Double Sheath between Two Plasmas. *Royal Society of London Proceedings Series A*, 320:459–472, 1971. 17, 20, 23, 43, 63

R. R. Arslanbekov and A. A. Kudryavtsev. Modeling of nonlocal electron kinetics in a low-pressure afterglow plasma. *Physical Review E*, 58:7785, 1998. 70

R. R. Arslanbekov, A. A. Kudryavtsev, and L. D. Tsendin. Electron-distribution-function cutoff mechanism in a low-pressure afterglow plasma. *Physical Review E*, 64(1):016401, 2001. 70

S. Ashida, C. Lee, and M. A. Lieberman. Spatially averaged (global) model of time modulated high density argon plasmas. *Journal of Vacuum Science Technology*, 13:2498, 1995. 70

S. Ashida, M. R. Shim, and M. A. Lieberman. Measurements of pulsed-power modulated argon plasmas in an inductively coupled plasma source. *Journal of Vacuum Science Technology*, 14:391, 1996. 70

K. D. Baker, N. Singh, L. P. Block, R. Kist, W. Kampa, and H. Thiemann. Studies of strong laboratory double layers and comparison with computer simulation. *Journal of Plasma Physics*, 26:1–27, 1981. 17

I. B. Bernstein, J. M. Greene, and M. D. Kruskal. Exact Nonlinear Plasma Oscillations. *Physical Review*, 108:546–550, Nov. 1957. 18, 24

I. B. Bernstein and T. Holstein. Electron Energy Distributions in Stationary Discharges. *Physical Review*, 94:1475, 1954. 71

M. A. Biondi. Diffusion cooling of electrons in ionized gases. *Physical Review*, 93(6):1136, 1954. 70

C. K. Birdsall. Particle-in-cell charged-particle simulations, plus monte carlo collisions with neutral atoms, pic-mcc. *IEEE Transactions on Plasma Science*, 19(2):65–85, 1991. 46

C. K. Birdsall and D. Fuss. Clouds-in-clouds, clouds-in-cells physics for many body plasma simulation. *Journal of Computational Physics*, 3(4):494, 1969. 47, 48, 85, 88, 100

C. K. Birdsall and A. B. Langdon. *Plasma Physics via Computer*. McGraw-Hill, Inc. New York, NY, USA, 1985. 28, 47, 48, 49, 50, 85, 88

L. P. Block. A double layer review. *Astrophysics and Space Science*, 55:59–83, 1978. 57, 60

J.-P. Boeuf. Numerical model of rf glow discharges. *Physical Review A*, 36: 2782–2792, 1987. 27, 108, 110

J.-P. Boeuf and L. C. Pitchford. Two-dimensional model of a capacitively coupled rf discharge and comparisons with experiments in the Gaseous Electronics Conference reference reactor. *Physical Review E*, 51:1376–1390, 1995. 27

D. Bohm. *Minimum ionic kinetic energy for a stable sheath*. New York : Mcgraw-hill, 1949. 27

J. E. Borovsky. *The simulation of plasma double layer structures in two dimensions*. PhD thesis, Iowa Univ., Oakdale, February 1981. 23

J. E. Borovsky and G. Joyce. Simulation of plasma double-layer structures. In *Presented at the Symp. on Plasma Double Layers, Roskilde, Denmark, 1 May 1982*, 1982. 23

R. W. Boswell. Plasma production using a standing helicon wave. *Physics Letters A*, 33:457–458, Dec. 1970. 108

R. W. Boswell, E. Marsch, and C. Charles. Current-free electric double layer in a coronal magnetic funnel. *Astrophysical Journal Letters*, 78, 2006. 16, 25, 46

K. J. Bowers. Accelerating a Particle-in-Cell Simulation Using a Hybrid Counting Sort. *Journal of Computational Physics*, 173:393–411, Nov. 2001. 86

N. S. J. Braithwaite and J. E. Allen. Boundaries and probes in electronegative plasmas . *Journal of Physics D Applied Physics*, 21:1733–1737, Dec. 1988. 107

O. Buneman. Dissipation of current in ionized media. *Physical Review*, 115(3): 503–517, 1959. 47

P. Burger. Elastic collsions in simulating one-dimensional plasma diodes on the computer. *Physics of Fluids*, 10:658, 1967. 47

K. L. Cartwright, J. P. Verboncoeur, and C. K. Birdsall. Nonlinear hybrid boltzmann particle-in-cell acceleration algorithm. *Physics of Plasmas*, 7(8): 3253–3256, 2000. 86, 92

P. Chabert and T. E. Sheridan. Kinetic model for a low-pressure discharge with negative ions . *Journal of Physics D Applied Physics*, 33:1854–1860, 2000. 86, 96, 108, 110, 122

C. Chan, M. H. Cho, N. Hershkowitz, and T. Intrator. Laboratory evidence for ion-acoustic-type double layers. *Physical Review Letters*, 52:1782–1785, May 1984. 17

C. Chan, M.-H. Cho, N. Hershkowitz, and T. Intrator. Experimental observation of slow ion acoustic double layers. *Physical Review Letters*, 57:3050–3053, Dec. 1986. 18

C. Chan and N. Hershkowitz. Transition from single to multiple double layers. *Physics of Fluids*, 25(12):2135–2137, 1982. 25

C. Chan and N. Hershkowitz. Electron temperature differences and double layers. *Physics of Fluids*, 26(6):1587–1595, 1983. 76

G. Chanteur, J. C. Adam, R. Pellat, and A. S. Volokhitin. Formation of ion-acoustic double layers. *Physics of Fluids*, 26:1584–1586, June 1983. 17

C. Charles. Hydrogen ion beam generated by a current-free double-layer in an helicon plasma. *Applied Physics Letters*, 84(3):332–334, 2004. 46, 79

C. Charles. High source potential upstream of a current-free electric double layer. *Physics of Plasmas*, 12(044508), 2005a. 46

C. Charles. Spatially resolved energy analyzer measurements of an ion beam on the low potential side of a current-free double-layer. *IEEE Transactions on Plasma Science*, 33(2):336, 2005b. 46

C. Charles. Large area generation of supersonic ion beams; application to surface functionalisation. In *Proceedings of the 6th international conference on reactive plasmas and 23rd symposium on plasma processing*, 2006. 46, 83

C. Charles and R. W. Boswell. Current-free double-layer formation in a high-density helicon discharge. *Applied Physics Letters*, 82(9):1356–1358, 2003. 16, 29, 44, 45, 46, 55, 56, 58, 63, 64, 66, 67, 77, 78, 108, 130

C. Charles and R. W. Boswell. Laboratory evidence of a supersonic ion beam generated by a current-free helicon double-layer. *Physics of Plasmas*, 11(4): 1706, 2004a. 46

C. Charles and R. W. Boswell. Time development of a current-free double-layer. *Physics of Plasmas*, 11(8), 2004b. 46, 58

C. Charles, R. W. Boswell, P. Alexander, C. Costa, O. Sutherland, J. Kingwell, A. Parfitt, L. Pfiztner, R. Franzen, and P. E. Frigot. Radial divergence of a xenon ion beam formed in a helicon double layer thruster. *Applied Physics Letters (to be submitted)*, 2006. 46, 83

F. F. Chen. *Introduction to plasma physics and controlled fusion*. Plenum Press, second edition, 1984. 20, 65

F. F. Chen. Physical mechanism of current-free double layers. *Physics of Plasmas*, 13:034502, 2006. 67

P. K. Chu, S. Qin, C. Chan, N. W. Cheung, and L. A. Larson. Plasma immersion ion implantation - a fledgling technique for semiconductor processing. *Materials Science & Engineering R-Reports*, R17:207–80, 1996. 87

P. Coakley, N. Hershkowitz, R. Hubbard, and G. Joyce. Experimental observations of strong double layers. *Physical Review Letters*, 40(4):230–233, 1978. 16, 17, 23, 24, 43

B. I. Cohen and R. P. Freis. Orbit-averaged implicit particle codes. *Journal of Computational Physics*, 45:345–366, 1982. 47, 86

R. H. Cohen and T. D. Rognlien. Electron kinetics in radio-frequency magnetic fields of inductive plasma sources . *Plasma Sources Science and Technology*, 5:442–452, Aug. 1996a. 32, 55

R. H. Cohen and T. D. Rognlien. Induced magnetic-field effects in inductively coupled plasmas. *Physics of Plasmas*, 3:1839–1847, May 1996b. 32, 55

S. A. Cohen, N. S. Siefert, S. Stange, E. E. Scime, and F. M. Levinton. Ion acceleration in plasmas emerging from a helicon-heated magnetic-mirror device. *Physics of Plasmas*, 10(6):2593, 2003. 46, 81

J. R. Conrad, J. L. Radtke, R. A. Dodd, F. J. Worzala, and N. C. Tran. Plasma source ion-implantation technique for surface modification of materials. *Journal of Applied Physics*, 62:4591–6, 1987. 87

D. J. Cooperberg, V. Vahedi, and C. K. Birdsall. Pic-mcc with variable particle weights. In P. Valley Forge, editor, *Proc. Int. Conf. on the NumericalSimulationof Plasmas*, 1994. 86

G. G. Coppa, G. Lapenta, G. Dellapianna, F. Donato, and V. Ricardo. Blob method for kinetic plasma simulation with variable-size particles. *Journal of Computational Physics*, 1996:268–284, 1996. 47, 86

J. Dawson. One-dimensional plasma model. *Physics of Fluids*, 5:445, 1962. 47

J. S. DeGroot, C. Barned, A. E. Walstead, and O. Buneman. Localized structures and anomalous dc resistivity. *Physical Review Letters*, 38(22), 1977. 22, 43

K. G. Emeleus and G. A. Woolsey. *Discharges in electronegative gases*. London: Taylor and Francis, 1970. 107

R. N. Franklin. Electronegative plasmas - why are they so different? *Plasma Sources Science and Technology*, 11:A31–A37, Aug. 2002. 107

R. N. Franklin and J. Snell. The free fall column with negative ions . *Journal of Physics D Applied Physics*, 25:453–457, Mar. 1992. 107

A. Fruchtman. Electric field in a double layer and the imparted momentum. *Physical Review Letters*, 96(065005), 2006. 67

L. Garrigues, A. Heron, J. C. Adam, and J. P. Boeuf. Hybrid and particle-in-cell models of a stationary plasma thruster. *Plasma Sources Science and Technology*, 9:219–226, May 2000. 86, 96

F. N. Gesto. Ion detachment in the helicon double-layer thruster exhaust beam. Master's thesis, The Australian National University, 2005. 46, 83

F. N. Gesto, B. D. Blackwell, C. Charles, and R. W. Boswell. Ion detachment in the helicon double-layer thruster exhaust beam. *Journal of Propulsion and Power*, 22(1), 2006. 46, 83

T. S. Gill, P. Bala, H. Kaur, N. S. Saini, S. Bansal, and J. Kaur. Ion-acoustic solitons and double-layers in a plasma consisting of positive and negative ions with non-thermal electrons. *The European Physical Journal D - Atomic, Molecular and Optical Physics*, 31(1):91, 2004. 18

V. A. Godyak and V. I. Kolobov. Effect of Collisionless Heating on Electron Energy Distribution in an Inductively Coupled Plasma. *Physical Review Letters*, 81:369–372, 1998. 70

V. A. Godyak, V. P. Meytlis, and H. R. Strauss. Tonks-langmiur problem for a bi-maxwellian plasma. *IEEE Transactions on Plasma Science*, 23(4):728, 1995. 70

V. A. Godyak and R. B. Piejak. Abnormally low electron energy and heating-mode transition in a low-pressure argon rf discharge at 13.56 MHz. *Physical Review Letters*, 65:996–999, 1990. 69

V. A. Godyak and R. B. Piejak. Paradoxical spatial distribution of the electron temperature in a low pressure rf discharge. *Applied Physics Letters*, 63:3137–3139, 1993. 70

V. A. Godyak, R. B. Piejak, and B. M. Alexandrovich. Electrical characteristics of parallel-plate rf discharges in argon. *IEEE Transactions on Plasma Science*, 19(4):660, 1991. 27

V. A. Godyak, R. B. Piejak, and B. M. Alexandrovich. Evolution of the electron-energy-distribution function during rf discharge transition to the high-voltage mode. *Physical Review Letters*, 68:40–43, 1992. 69

V. A. Godyak, R. B. Piejak, and B. M. Alexandrovich. Probe diagnostics of non-Maxwellian plasmas. *Journal of Applied Physics*, 73:3657–3663, 1993. 32

V. A. Godyak, R. B. Piejak, and B. M. Alexandrovich. Electron energy distribution function measurements and plasma parameters in inductively coupled argon plasma. *Plasma Sources Science and Technology*, 11:525, 2002. 70, 75, 83

C. K. Goertz and G. Joyce. Numerical simulation of the plasma double-layer. *Astrophysics and space science*, 32:165–173, 1975. 22, 43

K. S. Goswami, M. K. Kalita, and S. Bujarbarua. Theory of small amplitude electron acoustic double layers . *Plasma Physics and Controlled Fusion*, 28: 289–297, Jan. 1986. 18

L. Granovski. *Electric Current in Gas (Steady Current)*. Nauka, 1971. 70, 83

D. B. Graves and K. F. Jensen. A continuum model of dc and rf discharges. *IEEE Transactions on Plasma Science*, PS-14(2):78, 1986. 27

G. J. M. Hagelaar. *Modeling of microdischarges for display technology*. PhD thesis, Technische Universiteit Eindhoven, 2000. 137

G. J. M. Hagelaar. Some thoughts on the helicon double layer. Technical report, Space Plasma, Power and Propulsion, The Australian National University, 2005a. 67

G. J. M. Hagelaar. Stochastic electron heating in ac electric fields with transverse intensity variations. Technical report, CPAT, Université Paul Sabatier, Toulouse, France, 2005b. 39

G. J. M. Hagelaar. How to normalize the density of boltzmann electrons in a transient self-consistent plasma model. Technical report, CPAT, Université Paul Sabatier, Toulouse, France, 2006. 92

G. J. M. Hagelaar and L. C. Pitchford. Solving the boltzmann equation to obtain electron transport coefficients and rate coefficients for fluid models. *Plasma Sources Science and Technology*, 14:722, 2005. 28

H. D. Hagstrum. Auger ejection of electrons from molibdenum by noble gas ions. *Physical Review*, 104(3):672–683, 1956. 47

G. Hairapetian and R. L. Stenzel. Observation of a stationary, current-free double layer in plasma. *Physical Review Letters*, 65(2):175, 1990. 44

G. A. Harrower. Energy spectra of secondary electrons from mo and w for low primary energy. *Physical Review*, 104(1):52–56, 1956. 47

S. S. Hasan and D. Ter Haar. The Alfven-Carlquist double-layer theory of solar flares. *Solar Physics*, 56:89–107, 1978. 43

R. Hatakeyama, Y. Suzuki, and N. Sato. Formation of electrostatic potential barrier between different plasmas. *Physical Review Letters*, 50:1203–1206, 1983. 44

N. Hershkowitz. Review of recent laboratory double layer experiments. *Space Science Reviews*, 41:351–391, Aug. 1985. 23, 43

N. Hershkowitz, J. R. Dekock, P. Coakley, and S. L. Cartier. Surface trapping of primary electrons by multidipole magnetic fields. *Review of Scientific Instruments*, 51:64–69, Jan. 1980. 24

N. Hershkowitz, G. L. Payne, C. Chan, and J. R. Dekock. Weak double layers. *Plasma Physics*, 23:903–925, Oct. 1981. 17, 24

R. W. Hockney and J. W. Eastwood. *Computer Simulation Using Particles*. IOP, Bristol, 1988. 28, 47, 48, 49, 50, 85, 88

C. Hollenstein, M. Guyot, and E. S. Weibel. Stationary potential jumps in a plasma. *Physical Review Letters*, 45:2110–2113, 1980. 17

R. F. Hubbard and G. Joyce. Simulation of auroral double layers. *Journal of Geophysical Research*, 84:4297–4304, Aug. 1979. 17

C. Jacobsen and P. Carlqvist. Solar Flares Caused by Circuit Interruptions. *Icarus*, 3:270–+, Sept. 1964. 25

G. Joyce and R. F. Hubbard. Numerical simulation of plasma double-layers. *Journal of plasma physics*, 20:391–404, 1978. 22, 43

E. Kawamura, C. K. Birdsall, and V. Vahedi. Physical and numerical methods of speeding up particle codes and paralleling as applied to RF discharges. *Plasma Sources Science and Technology*, 9:413–428, Aug. 2000. 47, 85

A. M. Keesee, E. E. Scime, C. Charles, A. Meige, and R. W. Boswell. The ion velocity distribution function in a current-free double layer. *Physics of Plasmas*, 12:093502, 2005. 79, 81

G. Knorr and C. K. Goertz. Existence and stability of strong potential double layers. *Journal of Astrophysics and Space Science*, 31:209–223, 1974. 20, 23, 43

V. I. Kolobov and V. A. Godyak. Nonlocal electron kinetics in collisional gas discharge plasma. *IEEE Transactions on Plasma Science*, 23(4):503, 1995. 71

V. I. Kolobov, D. P. Lymberopoulos, and D. J. Economou. Electron kinetics and non-Joule heating in near-collisionless inductively coupled plasmas. *Physical Review E*, 55:3408, 1997. 70

A. Kono. Complex sheath formation around a spherical electrode in electronegative plasmas: a comparison between a fluid model and a particle simulation . *Journal of Physics D Applied Physics*, 34:1083–1090, Apr. 2001. 108

U. Kortshagen, A. Maresca, K. Korlov, and B. Heil. Recent progress in the understanding of electron kinetics in low-pressure inductive plasma. *Applied Surface Science*, 192:244, 2002. 70

I. G. Kouznetsov, A. J. Lichtenberg, and M. A. Lieberman. Internal sheaths in electronegative discharges. *Journal of Applied Physics*, 86:4142–4153, 1999. 108, 110

M. J. Kushner. Monte-Carlo simulation of electron properties in rf parallel plate capacitively coupled discharges. *Journal of Applied Physics*, 54:4958–4965, Sept. 1983. 28

D. T. K. Kwok, Z. M. Zeng, P. K. Chu, and T. E. Sheridan. Hybrid simulation of sheath and ion dynamics of plasma implantation into ring-shaped targets . *Journal of Physics D Applied Physics*, 34:1091–1099, 2001. 86, 88, 96

L. D. Landau. On the vibrations of the electronic plasma. *J. Phys. (USSR)*, 10 (25), 1946. 32

A. B. Langdon. Analysis of the time integration in plasma simulation. *Journal of Computational Physics*, 30:202–221, Feb. 1979. 47

A. B. Langdon and C. K. Birdsall. Theory of plasma simulation using finite-size particles. *Physics of Fluids*, 13(8):2115, 1970. 47, 48, 85, 88

A. B. Langdon, B. I. Cohen, and A. Friedman. Direct implicit large time step particle simulation of plasma. *Journal of Computational Physics*, 51:107–138, 1983. 47, 86

I. Langmuir. The Interaction of Electron and Positive Ion Space Charges in Cathode Sheaths. *Physical Review*, 33:954–989, 1929. 16, 17, 18, 20, 23, 43

B. Legradic. Electron heating in low-pressure inductive discharges. Master's thesis, Space Plasma, Power and Propulsion - The Australian National University, 2006. 75

M. A. Lieberman. Analytical model of a current-free double layer. private communication, 2006a. 60

M. A. Lieberman. Two distinct electron temperatures in the current-free double layer. private communication, 2006b. 67, 77

M. A. Lieberman and C. Charles. A theory for formation of a low pressure, current-free double layer. *Physical Review Letters (submitted)*, 2006. 20, 43, 63, 64, 76, 83

M. A. Lieberman and A. J. Lichtenberg. *Principles of Plasma Discharges and Materials Processing*. Wiley Interscience, New-York, second edition, 2005. 32, 52, 57, 105

P. C. Liewer and V. K. Decyk. A general concurrent algorithm for plasma particle-in-cell simulation codes. *Journal of Computational Physics*, 85(2): 302–322, 1989. 86

J. S. Logan, J. H. Keller, and R. G. Simmons. The rf glow-discharge sputtering model. *Journal of Vacuum Science and Technology*, 14(1):92, 1977. 26

P. J. Mardahl and J. P. Verboncoeur. Charge conservation in electromagnetic PIC codes; spectral comparison of Boris/DADI and Langdon-Marder methods. *Computer Physics Communications*, 106:219–229, Nov. 1997. 49

A. Maresca, K. Orlov, and U. Kortshagen. Experimental study of diffusive cooling of electrons in a pulsed inductively coupled plasma. *Physical Review E*, 65(5):056405, 2002. 70

A. Meige and R. W. Boswell. Electron energy distribution functions in low-pressure inductively-coupled bounded plasmas. *Physics of Plasmas (to appear)*, 2006. 69

A. Meige, R. W. Boswell, C. Charles, and M. M. Turner. One-dimensional particle-in-cell simulation of a current-free double-layer in an expanding plasma. *Physics of Plasmas*, 12(5), 2005a. 52, 55, 79, 101

A. Meige, M. Jarnyk, D. T. K. Kwok, and R. W. Boswell. Particle-in-cell simulation of an electron shock wave in a rapid rise time plasma immersion ion implantation process. *Physics of Plasmas*, 12:043503, April 2005b. 87

M. Meyyappan and J. P. Kreskovsky. Glow discharge simulation through solutions to the moments of the Boltzmann transport equation. *Journal of Applied Physics*, 68:1506–1512, Aug. 1990. 27

M. K. Mishra, A. K. Arora, and R. S. Chhabra. Ion-acoustic compressive and rarefactive double layers in a warm multicomponent plasma with negative ions. *Physical Review E*, 66(4):046402, Oct. 2002. 18

F. S. Mozer, C. W. Carlson, M. K. Hudson, R. B. Torbert, B. Parady, J. Yatteau, and M. C. Kelley. Observations of paired electrostatic shocks in the polar magnetosphere. *Physical Review Letters*, 38:292–295, Feb. 1977. 25, 43

K. Nanbu and V. V. Serikov. Particle-in-cell simulation of expansions of dense plasma sources for x-ray laser system. *Japanese Journal of Applied Physics*, 36(7A):4497–4508, 1997. 23

D. L. Newman, M. V. Goldman, R. E. Ergun, and A. Mangeney. Formation of double layers and electron holes in a current-driven space plasma. *Physical Review Letters*, 87(25):255001–1, 2001. 23, 43

J. L. Pack, R. E. Voshall, A. V. Phelps, and L. E. Kline. Longitudinal electron diffusion coefficients in gases: Noble gases. *Journal of Applied Physics*, 71: 5363–5371, June 1992. 51

J. H. Parker. Position- and Time-Dependent Diffusion Modes for Electrons in Gases. *Physical Review*, 139:1792, 1965. 70

J. D. P. Passchier and W. J. Goedheer. A two-dimensional fluid model for an argon rf discharge. *Journal of Applied Physics*, 74:3744–3751, 1993. 27

S. V. Patankar. *Numerical heat transfer and fluid flow.* Washington, DC, Hemisphere Publishing Corp., 1980. 210 p., 1980. 135

H. L. Pecseli and J. Trulsen. Nonlinear evolution of the ion-ion beam instability. *Physical Review Letters*, 48:1355–1358, May 1982. 25

F. W. Perkins and Y. C. Sun. Double layers without current. *Physical Review Letters*, 46(2):115, 1981. 18, 44

A. V. Phelps. The application of scattering cross sections to ion flux models in discharge sheaths. *Journal of Applied Physics*, 1994(2):747–753, 1994. 51

A. B. Pippard. The high frequency skin resistance of metals at low temperatures. *Physica*, 15(45), 1949. 32

L. C. Pitchford, J. P. Boeuf, and W. L. Morgan. The siglo data base, cpat and kinema software - bolsig. URL `http://www.cpat.ups-tlse.fr/operations/operation_03/POSTERS/BOLSIG/`. 117

N. Plihon. Direct measurement of the electronegativity and photodetachment. private communication, LPTP - Ecole Polytechnique, 2005. 110

N. Plihon. *Stabilite et structure electrique d'une decharge inductive basse pression en gaz electronegatif.* PhD thesis, Laboratoire de Physique et Technologie des Plasmas CNRS-Ecole Polytechnique, 2006. 110, 127

N. Plihon, C. S. Corr, and P. Chabert. Double layer formation in the expanding region of an inductively coupled electronegative plasma. *Applied Physics Letters*, 86(091501), 2005a. 108, 109, 110, 113, 119

N. Plihon, C. S. Corr, P. Chabert, and J.-L. Raimbault. Periodic formation and propagation of double layers in the expanding chamber of an inductive discharge operating in ar/sf6 mixtures. *Journal of Applied Physics*, 98(023306), 2005b. 29, 108, 109, 110, 123, 124, 127, 128, 131

R. K. Porteous and D. B. Graves. Modeling and simulation of magnetically confined low-pressure plasmas in two dimensions. *IEEE Transactions on Plasma Science*, 19(2):204, 1991. 28

R. K. Porteous, H.-M. Wu, and D. B. Graves. A two-dimensional, axisymmetric model of a magnetized glow discharge plasma . *Plasma Sources Science Technology*, 3:25–39, February 1994. 28

W. H. Press, S. A. Teukolsky, W. T. Vetterling, and B. P. Flannery. *Numerical Recipes in C : The Art of Scientific Computing*. Cambridge University Press, 1992. 50, 89

B. H. Quon and A. Y. Wong. Formation of potential double layers in plasmas. *Physical Review Letters*, 37(21):1393–1397, 1976. 17, 23, 24, 43

M. A. Raadu. the physics of double layers and their role in astrophysics. *Physics Reports*, 178:25–97, 1989. 15, 25, 43

M. A. Raadu and J. J. Rasmussen. Dynamical aspects of electrostatic double layers. *Astrophysics and Space Science*, 144:43–71, 1988. 19

T. Rhymes and R. W. Crompton. Experimental observations of the diffusion cooling of electrons in argon. *Australian Journal of Physics*, 28:675, 1975. 70

R. E. Robson. Diffusion cooling in a magnetic field. *Physical Review E*, 61:848, 2000. 70

R. Roychoudhury and S. Bhattacharyya. Ion-acoustic double layers. *Journal of Plasma Physics*, 42:353–360, Dec. 1989. 18

R. Z. Sagdeev. Cooperative Phenomena and Shock Waves in Collisionless Plasmas. *Reviews of Plasma Physics*, 4:23–+, 1966. 20, 21

K. Sato and F. Miyawaki. Formation of presheath and current-free double layer in a two-electron-temperature plasma. *Physics of Fluids B: Plasma Physics*, 4(5):1247, Feb. 1992. 44

N. Sato, R. Htakeyama, S. Iizuka, and K. Saeki. Ultrastrong stationaty double layers in a nondischarge magetoplasma. *Physical Review Letters*, 46(20): 1330–1333, 1981. 17, 23, 24

N. Sato, G. Popa, E. Märk, E. Mravlag, and R. Schrittwieser. Instability as a source for traveling ion waves. *Physics of Fluids*, 19:70–73, Jan. 1976. 16

T. Sato and H. Okuda. Ion-acoustic double layers. *Physical Review Letters*, 44 (11):740–743, 1980. 17, 23, 43

A. N. Sekar and Y. C. Saxena. Potential double layers in double plasma device. *Pramana*, 23(3):351, 1984. 25

A. N. Sekar and Y. C. Saxena. Development of ion-acoustic double layers through ion-acoustic fluctuations. *Plasma Physics and Controlled Fusion*, 27:181–191, Feb. 1985. 18

T. E. Sheridan. Double layers in a modestly collisional electronegative discharge. *Journal of Physics D Applied Physics*, 32:1761–1767, Aug. 1999. 108, 110

T. E. Sheridan, N. S. J. Braithwaite, and R. W. Boswell. Relation between double layers and flux for a collisionless discharge with two negative components. *Physics of Plasmas*, 6:4375–4381, 1999a. 108, 110

T. E. Sheridan, P. Chabert, and R. W. Boswell. Positive ion flux from a low-pressure electronegative discharge . *Plasma Sources Science and Technology*, 8:457–462, 1999b. 108, 110, 122

G. E. Shneider and M. Zedan. A modified strongly implicit procedure for the numerical solution of field problems. *Numerical Heat Transfer*, 4:1–19, 1981. 89, 137

C. H. Shon, H. J. Lee, and J. K. Lee. Method to increase the simulation speed of particle-in-cell (pic) code. *Computer Physics Communications*, 141:322–329, 2001. 47, 86

N. Singh. Double layer formation. *Plasma Physics*, 24:639–660, June 1982. 23

N. Singh and R. W. Schunk. Plasma response to the injection of an electron beam. *Plasma Physics and Controlled Fusion*, 26:859–890, July 1984. 23

H. R. Skullerud. The stochastic computer simulation of ion motion in a gas subjected to a constant electric field. *Journal of Physics D*, 1(11):1567–1568, 1968. 100

T. J. Sommerer, W. N. G. Hitchon, and J. E. Lawler. Electron heating mechanisms in helium rf glow discharges: A self-consistent kinetic calculation. *Physical Review Letters*, 63:2361–2364, Nov. 1989. 28

T. J. Sommerer and M. J. Kushner. Numerical investigation of the kinetics and chemistry of rf glow discharge plasmas sustained in He, N_2, O_2, $He/N_2/O_2$, $He/CF_2/O_2$, and SiH_4/NH_3 using a Monte Carlo-fluid hybrid model. *Journal of Applied Physics*, 71:1654–1673, Feb. 1992. 28

P. C. Stangeby and J. E. Allen. Current limitation in mercury vapour discharges II. Experiment . *Journal of Physics D Applied Physics*, 6:224–242, Jan. 1973. 16

X. Sun, C. Biloiu, R. Hardin, and E. E. Scime. Parallel velocity and temperature of argon ions in an expanding, helicon source driven plasma. *Plasma Sources Science and Technology*, 13:359, 2004. 46

X. Sun, A. M. Keesee, C. Biloiu, E. E. Scime, A. Meige, C. Charles, and R. W. Boswell. Observations of ion-beam formation in a current-free double-layer. *Physical Review Letters*, 95(025004), 2005. 79, 81, 82

M. Surendra, D. B. Graves, and G. M. Jellum. Self-consistent model of direct-current glow discharge: treatment of the fast electrons. *Physical Review A*, 41(2):1112, 1990. 47

M. Surendra, D. B. Graves, and I. J. Morey. Electron heating in low-pressure rf glow discharges. *Applied Physics Letters*, 56:1022–1024, 1990. 47

O. Sutherland, C. Charles, N. Plihon, and R. W. Boswell. Experimental evidence of a double layer in a large volume helicon reactor. *Physical Review Letters*, 95(205002), 2005. 46

K. Tachibana. Excitation of the 1s5,1s4, 1s3, and 1s2 levels of argon by low-energy electrons. *Physical Review A*, 1986. 51

M. Temerin, K. Cerny, W. Lotko, and F. S. Mozer. Observation of double layers and solitary waves in the auroral plasma. *Physical Review Letters*, 48(17): 1175–1178, 1982. 16, 17, 25, 43

L. Tonks and I. Langmuir. A General Theory of the Plasma of an Arc. *Physical Review*, 34:876–922, Sept. 1929. 27

S. Torven. Modified Korteweg-de Vries equation for propagating double layers in plasmas. *Physical Review Letters*, 47:1053–1056, 1981. 43

S. Torvén and M. Babić. Current chopping space charge layers in a low pressure arc plasma. In J. G. A. Hölscher and D. C. Schram, editors, *Phenomena in Ionized Gases, Twelfth International Conference*, pages 124–+, Aug. 1975. 23

L. D. Tsendin. *Sov. Pkys.-JETP*, 39:805, 1974. 71

M. M. Turner. Collisionless electron heating in an inductively coupled discharge. *Physical Review Letters*, 71(12), 1993. 32, 52

M. M. Turner. Kinetic properties of particle-in-cell simulations compromised by monte carlo collisions. *Physics of Plasmas*, 13:033506, 2006. 51

M. M. Turner, R. A. Doyle, and M. B. Hopkins. Measured and simulated electron energy distribution functions in a low-pressure radio frequency discharge in argon. *Applied Physics Letters*, 62:3247–3249, 1993. 69

M. Tuszewski and S. Gary. Downstream instabilities of electronegative plasma discharges. *Physics of Plasmas*, 10(2):539, 2003. 110, 128

M. Tuszewski and R. R. White. Instabilities of ar/sf6 inductive plasma discharges. *Journal of Applied Physics*, 94(5):2858, 2003. 110, 128

M. Tuszewski, R. R. White, and G. A. Wurden. Relaxation oscillations of low-frequency ar/sf6 inductive plasma discharges. *Plasma Sources Science and Technology*, 12:396, 2003. 110, 128

V. Vahedi, C. K. Birdsall, M. A. Lieberman, G. DiPeso, and T. D. Rognlien. Capacitive rf discharges modeled by particle-in-cell monte-carlo simulation. ii: comparisons with laboratory measurments of electron energy distribution functions. *Plasma Sources Science and Technology*, 2:273–278, 1993a. 47

V. Vahedi, G. DiPeso, C. K. Birdsall, M. A. Lieberman, and T. D. Rognlien. Capacitive rf discharges modeled by particle-in-cell monte-carlo simulation. i: analysis of numerical techniques. *Plasma Sources Science and Technology*, 2:261–272, 1993b. 47

V. Vahedi and M. Surendra. A monte carlo collision model for the particle-in-cell method: application to argon and oxygen discharges. *Computer Physics Communications*, 87:179–198, 1995. 28, 47, 51, 89, 100

D. Vender. *Numerical Studies of the Low Pressure Plasma*. PhD thesis, Research School of Physical Science and Engineering - Australian National University, September 1990. 52

D. Vender and R. W. Boswell. Numerical modeling of low-pressure plasmas. *IEEE Transactions on Plasma Science*, 18(4):725, 1990. 52

D. Vender, H. B. Smith, and R. W. Boswell. Simulations of multipactor-assisted breakdown in radio frequency plasmas. *Journal of Applied Physics*, 80:4292–4298, 1996. 48

P. L. G. Ventzek, T. J. Sommerer, R. J. Hoekstra, and M. J. Kushner. Two-dimensional hybrid model of inductively coupled plasma sources for etching. *Applied Physics Letters*, 63:605–607, 1993. 86, 96

J. P. Verboncoeur. Particle simulation of plasmas: review and advances. *Plasma Physics and Controlled Fusion*, 47:A231, 2005. 46

J. P. Verboncoeur, M. V. Alves, V. Vahedi, and C. K. Birdsall. Simultaneous potential and circuit solution for 1d bounded plama particle simulation code. *Journal of Computational Physics*, 104:321–328, 1993. 47, 50

F. Verheest. Are weak dust-acoustic double layers adequately described by modified Korteweg-de Vries equations? *Physica Scripta*, 47:274–+, Feb. 1993. 22

F. Verheest and M. A. Hellberg. Bohm sheath criteria and double layers in multispecies plasmas. *Journal of Plasma Physics*, 57:465, 1997. 78

E. S. Weibel. Anomalous skin effect in a plasma. *Physics of Fluids*, 10:741, 1967. 32

B. P. Wood. *Sheath Heating in Low-Pressure Capacitive Radio Frequency Discharges*. PhD thesis, University of California, Berkeley, 1991. 26